

# SHAPE MEMORY CERAMICS IN SMALL VOLUMES

BY

ALAN LAI

B.S. Metals and Materials Engineering  
McGill University, Montreal, 2007

M.S. Applied Earth Sciences  
Delft University of Technology, Delft, 2010

SUBMITTED TO THE DEPARTMENT OF MATERIALS SCIENCE & ENGINEERING  
IN PARTIAL FULFILLMENT OF THE REQUIREMENTS FOR THE DEGREE OF  
DOCTOR OF PHILOSOPHY IN MATERIALS SCIENCE AND ENGINEERING  
AT THE  
MASSACHUSETTS INSTITUTE OF TECHNOLOGY

JUNE 2016

© 2016 Massachusetts Institute of Technology. All rights reserved

Signature of Author: \_\_\_\_\_

Alan Lai

Department of Materials Science and Engineering

April 14, 2016

Certified by: \_\_\_\_\_

Christopher A. Schuh

Department Head and Danae and Vasilis Salapatas Professor of Metallurgy

Thesis Supervisor

Accepted by: \_\_\_\_\_

Donald R. Sadoway

John F. Elliott Professor of Materials Chemistry

Chair, Departmental Committee on Graduate Students



## ABSTRACT

---

Shape memory ceramics rely on martensitic transformations which are similar to those found in metallic shape memory materials, but ceramics offer several advantages over metals such as higher operating temperatures and larger transformation stresses. However, polycrystalline shape memory ceramics have shown poor cycling performance which limits their use in practical applications. This is due to the inherent physical constraints of the grains that create stress concentrations and eventually leads to intergranular fracture.

Here it is proposed that single crystalline and oligocrystalline ceramics — made with a single grain or very few grains — will avoid the physical constraints found in polycrystalline materials that lead to intergranular fracture and result in shape memory ceramics with enhanced cycling performance. Zirconia was chosen for study because it has the necessary martensitic transformations and has shown limited shape memory properties when in the bulk polycrystalline form. Focused ion beam milling was used to make single crystal and oligocrystal pillars of varying diameter that were compression tested using a nanomechanical testing platform to determine the mechanical properties.

This work showed that removing grain constraints in micron-scale shape memory zirconia prevented cracking and fracture. It also enhanced the number of achievable repeatable cycles from five in bulk materials to at least hundreds in small structures. The transition from single- to oligo- to poly-crystal was explored and it was found that fracture is more likely in polycrystals and that the transformation stresses increase as pillar diameter is increased, the opposite of what is observed in shape memory metals. This phenomenon is attributed to the higher stiffness of ceramics making the stored elastic energy more important. The effect of crystal orientation was investigated to aid in design and optimization. Orientation maps were produced for fracture behavior, elastic modulus, transformation stress, and transformation strain.

Finally four different scale-up architectures were proposed and implemented — powders, wires, foams, and thin films — and each demonstrated shape memory properties thereby paving the way for deployment in practical applications.





## ACKNOWLEDGMENTS

---

I would like to thank all the people who have helped me throughout my Ph.D. work whether they aided me technically, professionally, administratively, or personally. This work would not have been possible without all of their help and I am truly grateful to everyone.

Firstly, I would like to thank my advisor Prof. Chris Schuh for his guidance and direction — I owe so much of my development as a researcher to you. I always left our meetings together feeling more optimistic even when the research was difficult and not going as planned. Thank you for pushing me to my limits, you constantly showed great trust and faith in me and I am embiggened because of it.

I would also like to thank my thesis committee members, Prof. Sam Allen and Prof. Silvija Gradečak for all their input and valuable advice over the years which has greatly helped to shape this work.

This work would not be possible without all the people working directly on the various projects such as, Xueying Zhao and Dr. Hang Yu at MIT, and Xiaomei Zeng, Dr. Zehui Du, Pengcheng Ye, Prof. Chee Lip Gan, and Prof. Ma Jan at Nanyang Technological University in Singapore. It was my pleasure working with all of you and I hope our collaborations will continue into the future.

Many thanks to the numerous other people at MIT that helped me along the way including, M. Tarkanian, C. DiPerna, I. Feltier, D. Bono, S. Chen, P. Boisvert, Y. Zhang, S. Speakman, C. Settens, A. Schwartzman, K. Broderick, T. McClure, E. Haverty, A. Mireles, J. Hollingsworth-Brown, and D. Johansen. I have learned so much from each of you and cannot thank you enough for all the time you spent helping me.

All of the past and present Schuh group members had a large impact on me during my time at MIT. I learned a great deal from everyone, from how to navigate the academic world, how to be a more rigorous scientist, and how to be a better presenter. In particular I would like to thank Mike Gibson, Zach Cordero, Sam Humphry-Baker, Nihan Tuncer, Stian Ueland, Oliver Johnson, Matteo Seita, Arvind Kalidindi, and Xueying Zhao for their insightful discussions and for their endless patience in answering all my questions.

Making it through grad school would not have been possible if I did not have the proper support outside of the lab and I have many friends to thank for getting me through it all. Thanks for all the good times Colin McNair, Jacobs Ruben, Adam Freedman, Matt Humbert, Alex Broad, Ian Fein, and Scott Burger. I know the good times will continue long into the future, I'd even bet on it.

Thank you to all the members of the MIT club ice hockey team, you provided me with an outlet to vent all the frustrations of lab work. I will never forget the memorable friendships, occasional goals, and unfortunate injuries.

Thank you to the people and organizations that funded this work, notably the Temasek Laboratories at Nanyang Technological University and the Deshpande Center at MIT. Special thanks to Maren Cattonar and Leon Sandler at Deshpande for their guidance and patience.

Finally, I would like to thank my family for their support throughout the many years I have spent in school. You've always encouraged me to choose my own path and your encouragement along the way has always been appreciated, although not always vocalized. I am grateful to have such a wonderful and loving family and I couldn't have done any of this without you.

# CONTENTS

---

1	INTRODUCTION	15
1.1	Martensitic Phase Transformations . . . . .	15
1.2	The Shape Memory Effect . . . . .	16
1.3	Superelasticity - Stress Induced Transformations . . . . .	18
1.4	History and Applications of Shape Memory Materials . . . . .	19
1.5	Oligocrystalline Structures to Eliminate Brittle Fracture . . . . .	21
1.6	Sample Size Effects . . . . .	23
1.7	Research Objectives and Outline of Thesis . . . . .	24
2	SHAPE MEMORY CERAMICS IN SMALL VOLUMES	27
2.1	Shape Memory Ceramic Materials . . . . .	27
2.2	Zirconia as a Shape Memory Ceramic . . . . .	28
2.2.1	The Martensitic Transformation in Zirconia . . . . .	29
2.2.2	Transformation Toughening of Zirconia . . . . .	30
2.2.3	Doping Elements . . . . .	30
2.2.4	Shape Memory Properties of Polycrystalline Zirconia . . . . .	31
2.3	Shape Memory Ceramics in Small Volumes . . . . .	34
2.4	Fabrication and Characterization of Polycrystalline Zirconia . . . . .	34
2.5	Fabrication of Single Crystal Micro-Pillars . . . . .	39
2.6	Mechanical Testing of Single Crystal Micro-Pillars . . . . .	39
2.7	Superelastic Behavior of Single Crystal Micro-Pillars . . . . .	40
2.8	Energy Dissipation of Small-Scale Zirconia . . . . .	42
2.9	The Shape Memory Effect in Small-Scale Zirconia . . . . .	43
2.10	Comparison of Ceramic and Metallic Shape Memory Materials . . . . .	45
2.11	Conclusions . . . . .	48
3	OLIGOCRYSTALLINE TO POLYCRYSTALLINE TRANSITION	51
3.1	Size Effects in Shape Memory Metals . . . . .	51
3.2	Oligocrystalline Transition in Shape Memory Ceramics . . . . .	52
3.3	Transformation Stress Across the Oligocrystalline Transition . . . . .	55
3.4	Size Effect on Transformation Strain . . . . .	57
3.5	Conclusions . . . . .	57

4	ORIENTATION EFFECTS	59
4.1	Crystal Orientation Dependence in Shape Memory Metals . . . . .	59
4.2	Experimental Design for Orientation Dependence . . . . .	60
4.3	Orientation Effect on Elastic Loading Modulus . . . . .	70
4.4	Transformation Correspondences and Thermodynamics . . . . .	71
4.5	Orientation Effect on Transformation Stress . . . . .	74
4.6	Orientation Dependent Size Effects . . . . .	82
4.7	Orientation Effect on Transformation Strain . . . . .	84
4.8	Conclusions . . . . .	87
5	SCALE UP METHODS	89
5.1	Particles and Powder . . . . .	89
5.1.1	Superelastic Properties of Micron-Sized Particles . . . . .	90
5.1.2	Shape Memory Ceramic Powders . . . . .	92
5.1.3	Concluding Thoughts on Particles and Powders . . . . .	96
5.2	Oligocrystalline Wires . . . . .	97
5.2.1	Electrospinning of Shape Memory Ceramic Wires . . . . .	98
5.2.2	Concluding Thoughts on Oligocrystalline Wires . . . . .	101
5.3	Foams . . . . .	101
5.3.1	Fabrication of Ceramic Foams . . . . .	102
5.3.2	Freeze Casting . . . . .	103
5.3.3	Experimental Setup . . . . .	104
5.3.4	Freeze Cast Zirconia Structures . . . . .	105
5.3.5	Thermal Properties of Shape Memory Ceramic Foams . . . . .	106
5.3.6	Concluding Thoughts on Foams . . . . .	107
5.4	Thin Films . . . . .	108
5.4.1	Production of Zirconia Thin Films . . . . .	109
5.4.2	Characterization of Zirconia Thin Films . . . . .	111
5.4.3	Concluding Thoughts on Thin Films . . . . .	114
5.5	Conclusions . . . . .	115
6	CONCLUSIONS AND FUTURE WORK DIRECTIONS	117
A	APPENDIX A	125
A.1	Ceramic Powder Processing . . . . .	125
A.2	Focused Ion Beam Milling of Micro-Pillars . . . . .	126
A.3	Nanoindentation Micro-Compression . . . . .	127

A.4 Superelastic Micro-Compression Stress-Strain Curves . . . . . 128

BIBLIOGRAPHY . . . . . 133

## LIST OF FIGURES

---

Figure 1	Temperature Hysteresis of Martensitic Transformations . . . . .	16
Figure 2	Schematic of the Shape Memory Effect . . . . .	17
Figure 3	Superelastic Hysteresis . . . . .	19
Figure 4	Stress-Temperature Diagram . . . . .	20
Figure 5	Oligocrystalline Structures for Improved Superelastic Response .	23
Figure 6	Size Effects on Damping Capacity of Shape Memory Metals . . .	24
Figure 7	Crystal Structures of Pure ZrO <sub>2</sub> . . . . .	29
Figure 8	ZrO <sub>2</sub> Phase Diagrams . . . . .	31
Figure 9	Shape Memory Effect in CeO <sub>2</sub> -ZrO <sub>2</sub> . . . . .	32
Figure 10	Superelastic Behavior in CeO <sub>2</sub> -ZrO <sub>2</sub> . . . . .	33
Figure 11	Superelastic Cycling of CeO <sub>2</sub> -ZrO <sub>2</sub> . . . . .	33
Figure 12	Polycrystalline Grains of CeO <sub>2</sub> -ZrO <sub>2</sub> . . . . .	35
Figure 13	XRD Patterns for Varying Amounts of Cerium Doping . . . . .	37
Figure 14	DSC Curve of 11.4% CeO <sub>2</sub> -ZrO <sub>2</sub> . . . . .	38
Figure 15	Transformation Temperatures of CeO <sub>2</sub> -ZrO <sub>2</sub> . . . . .	38
Figure 16	Pillar and Tip Geometry . . . . .	40
Figure 17	Superelastic Stress-Temp and Stress-Strain Diagrams . . . . .	41
Figure 18	Measured Superelastic Stress-Strain Response . . . . .	42
Figure 19	Austenite Shape Memory Stress-Temp . . . . .	43
Figure 20	Shape Memory Effect in Zirconia Micro-Pillar . . . . .	44
Figure 21	Martensite Stripes in Zirconia Micro-Pillar . . . . .	45
Figure 22	TEM Phase Identification of Bent and Heated Pillar . . . . .	45
Figure 23	Comparison of Superelasticity in Ceramics and Metals . . . . .	46
Figure 24	Comparison of Actuator Stress and Strain . . . . .	48
Figure 25	Comparison of Martensite Start Temperature of Various Shape Memory Materials . . . . .	49
Figure 26	Oligo-Polycrystalline Transition . . . . .	53
Figure 27	Bent Oligocrystalline Pillar . . . . .	54
Figure 28	Martensite Stripes on Compressed Pillar . . . . .	54

Figure 29	Transformation Stress and Strain versus Pillar Diameter . . . . .	56
Figure 30	Orientation Dependence in Cu-Al-Ni Alloys . . . . .	60
Figure 31	SEM and EBSD Map of Polycrystalline Grains . . . . .	61
Figure 32	Transition Temperatures for $xY_2O_3-5 \text{ mol\% TiO}_2-ZrO_2$ . . . . .	62
Figure 33	XRD Patterns for $xY_2O_3-5 \text{ mol\% TiO}_2-ZrO_2$ . . . . .	63
Figure 34	Micro-Pillar Before and After Compression . . . . .	67
Figure 35	Pillar Orientations on Standard Stereographic Triangle . . . . .	67
Figure 36	Orientation Dependent Mechanical Behavior of Pillars . . . . .	68
Figure 37	Theoretical vs. Measured Loading Modulus . . . . .	71
Figure 38	Theoretical vs. Measured Loading Modulus Stereographic Projection	72
Figure 39	Zirconia Tetragonal to Monoclinic Correspondences . . . . .	73
Figure 40	Orientation Dependence of Transformation Stress . . . . .	76
Figure 41	Measured Critical Stress vs. Schmid Factor for Correspondence C	77
Figure 42	Transformed and Cracked Pillar 6 . . . . .	79
Figure 43	Measured Critical Stress vs Schmid Factor with Normal Component	82
Figure 44	Orientation Dependence of Sample Size Effects . . . . .	84
Figure 45	Minimum Theoretical Compressive Strain Stereographic Triangle	86
Figure 46	Measured Compressive Strain vs. Theoretical Strain . . . . .	87
Figure 47	Oligocrystalline Macrostructures . . . . .	90
Figure 48	Particle Size Distribution of As-Precipitation and Dried/Calcined Powders . . . . .	91
Figure 49	Superelastic Load-Displacement Curves for Individual Particle .	92
Figure 50	Experimental Setup for Quasi-Static Powder Testing . . . . .	93
Figure 51	X-Ray Diffraction Patterns of Shape Memory Powders Before and After Compression . . . . .	94
Figure 52	X-Ray Diffraction Patterns of Superelastic Powders Before and After Compression . . . . .	95
Figure 53	X-Ray Diffraction Patterns of Intermediate Powders Before and After Compression . . . . .	97
Figure 54	Oligocrystalline Wire Schematic and Metal Wire . . . . .	98
Figure 55	Schematic of Typical Electrospinning Setup . . . . .	100
Figure 56	As-Deposited Electrospun Ceramic Wires . . . . .	100
Figure 57	Annealed Electrospun Ceramic Wires . . . . .	101
Figure 58	Freeze Casting Process . . . . .	104

Figure 59	Experimental Freeze Casting Setup . . . . .	105
Figure 60	SEM Micrographs of Shape Memory Ceramic Foams . . . . .	106
Figure 61	Differential Scanning Calorimetry Curves of Shape Memory Ceramic Foams . . . . .	107
Figure 62	Thin Film Schematic . . . . .	108
Figure 63	Sputter Deposition Rate of Oxide Targets . . . . .	110
Figure 64	Sputter Deposition Rate of Metallic Targets . . . . .	111
Figure 65	Sputtered Film Micrographs . . . . .	112
Figure 66	Phases in Films Produced from Oxide Targets . . . . .	113
Figure 67	Phases Present in Films Produced With Metallic Targets . . . . .	114
Figure 68	In-Situ Furnace GIXD of Thin Films . . . . .	115
Figure 69	Effective Diameter Diagram . . . . .	127
Figure 70	Stress-Strain Curves for Superelastic Pillar A . . . . .	129
Figure 71	Stress-Strain Curves for Superelastic Pillar B . . . . .	129
Figure 72	Stress-Strain Curves for Superelastic Pillar C . . . . .	130
Figure 73	Stress-Strain Curves for Superelastic Pillar D . . . . .	130
Figure 74	Stress-Strain Curves for Superelastic Pillar E . . . . .	131
Figure 75	Stress-Strain Curves for Superelastic Pillar F . . . . .	131
Figure 76	Stress-Strain Curves for Superelastic Pillar G . . . . .	132

## LIST OF TABLES

---

Table 1	Metallic Shape Memory Materials . . . . .	21
Table 2	Ceramics with Martensitic Transformations . . . . .	28
Table 3	Lattice Parameters of Pure Zirconia . . . . .	29
Table 4	Sintered Disk Composition . . . . .	36
Table 5	Phases of Sintered Ceramics . . . . .	37
Table 6	Orientation and Dimensions of Transformed Pillars 1-24 . . . . .	64
Table 7	Orientation and Dimensions of Transformed Pillars 25-31 . . . . .	65
Table 8	Orientation and Dimensions of Fractured Pillars . . . . .	65
Table 9	Mechanical Properties of Transformed Pillars 1-24 . . . . .	66



Table 10	Mechanical Properties of Transformed Pillars 25-31 . . . . .	68
Table 11	Mechanical Properties of Fractured Pillars 32-40 . . . . .	69
Table 12	Materials Parameters for the Calculation of the Theoretical Transformation Stress . . . . .	80
Table 13	Strain Parameters for the Calculation of the Theoretical Transformation Stress . . . . .	81
Table 14	FIB Milling Procedure . . . . .	126
Table 15	Superelastic Micro-Compression Stress-Strain Curves . . . . .	128

## ACRONYMS

---

**SME** Shape Memory Effect

**EBS** Electron Backscattered Diffraction

**SEM** Scanning Electron Microscopy

**FIB** Focused Ion Beam

**EDS** Energy Dispersive Spectroscopy

**XRD** X-Ray Diffraction

**DSC** Differential Scanning Calorimetry

**TMA** Thermomechanical Analysis

**GIXD** Grazing Incidence X-Ray Diffraction



## INTRODUCTION

---

Shape memory materials are a class of materials that exhibit two distinct thermo-mechanical phenomena:

1. The **shape memory effect (SME)** is the ability of a material to undergo apparent plastic deformation at low temperatures and then, upon heating, recall a specific predetermined shape that was set at a higher temperature.
2. **Superelasticity** is the ability to attain large, fully reversible strains in the range of 3-18% when exposed to a mechanical stress [1].

The mechanism underlying both of these phenomena is a martensitic phase transformation. This chapter will provide the necessary background information on martensitic transformations in terms of the mechanical response of the shape memory effect and superelasticity.

### 1.1 MARTENSITIC PHASE TRANSFORMATIONS

Martensitic transformations are diffusionless and reversible transformations between two different crystal structures. The atoms move small distances cooperatively, which results in a phase transformation, but the relative positions of the atoms with respect to each other do not change, i.e. they do not change place with one another. An additional requirement is that the phase transformation is associated with a volume or shape change. This last aspect is critical for shape memory materials because it is the shape change of the unit cell that leads to useful macroscopic shape changes.

As with most phase transformations, martensitic transformations are thermally induced, however martensitic transformations also have temperature hysteresis as shown in [Figure 1](#). There are four important temperatures during the transformation: martensite start ( $M_s$ ), martensite finish ( $M_f$ ), austenite start ( $A_s$ ), and

austenite finish ( $A_f$ ). If we start at a high temperature, above  $A_f$ , then the material is completely in the austenite phase. As we begin to cool the material we will reach the  $M_s$  temperature, where the austenite will begin to transform to martensite. If cooling is continued below  $M_f$  then all of the austenite will be transformed to martensite leaving a fully martensitic material. The austenite to martensite transition is known as the forward transformation.

Now if the martensite is heated, austenite will begin to form at  $A_s$  and then once the temperature is above  $A_f$  only austenite will remain. The martensite to austenite transition is known as the reverse transformation. The hysteresis is due to a balance between the chemical driving force that promotes the phase transformation and the elastic energy created by the shape change that hinders the transformation. Note that [Figure 1](#) shows  $A_s$  lower than  $M_s$ , however this is not always the case as  $A_s$  can be greater than  $M_s$ .

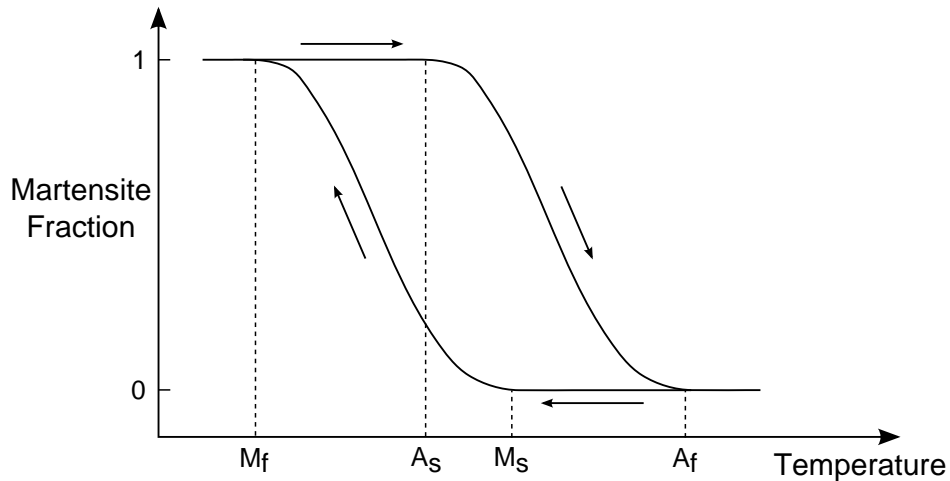


Figure 1: Temperature hysteresis of martensitic transformations showing that the forward and reverse transformations occur at different temperatures.

## 1.2 THE SHAPE MEMORY EFFECT

The [SME](#) is an apparent plastic deformation that can be fully recovered upon heating. A full shape memory cycle is presented in [Figure 2](#) showing a macroscopic specimen in the top half of the figure and the corresponding microscopic structure in the bottom half. Addressing the macroscopic behavior first, the cycle be-

gins by setting the memory shape under stress in the austenite phase above  $A_f$  (a). The specimen is then cooled and will go through a phase transformation to the martensite phase ( $a \rightarrow b$ ), but once transformed the macroscopic shape will remain essentially the same as the starting shape, a process known as self-accommodation. Then if the specimen is mechanically loaded ( $b \rightarrow c$ ) it will be physically deformed and when it is unloaded it will retain the deformed shape. If the sample is subsequently heated ( $c \rightarrow d$ ) it will go through the phase transformation to austenite and it will revert back to the original shape. This is known as the one-way shape memory effect, since the material can only remember the high temperature shape when heated.

The mechanism for the shape memory effect can be described in terms of the crystal structures of the two phases and is shown in the lower part of [Figure 2](#). Here the austenite phase is represented schematically in 2D as a rectangular lattice and the martensite as an oblique lattice. Upon cooling from the austenite phase, the material transforms into martensite but it does so in a self-accommodating way, so that the overall shape of the object does not change (b). This involves many different twin variants which have the same martensitic crystal structure but with different alignments. If the martensite is now deformed, some twin variants will become preferred, due to the applied stress, and they will remain upon unloading (c). When the sample is heated again the martensite will transform to austenite and it will recover the original shape (d).

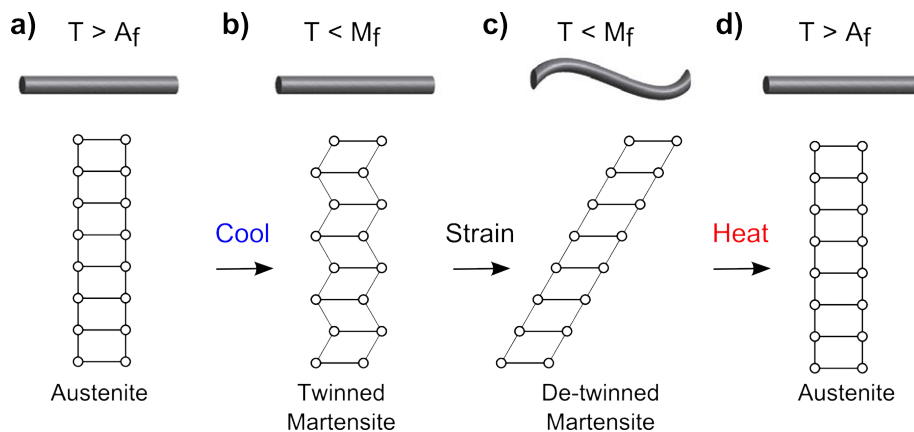


Figure 2: Schematic of the shape memory effect in a macroscopic specimen (top) and in the crystal structure (bottom). The austenite is represented as a rectangular lattice and the martensite as an oblique lattice.

## 1.3 SUPERELASTICITY - STRESS INDUCED TRANSFORMATIONS

In addition to being thermally induced, martensitic transformations can also be induced by the application of stress, which leads to the phenomenon known as superelasticity. If the material is stressed in its austenitic state, above  $A_s$ , then the austenite will be transformed into martensite. Once the load is removed however, the material transforms back to the austenite phase, since that is preferred thermodynamically, and reverts back to its original shape. This results in a large recoverable strain and a stress-strain curve that shows hysteresis behavior, [Figure 3](#), where the area inside the hysteresis loop is energy lost during the transformation and is related to the damping capacity. The transformation stresses are labeled on the diagram ( $\sigma^{M_s}$ ,  $\sigma^{M_f}$ ,  $\sigma^{A_s}$ ,  $\sigma^{A_f}$ ) corresponding to the martensite/austenite start and finish stresses which are analogous to the martensite start and finish temperatures. Superelasticity is often used interchangeably with the term pseudoelasticity. Here superelasticity will be used to describe elastic behavior but a more detailed description of the terminology is given by Otsuka [1].

To obtain superelasticity, the stress required to induce the austenite to martensite transformation must be less than the critical stress to induce slip. If slip occurs before the phase transformation then the deformation will not be recoverable upon unloading and will result in permanent deformation. [Figure 4](#) shows a typical stress-temperature diagram where the lines of positive slope separate the plot into austenite (right) and martensite (left) regions. There are four lines for each of the important transformation temperatures. If we start at point 1, in the fully austenitic state, and begin to apply a stress, then we will pass through the  $A_f$  and  $A_s$  lines and nothing will change because the material remains austenitic. Once we reach the stress level to pass the  $M_s$  line, point 2, the stress induced martensite transformation will start and will complete after passing through the  $M_f$  line where the material will be completely martensite, point 3. If the material is unloaded then it will transform back to austenite and the original shape. The line with negative slope indicates the critical stress required for slip, and it must be greater than the stress required to induce the martensitic transformation,  $\sigma^{M_s}$ , otherwise superelasticity will not be observed.

The slope of the transformation lines on the stress-temperature diagrams can be calculated using a modified Clausius-Clapeyron relation,

$$\frac{d\sigma}{dT} = -\frac{\Delta H}{\Delta\epsilon T} \quad (1)$$

where  $\Delta H$  is the enthalpy of the transformation and  $\Delta\epsilon$  is the change in strain of the transformation. The slope of the transformation lines can be calculated from the enthalpy of the transformation and the strain change, and this can be compared to the experimentally measured stresses required to induce the transformation [2, 3].

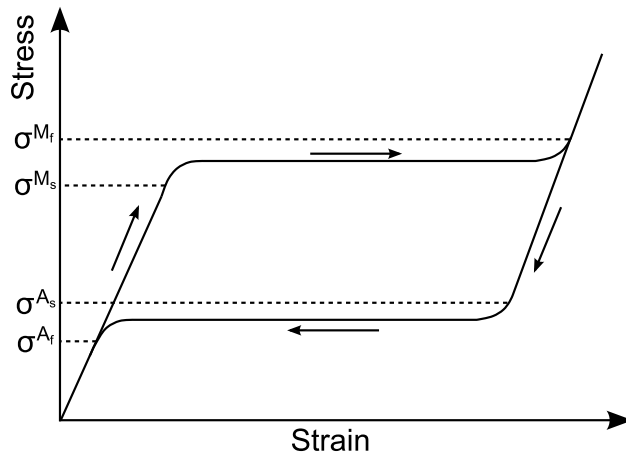


Figure 3: Schematic superelastic hysteresis stress-strain curve with the transformation stresses shown. After loading the material has no permanent plastic deformation but the area within the curve indicates energy was dissipated.

#### 1.4 HISTORY AND APPLICATIONS OF SHAPE MEMORY MATERIALS

The first discovery of the phenomenon known as the shape memory effect in Au-Cd alloys is usually attributed to Chang and Read in 1951 [4], although other earlier researchers contributed significantly to the discovery [5, 6]. The surprising ability of an inanimate material to remember a predetermined shape was immediately recognized as valuable and sparked a great deal of research. Between their original discovery and today, new alloy systems with shape memory properties have been discovered like Ni-Ti in 1963 [7] as well as many other systems such as Cu-Zn, Fe-Pt, and Cu-Al-Ni [8]. Table 1 lists some of the metal alloys that demon-

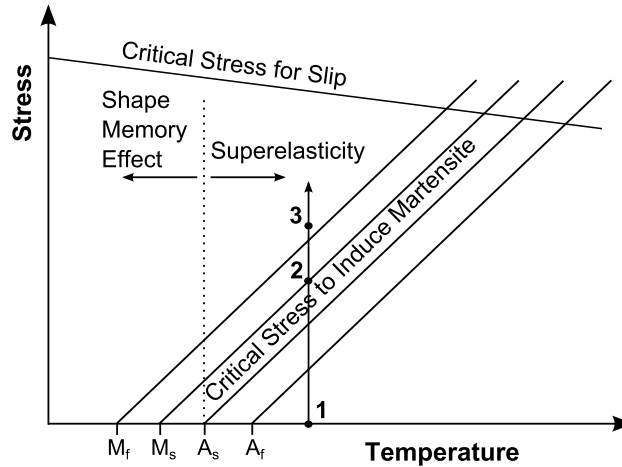


Figure 4: Stress-temperature diagram for a shape memory material the shape memory effect is seen at low temperatures while superelasticity is seen at high temperatures.

strate the SME and superelasticity. A large amount of information has been gathered on the phase transformations and can be found in the literature [1, 9].

Shape memory materials have been used extensively as actuators and couplings. Actuators convert an input signal into some kind of mechanical motion, such as making an electrical connection or closing a valve. Since shape memory materials naturally produce a shape change, they can use a temperature change as their input to create a mechanical motion. The temperature change can be ambient temperature changes or externally induced temperature changes (heating). However, when dealing with the one-way shape memory effect, they require another mechanism to return the part back to the original shape which is normally done with a spring.

Couplings join two objects together with a tight and semi-permanent connection. Shape memory materials are ideal for this application because they generally only require one transformation cycle. However since each coupling needs to be made custom for a given connection they tend to be rather expensive. Many of the newest applications of shape memory materials are in the biomedical industry including dental braces and medical stents [10].

Applications of superelasticity utilize the large recoverable strains that are possible and include flexible eyeglasses, dental braces, and antennae [1]. Since the



Table 1: Metallic alloys that demonstrate the shape memory effect and superelasticity [8].

ALLOY	COMPOSITION (AT%)	STRUCTURAL CHANGE
Ag-Cd	44-49 Cd	B2 $\rightarrow$ 2H
Au-Cd	46.5-50 Cd	B2 $\rightarrow$ 2H
Cu-Zn	38.5-41.5 Zn	B2 $\rightarrow$ M9R
Cu-Al-Zn	26-28 Al, 3-4.5 Ni	DO <sub>3</sub> $\rightarrow$ 2H
Ni-Al	36-38 Al	B2 $\rightarrow$ 3R
Ni-Ti	49-51 Ni	B2 $\rightarrow$ Monoclinic
Fe-Pt	25 Pt	L1 <sub>2</sub> $\rightarrow$ Ordered BCT

superelastic stress-strain curve is hysteretic, energy is dissipated during each cycle, which leads to the possibility of energy dissipating applications.

## 1.5 OLIGOCRYSTALLINE STRUCTURES TO ELIMINATE BRITTLE FRACTURE

A valuable characteristic for applications of shape memory materials is the ability to be cycled many times, whether through shape memory heating cycles or superelastic stress cycles. Some bulk materials (in polycrystalline form) lack the ability to go through multiple transformation cycles due to brittle fracture that occurs because of the transformation [11]. Note that the cycling ability referred to here is different from high cycle fatigue issues that occur after thousands or millions of cycles; here we are talking about tens to hundreds of cycles. One possible mechanism for the brittle fracture is incompatibilities between neighboring grains in a polycrystalline material. As one grain transforms and therefore changes shape, it will build up stress with adjacent grains and this stress can cause intergranular fracture [11]. Some examples of brittle shape memory materials are copper based shape memory alloys as well as zirconia shape memory ceramics [12].

One way to prevent this type of brittle intergranular fracture is through microstructure control. It is possible to remove the physical constraints around a grain by removing neighboring grains altogether. The most straightforward way to remove grain boundaries is to make a single crystal which, by definition has no grain boundaries. But there are other structures that can be fabricated that have very few grain boundaries, compared to polycrystals, that can reduce or eliminate grain boundary incompatibilities, namely oligocrystalline structures.

Oligocrystalline structures can be broadly described as having very few grains, in other words somewhere between a polycrystalline material with many grains and a single crystal with only one grain. An example of an oligocrystalline architecture is a bamboo structure where the grains of the material span the entire cross-section of the material. A structure like this can have many total grains, but in any given region there are very few. The structural value is that each grain has access to a free surface and therefore is not fully constrained by surrounding grains, allowing the transformation to occur without stress build-up between grains and avoiding fracture. The informal definition of an oligocrystal is a material with a low number of grains relative to its volume [13, 14, 15], however a more quantitative definition was provided by Ueland et al; a structure in which the total surface area exceeds the total grain boundary area [16].

The concept of microstructure engineering of oligocrystalline structures has been applied to brittle copper based shape memory metals [11, 17]. Figure 5 shows examples of different microstructures in Cu-Al-Ni microwires. Figure 5d is a completely polycrystalline structure that exhibited brittle fracture on the first superelastic cycle. This can be contrasted to a single crystal, Figure 5a, that showed near ideal superelastic behavior and was able to be cycled many times. A wire with a near oligocrystalline structure shown in Figure 5c, which showed better superelastic cycling ability than the polycrystal but still fractured after several cycles. An ideal bamboo structure, shown in Figure 5b, had properties approaching those of the single crystal, and exhibited many cycles without fracture. These results clearly show the advantages of applying microstructure engineering to brittle shape memory materials as it can reduce and eliminate the stress concentrations that lead to brittle fracture. This will expand the number of available shape memory materials for use in practical applications.

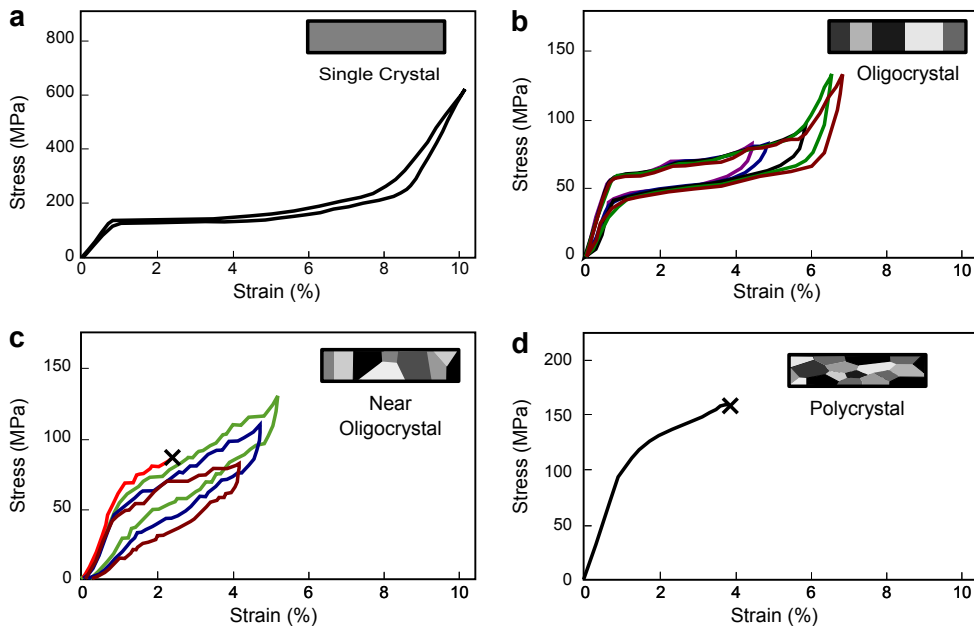


Figure 5: Superelastic stress-strain curves for a Cu-Al-Ni (a) bulk single crystal, (b) oligocrystalline microwire, (c) near oligocrystalline microwire, and (d) polycrystalline microwire. The oligocrystals and single crystals can be cycled many times without failure [16].

## 1.6 SAMPLE SIZE EFFECTS

In addition to the improved fracture properties that are demonstrated by oligocrystalline structures there are also some changes in the materials properties due to the small sample sizes that are typically associated with oligocrystals. Norwich has shown that small diameter Ni-Ti wires have increased fatigue performance in the superelastic range, although the wires were polycrystalline [18]. Chen et al. [11] showed that there is a size effect for the transformation stresses, transformation temperatures, and for the energy dissipation during superelastic cycling for small single crystal pillars and oligocrystalline (bamboo) wires of Cu-Al-Ni, which is demonstrated by the superelastic stress-strain curves in Figure 6. They propose several explanations for the size effects that include surface energy, stored elastic energy, acoustic emission, heat transfer, and internal friction. However, the analysis rules out all of the mechanisms except heat transfer and internal friction. The heat transfer mechanism dominates in larger diameter samples

where heat can not be exchanged with the environment quickly enough, which results in a temperature increase in the sample. This temperature increase stabilizes the austenite phase and results in larger stresses to induce the transformation which increases the hysteresis. The internal friction mechanism dominates in small diameter samples where the free surfaces act as pinning sites or obstacles that retard the transformation and cause an increase in the hysteresis as the diameter decreases [11].

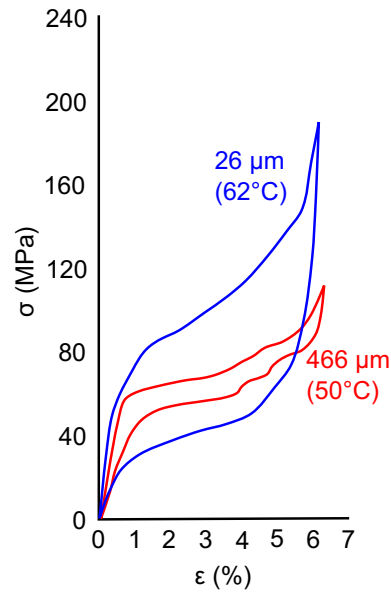


Figure 6: Superelastic stress-strain curves for two Cu-Al-Ni microwires with 26  $\mu\text{m}$  diameter (blue) and 466  $\mu\text{m}$  diameter. The small diameter wires show increased damping capacity, adapted from [11].

## 1.7 RESEARCH OBJECTIVES AND OUTLINE OF THESIS

All of the background material presented so far in Chapter 1 has been described to illustrate the idea of microstructure engineering of oligocrystalline and single crystal structures to improve the performance of brittle shape memory materials. The rest of the thesis will focus on extending these concepts to ceramic shape memory materials which also suffer from brittle fracture. To date, no studies have been carried out on shape memory ceramics to prove that oligocrystalline struc-

tures can successfully eliminate the issues of cracking and fracture. The structure of this thesis is as follows:

#### CHAPTER 2

First a suitable ceramic material, zirconia, was chosen that had the requisite martensitic transformation. Micron-scale single crystal structures were fabricated and tested to demonstrate their ability to cycle many times without brittle failure. The shape memory effect was demonstrated for the first time in a small scale shape memory ceramic achieving up to 7% strain without any signs of cracking. Dozens of superelastic cycles were also achieved, greatly improving upon the several cycles that are possible in polycrystals.

#### CHAPTER 3

This chapter takes the concept from Chapter 2 and more rigorously investigates the transition from single crystal to oligocrystal and finally up to polycrystal by varying the pillar diameter while keeping the grain size constant. As expected, the more polycrystalline the structure, the more likely it was to undergo cracking. A new size effect trend was observed for shape memory ceramics, where the transformation stress increased as pillar diameter increases, which was the opposite of what is observed in metals. It is proposed that the explanation for this new size effect has to do with the significantly higher stiffness of ceramics which causes the elastic stored energy to be larger contributor to the total free energy driving the transformation.

#### CHAPTER 4

Single crystals and oligocrystals are expected to have anisotropic properties since the properties are not averaged by the large number of grains typically found in polycrystals. Therefore a thorough exploration of the effect of crystal orientation was carried out to determine the effect on properties such as elastic modulus, transformation stress, transformation strain, and fracture behavior. It was revealed that certain orientations are indeed more likely to fracture and some orientations even exhibited crystal slip at room temperature. The crystallographic theory was used to compare with the measured experimental results. Orientation maps were produced that will aid in the design of future optimized shape memory ceramics.

## INTRODUCTION

### CHAPTER 5

For the scientific investigations of Chapters 2, 3, and 4, micro-pillar specimens were used for their ease of fabrication and uniform geometry ideal for probing mechanical properties. However, micro-pillars are not ideal for most applications due to their limited size. In this chapter, several large scale architectures were investigated that still maintain micro-scale oligocrystalline features such as powders, wires, foams, and thin films. Processing techniques were developed for each structure, test specimens were fabricated and the shape memory properties were explored. These structures are the likely future for applications of shape memory ceramics.

### CHAPTER 6

This chapter summarizes all the work that was carried out and presents opportunities for future work to further develop the field of shape memory ceramics.

## SHAPE MEMORY CERAMICS IN SMALL VOLUMES

---

Some ceramic materials have martensitic phase transformations and are therefore expected to demonstrate shape memory properties, notably zirconia based ceramics. To date, however, all shape memory behavior in ceramics has been hindered by brittle fracture after several transformation cycles. In this chapter we survey some of the candidate ceramic shape memory materials, ultimately choosing zirconia as the test case to explore the use of microstructure engineering to eliminate brittle fracture to create shape memory ceramics that can be cycled repeatedly.

*- This work done in collaboration with:  
Dr. Zehui Du and Xiaomei Zeng at Nanyang Technological University*

### 2.1 SHAPE MEMORY CERAMIC MATERIALS

Many ceramics have martensitic transformations similar to those found in metallic shape memory alloys and therefore can exhibit the shape memory effect and superelasticity with the same mechanism. Each material has a parent phase (austenite) and martensite phase and there is an associated shear angle and volume change that accompanies the transformation between the two. A list of potential shape memory ceramics is given in [Table 2](#) [19]. In general a larger shear angle will result in a larger shape change but other factors must also be considered like ease of fabrication and the transformation temperatures. After reviewing the potential options, zirconia was chosen as the first ceramic to study in this work for the following reasons:

- Zirconia has a well studied and well characterized martensitic transformation between a tetragonal phase (austenite) and a monoclinic phase (martensite) [20, 21, 22].
- The transformation temperatures can be easily modified between 25-1100°C by doping with other oxides such as yttria, ceria, and magnesia [22].

- It can be fabricated by conventional ceramic processing techniques [23, 24].
- Shape memory properties have been demonstrated in polycrystalline zirconia but brittle fracture occurred after five superelastic cycles [12].

Table 2: Ceramic materials that have martensitic transformations. The shear angle and the volume change impact the extent of the shape memory properties [19].

CERAMIC	PARENT PHASE (SPACE GROUP)	MARTENSITE (SPACE GROUP)	SHEAR ANGLE	$\Delta V/V_o$
$Al_2SiO_5$	Sillimanite ( $Pbnm$ )	Kyanite ( $P\bar{1}$ )	$26.1^\circ$	-0.110
$Ca_2SiO_4$	Ortholarmite, $\alpha'$ ( $Ccm2_1$ )	Cinolarmite ( $P112_1/n$ )	$4.5^\circ$	-0.035
$Mg_2SiO_4$	Olivine ( $Pbnm$ )	Spinel, $\gamma$ ( $Fd\bar{3}m$ )	$19.9^\circ$	-0.085
$Mg_2SiO_4$	Spinel, $\gamma$ ( $Pbnm$ )	$\beta$ -phase ( $Fd\bar{3}m$ )	$40.9^\circ$	+0.024
$ZrO_2$	Baddeleyite, tet ( $P4_2/nmc$ )	Baddeleyite, mono ( $P2_1/c$ )	$8.78^\circ$	+0.031
$ZnS$	Wurtzite ( $P6_3mc$ )	Sphalerite ( $F\bar{4}3m$ )	$19.5^\circ$	+0.001

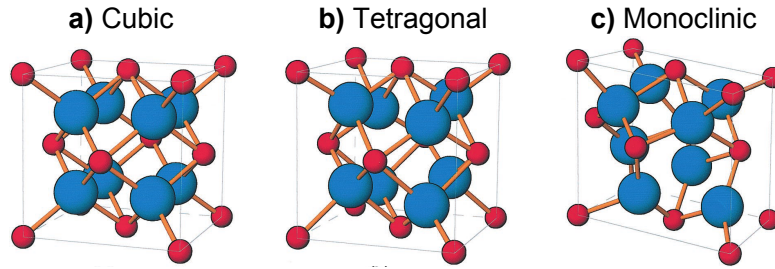
## 2.2 ZIRCONIA AS A SHAPE MEMORY CERAMIC

As mentioned in the previous section, zirconia has many attributes that make it ideal for study as a shape memory ceramic. Here, further depth will be provided on the details of the transformations in zirconia, the effect of doping, and the known shape memory properties.



## 2.2.1 The Martensitic Transformation in Zirconia

Pure zirconia ( $\text{ZrO}_2$ ) has three different solid phases that exist in different temperature ranges and their crystal structures are shown in Figure 7. The cubic phase ( $\text{Fm}\bar{3}\text{m}$ ) is stable at temperatures greater than  $2360^\circ\text{C}$ , the tetragonal phase ( $\text{P4}_2/\text{nmc}$ ) occurs between  $1170^\circ\text{C}$  and  $2360^\circ\text{C}$ , while the monoclinic phase ( $\text{P2}_1/\text{c}$ ) is present below  $1170^\circ\text{C}$  [20, 22]. The lattice parameters for each phase in pure zirconia are given in Table 3. The transformation between the tetragonal and monoclinic phases only involves slight shifts of atoms and all atoms maintain their relative positions but there is a significant shear strain of  $\sim 8\%$  and a volume change of  $\sim 4\%$  [19].



The tetragonal cell in Figure 7 is actually a double FCT cell, but the primitive cell is BCT

Figure 7: The crystal structures of zirconia include (a) cubic, (b) tetragonal, and (c) monoclinic phases. Adapted from [20].

Table 3: Lattice parameters of pure zirconia at room temperature [25] and at elevated temperatures [26].

TEMPERATURE	PHASE	LATTICE PARAMETERS (nm)
25°C	Monoclinic ( $\text{P2}_1/\text{c}$ )	$a = 5.1501$
		$b = 5.2077$
		$c = 5.3171$
		$\beta = 99.224^\circ$
1160°C	Tetragonal ( $\text{P4}_2/\text{nmc}$ )	$a = 5.1435$
		$c = 5.2689$
2230°C	Cubic ( $\text{Fm}\bar{3}\text{m}$ )	$a = 5.269$

### 2.2.2 Transformation Toughening of Zirconia

Before 1975, zirconia had few practical applications mainly due to the phase transformation between the tetragonal phase to the monoclinic phase that, upon cooling, lead to brittle fracture in the material [20]. One of the most important applications of zirconia came about as a direct result of the martensitic transformation itself, in so-called transformation toughened ceramics. Here the transformation from tetragonal to monoclinic was used to prevent crack propagation and make zirconia mechanically tougher. The general concept used metastable regions of tetragonal zirconia that were metastable due to compressive forces within the specimen. When a crack was opened near a metastable tetragonal region, the compressive stress would be released and the region would transform to the monoclinic phase, change shape, and expand in volume. It was this volume change that specifically helped to close the crack and prevent crack propagation thereby increasing the toughness. This was first discovered by Garvie, Hannink, and Pascoe in their landmark 1975 letter [27]. Because of the practical applications of transformation toughened ceramics there is a wealth of information on the factors that affect transformation toughening of ceramics such as the tetragonal phase grain size, distribution, and the processing [21].

### 2.2.3 Doping Elements

As noted earlier pure zirconia transforms from the monoclinic phase to tetragonal phase upon heating at  $1170^{\circ}\text{C}$ , but we have the ability to alter the transformation temperature by doping zirconia with oxides such as magnesia, hafnia, titania, ceria, and other oxides. The alloying oxides act to stabilize the high temperature phase (austenite) thereby lowering the transformation temperature. If the doping is increased it is even possible to stabilize the very high temperature cubic phase at room temperature. [Figure 8a](#) shows a schematic equilibrium phase diagram for  $\text{ZrO}_2$  with a generic metal oxide. With small amounts of doping the monoclinic to tetragonal transformation temperature drops and it is possible to obtain a mixed monoclinic and cubic structure at room temperature. With the appropriate heat sintering schedule and faster cooling, metastable phases can be formed. A metastable phase diagram is shown in [Figure 8b](#); here the tetragonal phase is

retained at room temperature with adequate doping. Additionally mixtures of monoclinic and tetragonal phases can be preserved at room temperature for certain processing conditions; this is known as partially stabilized zirconia. The partially stabilized zirconias have much better thermal shock resistance and fracture toughness. Garvie found that partially stabilized zirconias that were processed to have retained tetragonal phase dispersed throughout the matrix were especially tough [28]. Higher doping concentrations will eventually lead to the cubic phase being stable at room temperature which is referred to as fully stabilized zirconia.

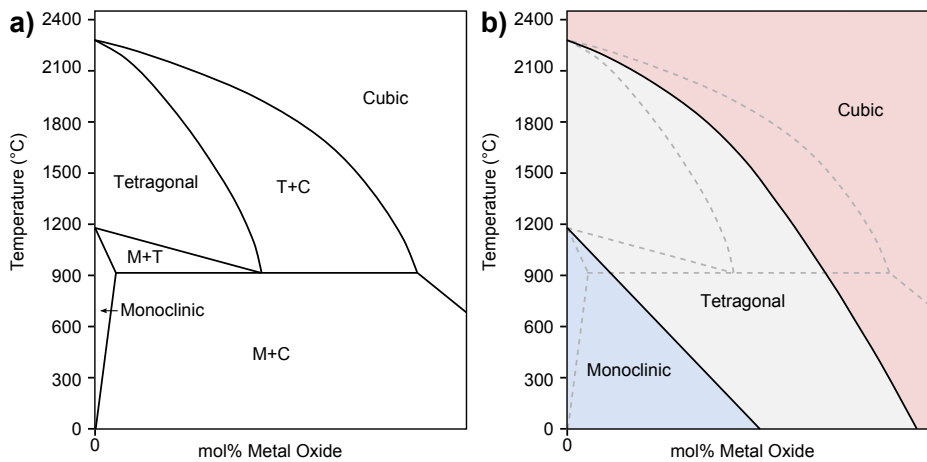


Figure 8: Schematic phase diagrams for  $ZrO_2$  and a metal oxide for a) equilibrium processing and b) metastable processing.

#### 2.2.4 Shape Memory Properties of Polycrystalline Zirconia

The martensitic transformation in zirconia makes it a good candidate for a shape memory ceramic material. Reyes-Morel investigated the shape memory effect in ceria-doped zirconia and found it to exhibit shape memory properties. Figure 9 shows a stress-strain curve for compression of  $CeO_2$ - $ZrO_2$  below the  $M_s$  temperature. The curve shows apparent permanent plastic deformation while subsequent heating recovers the strain, a classic demonstration of the shape memory effect. Reyes-Morel also investigated superelastic effects by carrying out compression tests above the  $A_f$  temperature with the stress-strain curve shown in Figure 10. The curve shows a classic hysteresis loop that is indicative of superelasticity [12].

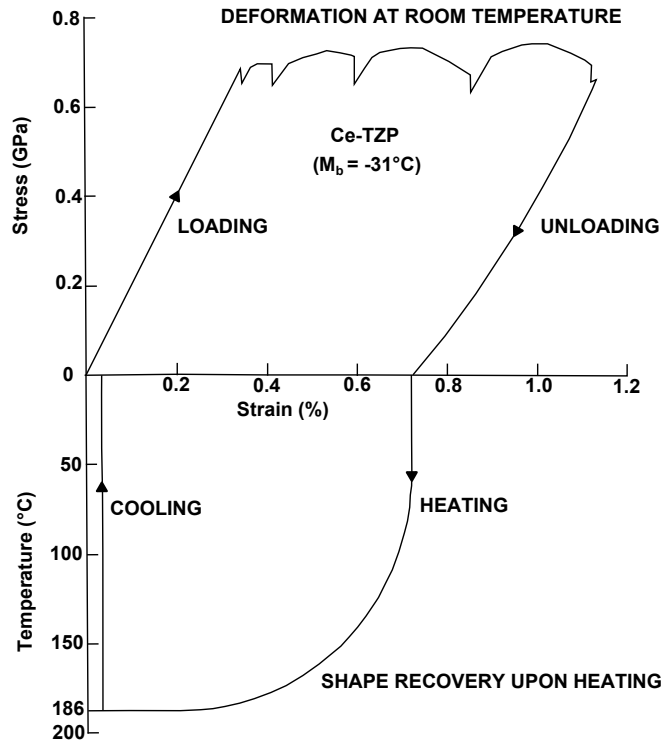


Figure 9: The shape memory effect in  $\text{CeO}_2\text{-ZrO}_2$  where deformation while in the martensite phase, below  $M_s$ , lead to permanent deformation. Subsequent heating above  $A_f$  resulted in shape recovery [12].

While the first shape memory and superelastic cycles show classic behavior, further testing revealed a degradation of the properties and eventually failure altogether. Reyes-Morel repeated the uniaxial compression tests in the superelastic regime for polycrystalline  $\text{CeO}_2\text{-ZrO}_2$  to determine the cyclic properties. Figure 11 shows the first four test cycles where each successive cycle the hysteresis loop becomes smaller and smaller until the specimen eventually failed on the fifth cycle. The failure was attributed to intergranular cracking and not to inherent limitations of the the cyclability of the transformation. Reyes-Morel even specifically claim that these ceramics would make good shape memory materials if the grain and interface cracking could be mitigated. To date, the superelastic cycling ability of  $\text{CeO}_2\text{-ZrO}_2$  has been limited to several cycles, and this was the driving force to apply microstructure control techniques to improve upon their shape memory properties [12].

## 2.2 ZIRCONIA AS A SHAPE MEMORY CERAMIC

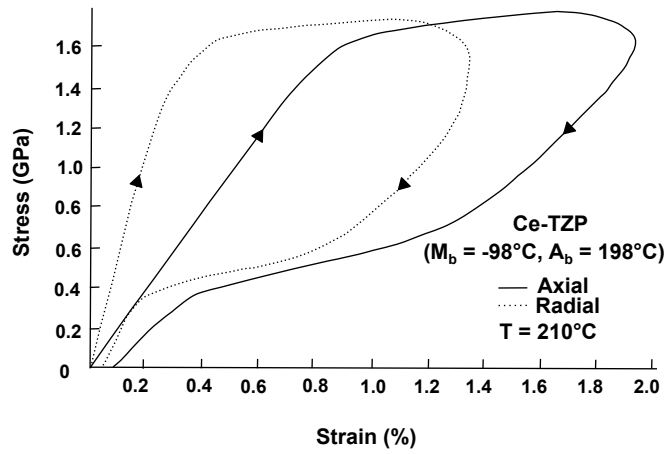


Figure 10: Superelastic behavior in  $\text{CeO}_2\text{-ZrO}_2$  showing almost complete strain recovery. Here  $M_b$  is equivalent to  $M_s$  and  $A_b$  is equivalent to  $A_s$  [12].

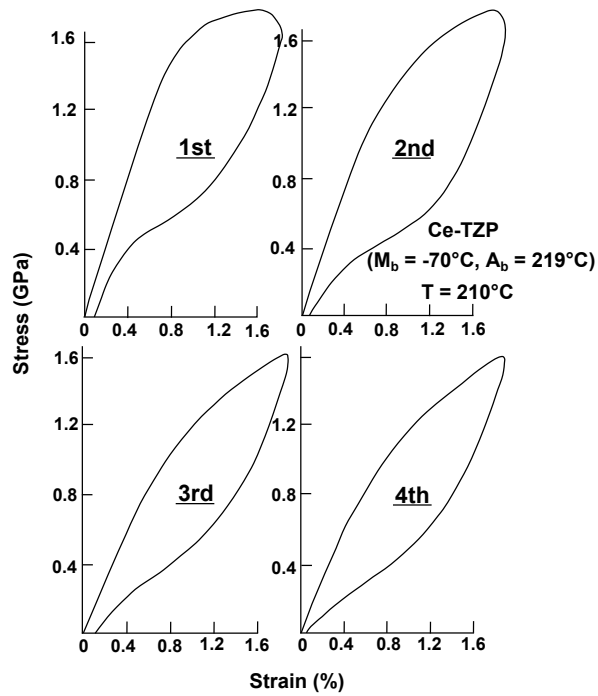


Figure 11: Axial superelastic stress-strain curves for  $\text{CeO}_2\text{-ZrO}_2$  showing diminishing hysteresis with each cycle, the 5th cycle resulted in failure [12].

### 2.3 SHAPE MEMORY CERAMICS IN SMALL VOLUMES

The concept of microstructure engineering to reduce or eliminate brittle fracture in shape memory metals was introduced in [Section 1.5](#) but now we wish to extend that concept to shape memory ceramics. The goal is to reduce the grain constraints that lead to internal stresses and eventual fracture. The general hypothesis can be summarized as,

*In ceramics that undergo martensitic transformations, a single crystal or oligocrystalline structure will relieve the stress concentrations generated by the phase transformation and mismatch between neighboring grains, thereby permitting cyclic transformation without cracking.*

The remainder of this chapter will focus on the creation of shape memory ceramics in small volumes and the subsequent characterization of their mechanical properties.

### 2.4 FABRICATION AND CHARACTERIZATION OF POLYCRYSTALLINE ZIRCONIA

As noted in [Section 2.2.3](#), doping zirconia with other metal oxides is a way to manipulate the transformation temperatures in order to produce samples that can be tested for all shape memory properties at room temperature. In this work the first doping element investigated was ceria as there is great amount of technical data in the literature about ceria-doped zirconia, and its properties and processing [[25](#), [29](#), [30](#)]. A co-precipitation technique was used to produce mixed powders by first mixing cerium and zirconium containing salts ( $\text{ZrOCl}_2 \cdot 8\text{H}_2\text{O}$  and  $\text{Ce}(\text{NO}_3)_3 \cdot 6\text{H}_2\text{O}$ ) in water followed by precipitation in 25 vol% ammonium hydroxide [[23](#), [24](#), [31](#)]. This method produced thoroughly mixed nano-sized particles which were then rinsed with DI water to remove any salt ions followed by ethanol rinsing and finally drying and calcination. During drying and calcination the powders tended to agglomerate and form micron sized particles on order of 15  $\mu\text{m}$ . A full description of the powder making process is given in [Section A.1](#)

The dry powders were formed into 6 mm diameter disks using uniaxial pressing at 3000 lbs of force resulting in disks several millimeters thick. The disks were

sintered at 1500°C for 10 hours with an 8°C/min ramp rate. A variety of different nominal compositions of sintered compacts were fabricated to produce a range of samples with different transformation temperatures.

The sintered ceramic disks were polished to reveal the grain size which is shown in the scanning electron microscope (SEM) image in Figure 12 and the grain size was measured as between 5-10  $\mu\text{m}$ . This grain size was large enough so that the final 1  $\mu\text{m}$  diameter micropillars should be comprised of only one grain.

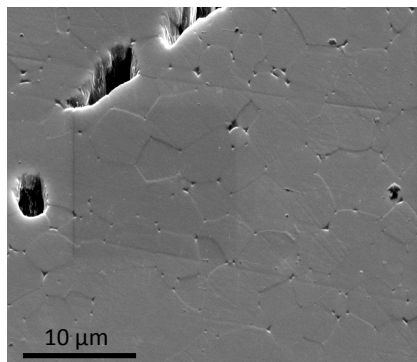


Figure 12: Grains in polycrystalline CeO<sub>2</sub>-ZrO<sub>2</sub>.

The composition of the sintered disks was measured using energy dispersive spectroscopy (EDS) and the results are given in Table 4. The nominal composition refers to the ratio of the metal salts that were mixed during powder processing.

Identification of the different phases present was done with x-ray diffraction (XRD) which can also quantitatively indicate the amount of each phase present [32]. The x-ray diffraction patterns for all compositions are shown in Figure 13 along with reference patterns for the monoclinic and tetragonal phases. Rietveld refinement was completed on the x-ray patterns to quantify the amount of each phase present for each composition and is summarized in Table 5.

The transformation temperatures for each composition were measured using a differential scanning calorimeter (DSC). An example curve showing the transformation peaks for 11.4% CeO<sub>2</sub>-ZrO<sub>2</sub> is shown in Figure 14 with the forward transformation occurring near 175°C and the reverse transformation near 375°C. Curves like this were collected for every composition. However once the ceria content was greater than 14.4%, no peaks were observed indicating that the tetragonal phase was retained to room temperature and is further evidenced by the XRD analysis. To further probe the transformation temperatures, the sintered

Table 4: Comparison of nominal composition of prepared powders (ratio of metal salts) and composition of sintered disks measured by EDS.

NOMINAL COMPOSITION (at%)	MEASURED CONCENTRATION (at%)
9	6.9
15	11.4
17	12.6
19	14.4
21	15.9
27	20.7

disks were run through a heating cycle using a thermomechanical analyzer (TMA) to measure the strain as the material transforms, providing an alternative method to measure the transformation temperatures. Again, above 14.4% CeO<sub>2</sub>, no measurable transformation was detected, but the TMA data matches well with the DSC data as can be seen in Figure 15. Here the measured data is plotted along with values from the literature [29] for the transformation temperatures of ceria doped zirconia, both showing good agreement.



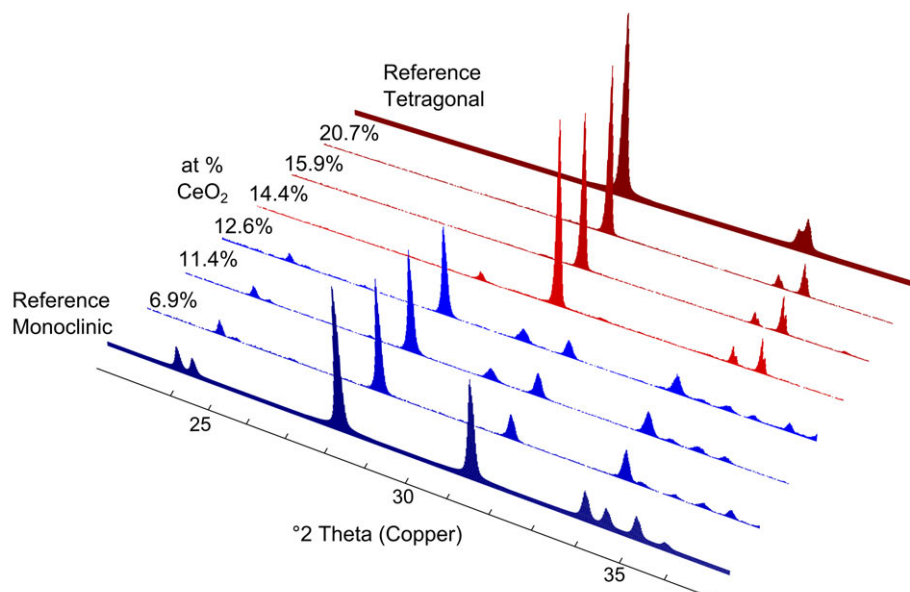


Figure 13: XRD patterns for each composition of CeO<sub>2</sub>-ZrO<sub>2</sub> and reference patterns for the pure monoclinic and tetragonal phases.

Table 5: Phases present in different compositions of sintered ceramics as measured by XRD.

MEASURED COMPOSITION (at% Ce)	PERCENT MONOCLINIC PHASE	PERCENT TETRAGONAL PHASE
6.9	98	2
11.4	93	7
12.6	84	16
14.4	7	93
15.9	0	100
20.7	0	100

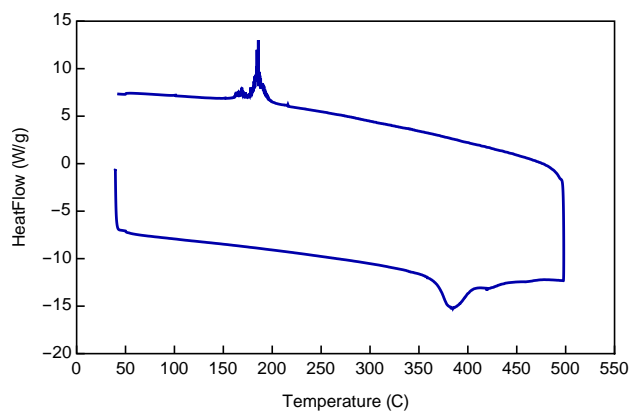


Figure 14: DSC curve for 11.4% CeO<sub>2</sub>-ZrO<sub>2</sub> showing forward and reverse transformation peaks.

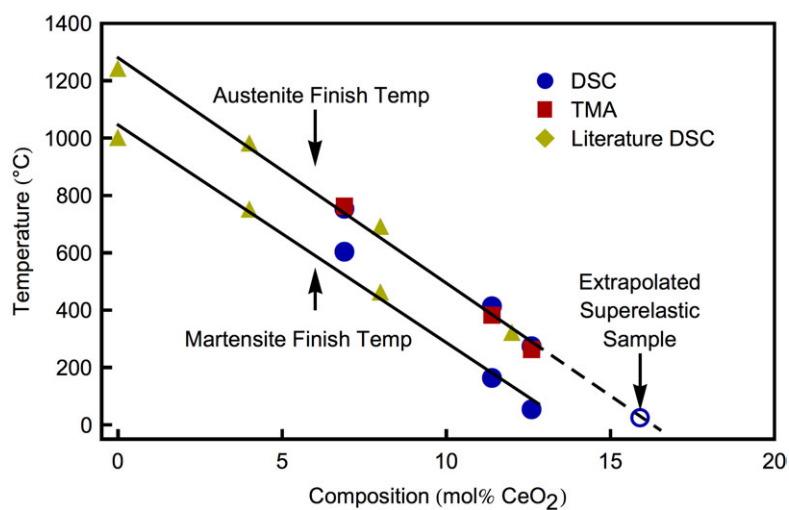


Figure 15: Measured [33] and literature [29] values for the transformation temperatures of CeO<sub>2</sub>-ZrO<sub>2</sub>.

## 2.5 FABRICATION OF SINGLE CRYSTAL MICRO-PILLARS

After sintering, the polycrystalline disks were polished flat using standard metallography techniques and then the flat substrates were used to fabricate single crystal micro-pillars. Micro-machining was performed with focused ion beam milling (FIB) to make micro-pillars from individual grains. The method used an ion beam, composed of gallium ions, that is directed normal to the substrate surface, to remove material leaving behind a cylindrical pillar [34, 35, 36]. If single crystal pillars are desired then the polycrystalline grain size is the limiting factor for how large the pillars can be. In an ideal micro-compression test, the aspect ratio should be between 2-3 in order to avoid pillar buckling [37]. This, combined with the polycrystalline grain size of 5-10  $\mu\text{m}$ , limits our pillar diameter to less than approximately 2  $\mu\text{m}$ . Note that in this section the crystal orientation of the grains was not accounted for; this will be addressed in Chapter 4.

## 2.6 MECHANICAL TESTING OF SINGLE CRYSTAL MICRO-PILLARS

The mechanical properties of the pillars were examined using nanomechanical testing techniques. This provided load-displacement data that was converted to stress-strain curves that were used to determine the Young's modulus, transformation stress, and transformation strain. This method has been used to explore pure metals [34, 36], intermetallic alloys [34], metallic glasses [38], naturally occurring biominerals [39], and shape memory metals [17, 40]. However we believe this is the first time it has been attempted with a shape memory ceramic material.

In this work a 20  $\mu\text{m}$  diameter cono-spherical tip was used to compress the pillars. The reason a cono-spherical tip was used instead of a flat punch was so the tip could still be used for scanning probe imaging which aides in centering the tip on the center of the pillar. A large trench was milled around the pillar to prevent the tip from contacting the bulk surface surrounding the pillar. [Figure 16](#) presents a schematic of the pillar-tip geometry.

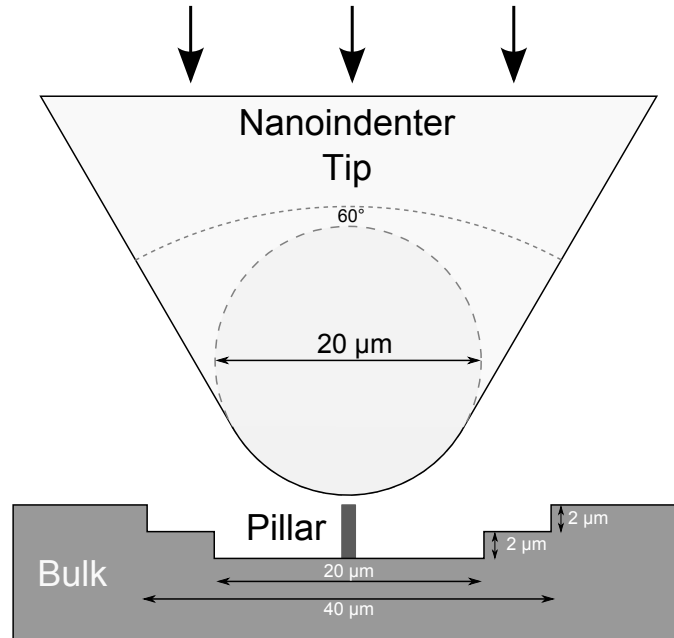


Figure 16: Geometry of the pillar and nanoindenter tip used during microcompression.

## 2.7 SUPERELASTIC BEHAVIOR OF SINGLE CRYSTAL MICRO-PILLARS

In order to investigate the superelastic properties of small scale zirconia, the 15.9% CeO<sub>2</sub> composition was selected since it is comprised of only the tetragonal phase, see [Table 5](#), which is the necessary starting phase to observe superelasticity. The stress-temperature diagram in [Figure 17a](#) illustrates where this composition is expected to lie at room temperature. If the stress is increased, we expect to pass through the phase transformation lines and thereby stress-induce martensite. The corresponding superelastic stress-strain curve that is expected is shown in [Figure 17b](#) with the characteristic forward and reverse transformation plateaus.

The experimental results did indeed match nicely with the expected mechanical behavior. The first loading and unloading cycle is shown in [Figure 18a](#) and there was an initial elastic loading section in the austenite phase. Once the critical stress to induce the phase transformation was reached, we saw a large strain plateau; in this case there were several strain plateaus possibly indicating that the transformation occurred in several steps. Upon unloading, there was another region of linear elastic response when the martensite was being unloaded elasti-

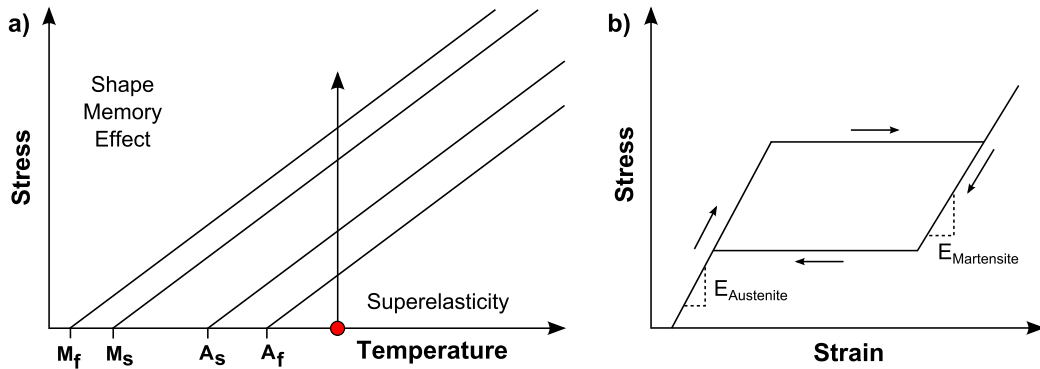


Figure 17: (a) Superelastic stress-temperature diagram with 15.9% Ce indicated by arrow at room temperature and (b) corresponding expected superelastic stress-strain diagram.

cally. Elastic unloading continued until another critical stress — that for reversion to austenite — is reached and then the martensite transformed back to austenite and another strain plateau was observed. Complete unloading lead to almost full strain recovery. Any residual strain was typically attributed to plastic deformation usually near the top of the pillar where the stresses were highest (due to pillar taper) and where there was a possibility to indent the top of the pillar resulting in permanent deformation.

Subsequent loading cycles of the same pillar are shown in [Figure 18b](#), [Figure 18c](#), and [Figure 18d](#) where similar superelastic behavior was seen but there is a clear gradual evolution of stress-strain curve. This behavior was expected with cycling as the material was "trained" to a particular kinematic pathway [41], i.e. different transformation variants became preferred for the specific stress state during compression.

The results shown in [Figure 18](#) were typical of the superelastic pillars that were tested and most were able to withstand at least dozens of transformation cycles with one pillar achieving 53 cycles. Stress-strain curves for other pillars can be found in [Section A.4](#). Obtaining dozens of cycles was a considerable improvement over polycrystalline superelastic zirconia which can only withstand several cycles before catastrophic failure [12].

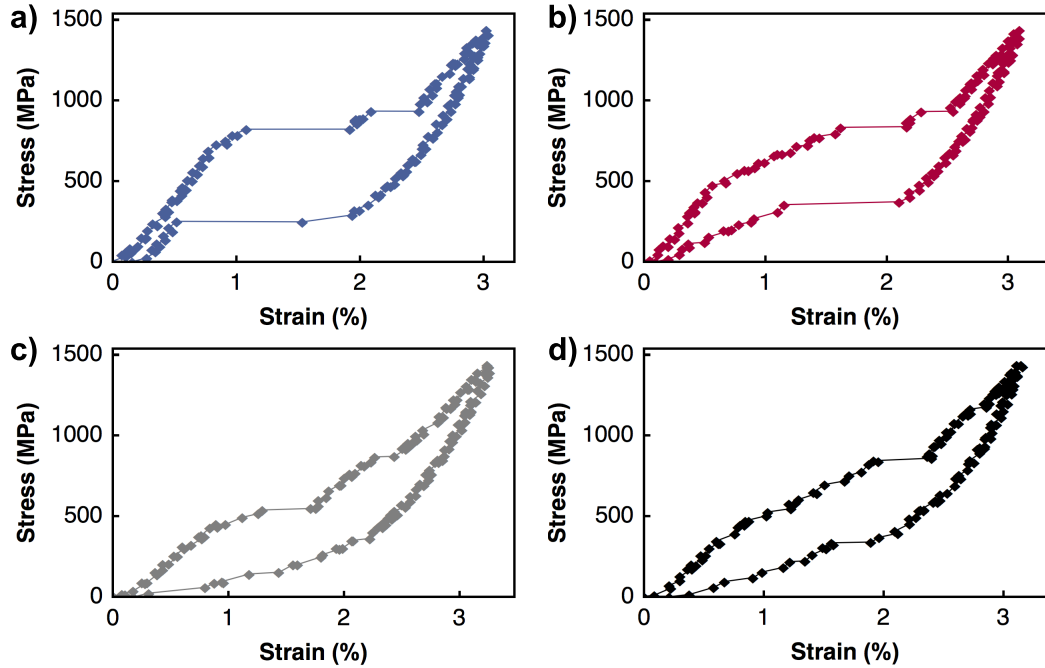


Figure 18: (a) First superelastic cycle of 15.9% CeO<sub>2</sub> zirconia micropillar (b) 10<sup>th</sup> cycle (c) 20<sup>th</sup> cycle (d) 27<sup>th</sup> cycle

## 2.8 ENERGY DISSIPATION OF SMALL-SCALE ZIRCONIA

Another useful property of superelastic materials is their ability to absorb and dissipate energy which is a direct result of the phase transformation. Energy is needed to drive the transformation, quantified by the enthalpy of transformation, but this is considered reversible as this energy is returned on the reverse transformation. As the transformation front moves through the material it may reach obstacles or defects such as grain boundaries, pores, precipitates, and free surfaces. The energy required to surpass these obstacles is generally not recovered and is therefore dissipated. The energy lost was measured from the hysteresis area inside the superelastic stress-strain curves. For example the superelastic curve shown in [Figure 18a](#) had a raw energy dissipated of 10.4 MJ/m<sup>3</sup>. When comparing energy dissipation values, the standard convention is to use the damping merit index which also takes into account the stiffness of material through its Young's modulus. The calculated merit index for zirconia micro-pillars ranged

from 1.2-2.5, which was nearly double of what was measured in Cu-Al-Ni micropillars [40].

## 2.9 THE SHAPE MEMORY EFFECT IN SMALL-SCALE ZIRCONIA

The small-scale zirconia micro-pillars were also investigated for their shape memory properties. To do this a slightly different doping composition was selected, namely 8 mol% CeO<sub>2</sub>-0.5 mol% Y<sub>2</sub>O<sub>3</sub>- ZrO<sub>2</sub>. Yttria is another doping element that will stabilize the low temperature phase but is a stronger stabilizer. Doping with 8 mol% CeO<sub>2</sub> should produce mostly monoclinic phase according to Table 5. The addition of a small amount of Y<sub>2</sub>O<sub>3</sub> will further stabilize and yield the tetragonal phase. This composition exists in a distinctive region in stress-temperature space where room temperature is in between the martensite start and austenite start temperatures, see Figure 19. This space is interesting because the material can begin in the austenite phase and then be stress induced into martensite but then upon unloading it will remain in the martensite phase. Heating can then return it back to the austenite phase. In essence this is a shape memory cycle except that the starting phase is austenite instead of the usual martensite.

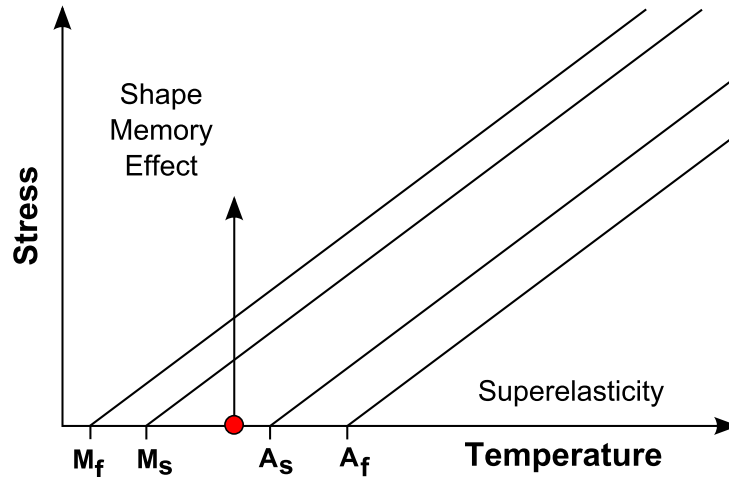


Figure 19: Stress-temperature diagram for a composition that demonstrates the shape memory effect while starting in the austenite phase.

To demonstrate the shape memory effect, a micro-pillar was loaded in bending mode — by loading it slightly off-axis — to a bending strain of ~7%, as shown

in [Figure 20a](#) and [Figure 20b](#). After bending, no visible cracks were seen and the large strain attained could only be attributed to the stress induced martensitic transformation since typical ceramics can only obtain 1-2% strain. To further prove the deformation was due to the transformation, the bent pillar was heated above the austenite transition temperature (500°C for 2 hours) to revert it back to the austenite phase. This caused a near complete shape recovery as seen in [Figure 20c](#).

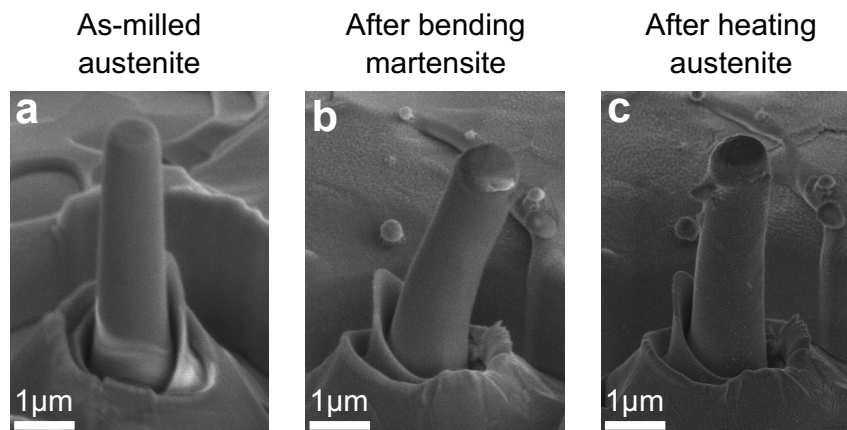


Figure 20: (a) As-milled pillar in austenite phase (b) pillar after bending load applied achieving 7% bending strain (c) pillar after heating to 500°C to recover original shape [33].

Yet another indicator of the phase transformation can be seen in a close-up image of the bent pillar, [Figure 21a](#), where a striped morphology was observed which is a classic characteristic of martensite [8]. The stripes are likely different variants of martensite that are required to accommodate the bending strain. When the pillar was heated, the martensite stripes disappeared when the martensite transformed to austenite and is shown in [Figure 21b](#).

One final characterization was done to verify the phase transformation in the shape memory micro-pillars. A pillar similar to the pillar shown in [Figure 20](#) was fabricated and was bent to induce the transformation. After bending, the pillar was prepared for TEM analysis using focused ion beam techniques to produce a thin section as shown in [Figure 22a](#). Selected area electron diffraction was carried out and the bent pillar was most closely indexed as the monoclinic phase, as shown in [Figure 22b](#). This same specimen was then heat treated at 500°C for two



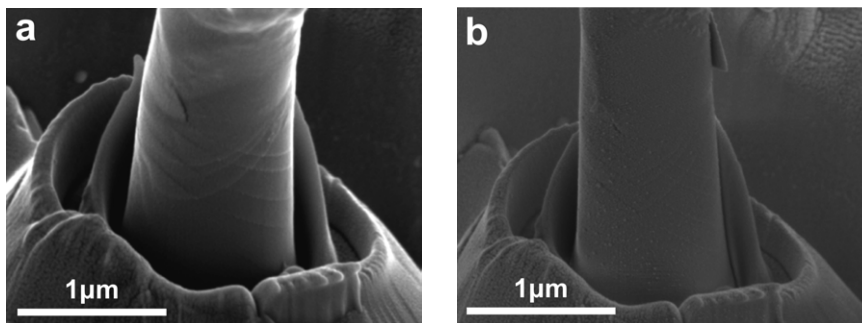


Figure 21: (a) Close up image of pillar after compression showing characteristic martensite stripes (b) pillar after heating no longer has visible martensite stripes [33].

hours (Figure 22c) followed by selected area electron diffraction phase indexing (Figure 22d) which showed after heating that the phase returned to the tetragonal phase providing conclusive evidence that the shape change was due to the phase transformation.

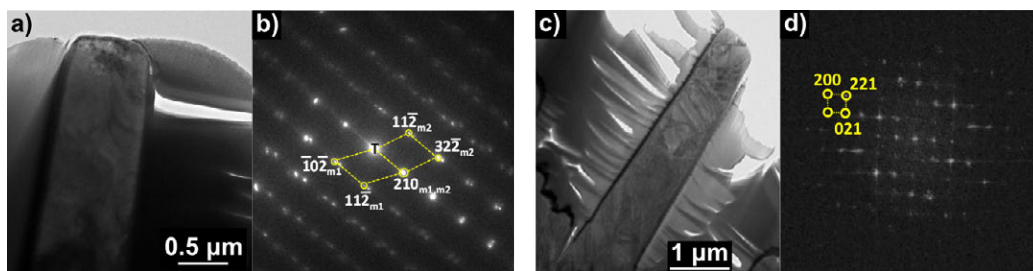


Figure 22: a) TEM lamella of a bent pillar and b) corresponding selected area diffraction pattern indexed as monoclinic. c) TEM lamella of a bent pillar after heating to 500°C and d) corresponding selected area diffraction pattern indexed as tetragonal [42].

## 2.10 COMPARISON OF CERAMIC AND METALLIC SHAPE MEMORY MATERIALS

The prospect of a new class of materials based on small-scale shape memory ceramics is technologically intriguing because ceramics offer a distinct suite of properties that differ from other shape memory materials. One of the most attractive properties of ceramics are their very high strengths and in the context of shape

memory materials the strength increase means that the stresses to induced superelasticity are much higher than other shape memory materials. This is best seen in [Figure 23](#) where the superelastic stress-strain curve for zirconia micro-pillars are compared to other shape memory metals, NiTi and Cu-Ni-Al. It is abundantly clear that zirconia requires larger stresses to induce the transformation,  $\sim 1.7$  GPa, compared to several hundred MPa in the metals.

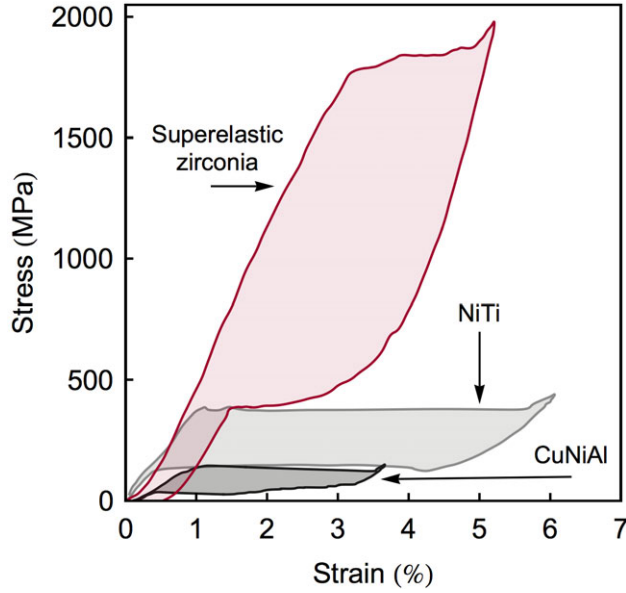


Figure 23: Superelastic stress-strain curves for zirconia micro-pillars and shape memory metals, Ni-Ti [43], and Cu-Ni-Al [40]. Superelastic zirconia has much higher transformation stresses due to the high strength of zirconia [33].

Another interesting feature of the stress-strain curve in [Figure 23](#) is the energy dissipated, as indicated by the area within each curve. To quantify energy dissipation, the loss factor ( $\eta$ ) is defined as,

$$\eta = \frac{\Delta W}{\pi \cdot W_{\max}} \quad (2)$$

where  $\Delta W$  is the total area within the curve and  $W_{\max}$  is the area under the curve up to the maximum. The loss factor normalizes the energy dissipation to the total energy input. To compare across different materials another normalization is required to account for the material's stiffness and the resulting damping merit index (MI) is given as,

$$MI = \eta \cdot E^{1/2} \quad (3)$$

where  $E$  is the Young's modulus of the material. The calculated merit index for the superelastic zirconia curve in [Figure 23](#) is  $\sim 2$  GPa which is almost double of that found in metals [40] making small scale shape memory ceramics appealing for energy damping applications.

The large stresses that are required to drive the transformation in shape memory ceramics are expected to translate into large output stresses when the shape memory effect is used for actuator applications. In [Figure 24](#), the actuation stress and strain are plotted for common actuator systems. The actuators can be divided into 2 groups.

- Multi-Component Actuator System

This group includes the actuators in the bottom right of [Figure 24](#) and they require the use of some type of secondary system; in order to provide motion hydraulics and pneumatics rely on pressurized fluids while solenoids and moving coil transducers need electromagnetic coils to provide the motion. This makes these systems large and bulky, but they can attain large combinations of stress and strain, as noted by the dashed contour lines of constant energy density.

- Solid-State Actuators

This group is comprised of piezoelectrics, magnetostrictives, and shape memory materials which all exploit naturally occurring phenomena based on the underlying solid-state physics of the material such as, bond stretching for piezoelectrics and magnetostrictives, or phase transformations for shape memory materials. The advantage of solid-state actuators is that they take up very little space and are good for micro-scale applications, but they typically suffer from low magnitudes of actuation strain; this is especially true for piezoelectrics.

[Figure 24](#) shows that shape memory ceramics have an excellent combination of actuation stress and strain, yielding an energy density approaching  $100 \text{ MJ/m}^3$ . This energy density exceeds not only shape memory metals but some of the multi-component actuator systems.

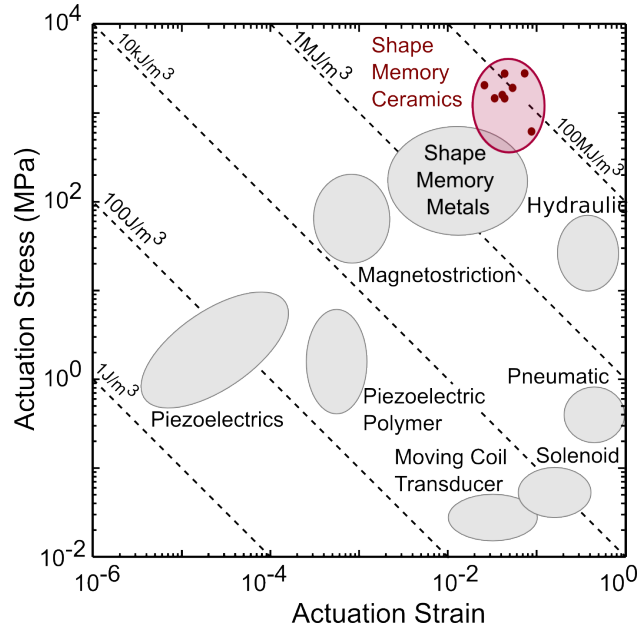


Figure 24: Comparison plot of actuation stress and strain for common actuator systems. The dashed lines represent contours of constant energy density. Figure adapted from Huber, Fleck, and Ashby [44].

Another property where ceramics are generally differentiated from metals is operating temperature, with ceramics being more refractory than metals. This explains their use as high temperature shape memory materials for applications in the aerospace or automotive fields [45]. The common shape memory metals like Ni-Ti and Cu-Al-Ni can't be used at temperatures much greater than  $\sim 150^{\circ}\text{C}$ , as shown in Figure 25. Their operating temperatures can be increased but usually with the addition of expensive platinum group metals. The high melting temperature of zirconia and the high transformation temperature to the tetragonal phase ( $\sim 1100^{\circ}\text{C}$ ) makes zirconia promising for high temperature applications. As noted previously, the transformation temperatures are controllable by doping with other metal oxides.

## 2.11 CONCLUSIONS

Until now investigations into the shape memory properties of shape memory zirconia have found that it does indeed demonstrate the expected mechanical

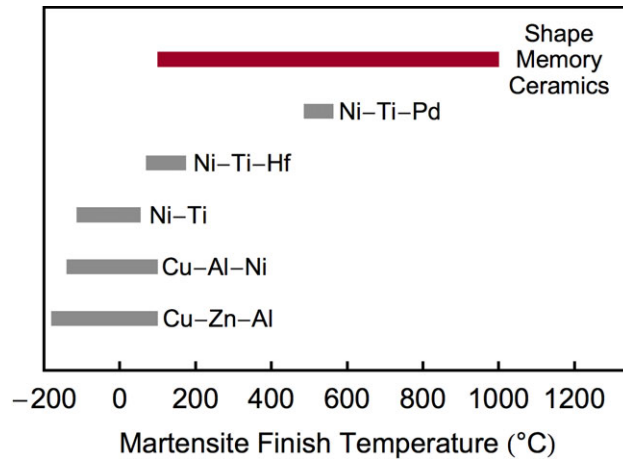


Figure 25: Comparison plot the martensite start temperature for various shape memory materials [33, 46].

properties such as the shape memory effect and superelasticity but due to their brittleness they fail at low strains after a few cycles and were therefore not considered useful for practical applications. Here we applied microstructure engineering techniques to produce small scale single crystal or oligocrystalline structures that eliminated internal stress concentrations and permitted the transformation to occur without fracturing the sample. This opens the door to robust shape memory ceramics that can take advantage of the large strains and stresses found in shape memory ceramics to eventually be used in practical applications. The next two chapters will delve deeper into the scientific understanding of small scale shape memory ceramics in order to investigate size effects and crystal orientation effects.



## OLIGOCRYSTALLINE TO POLYCRYSTALLINE TRANSITION

---

Materials properties can vary greatly when the specimen dimensions are reduced; this is especially well established in metals where the yield stress increases with power-law scaling as the sample size decreases [47]. This chapter first discusses the sample size effects that have been previously observed in shape memory metals and then explores new experimental work on size effects in shape memory ceramics.

*- This work done in collaboration with:  
Dr. Zehui Du and Xiaomei Zeng at Nanyang Technological University*

### 3.1 SIZE EFFECTS IN SHAPE MEMORY METALS

An exploration of size effects in micro-scale shape memory metals was done by San Juan et al. in 2009 by way of micropillar compression of a Cu-Al-Ni shape memory alloy [40]. The results showed that superelastic pillars with diameters of approximately 1  $\mu\text{m}$  had an exceptionally large damping ability as defined by the damping figure of merit (the damping figure of merit normalizes damping capacity with stiffness). This work was followed by a more comprehensive investigation into the size effects in shape memory metals by Chen et al. which revealed that size effects also existed for the transformation temperatures and the transformation stresses [11]. Chen sought to explain the mechanisms of the size effects and determined that the most important factors were the stored elastic energy, internal friction, and heat dissipation while the interfacial energy, surface energy, and mechanical wave propagation were of lesser importance. Several other studies were carried out to expand the research in copper based alloys [16, 41, 48] and magnetic shape memory alloys [49] but the overall conclusion was that shape memory materials in small sizes had potential to offer greater performance for a variety of metrics.

Another important aspect of size effect studies is the relationship between the sample size and the underlying microstructure. Much of the previous work investigated essentially perfect single crystals with varying sample diameters [40, 47] and for these samples there is no underlying microstructure. But it is possible to have small-scale structures that still have microstructure; or in other words, small samples with even smaller grains within the sample. This was investigated by Ueland et al. in copper based shape memory alloys microwires showing a transition from single crystal to oligocrystalline to polycrystalline [16] which was discussed in Section 1.5 and illustrated in Figure 5. The most important takeaway from this work was that oligocrystalline structures could have properties that approach that of single crystals but without the difficulty of making single crystals.

### 3.2 OLIGOCRYSTALLINE TRANSITION IN SHAPE MEMORY CERAMICS

The previous work presented in Chapter 2 showed that micron scale shape memory ceramics offered superior cycling ability compared to bulk specimens, however in that proof of concept work, the sample size was kept relatively constant and therefore size effects were not explored. Here we systematically investigated size effects by fabricating a series of micro-pillars with different diameters from a polycrystalline material with constant grain size. The resulting set of pillars spanned the oligocrystalline to polycrystalline transition providing an ideal testing ground to detect the change of properties as the microstructure shifted from oligocrystalline to polycrystalline.

Micro-pillars with diameters ranging from 0.5 to 3.0  $\mu\text{m}$  were machined from a bulk ceramic using focused ion beam milling. This diameter range was chosen to straddle the mean grain size of the bulk ceramic (1.7  $\mu\text{m}$ ) thus producing some pillars with a diameter significantly smaller than, and some larger than, the mean grain size. A total of 10 pillars were tested in micro-compression using a nanoindenter equipped with a 20  $\mu\text{m}$  nominal radius cono-spherical tip.

An example of an oligocrystalline pillar is shown in Figure 26a with the pillar having an effective diameter of 0.7  $\mu\text{m}$  which was much smaller than the bulk grain size so each grain was expected to span the entire diameter. Due to its height, 4.1  $\mu\text{m}$ , it was likely to contain more than one grain along its height, although this would not prevent it from having a bamboo like structure. A load of 0.5 mN

*Effective diameter accounts for pillar taper using the top and bottom diameters.  $d_{\text{eff}} = \sqrt{1/3(d_t^2 + d_t d_b + d_b^2)}$*



was applied to the pillar causing it to bend as shown in Figure 26d with the corresponding load-displacement curve in Figure 26g. The load-displacement curve shows two distinct displacement plateaus that are characteristic of the martensitic transformation. The presence of two plateaus could be due to either 1) multiple grains being present along the length of the pillars with each being activated at a different stress or 2) a stress gradient due to bending, with the outer surface transforming first because it experiences higher stress. After unloading there was substantial residual displacement consistent with the expected transformation. By analyzing the curvature of the bent pillar — by treating it as a cylindrical beam — the bending strain was calculated as  $\sim 7\%$ . The critical stress was calculated as 0.5 GPa by using the critical load ( $F_c$ ) shown on the load-displacement curve and the pillar dimensions.

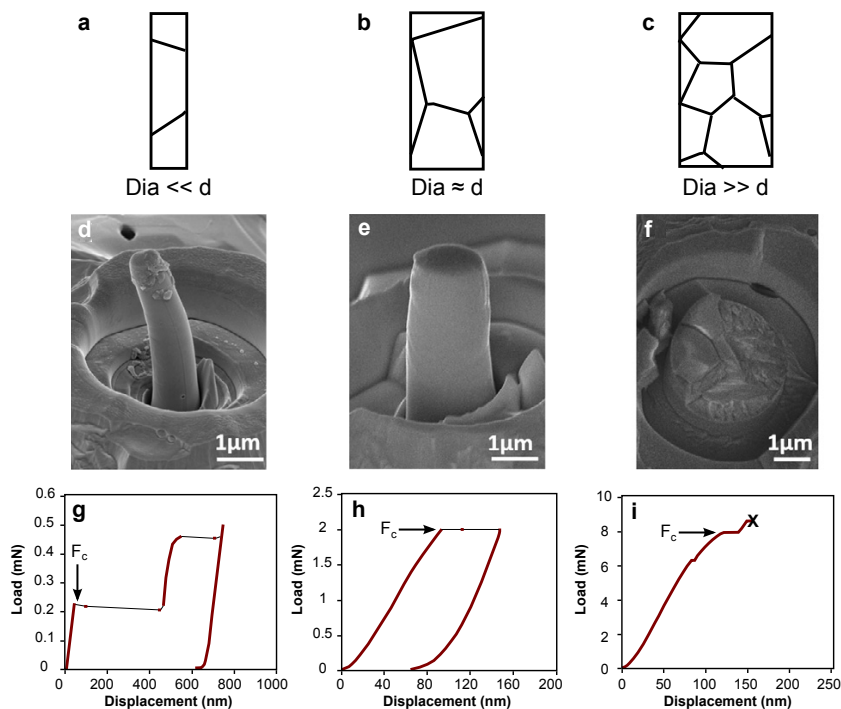


Figure 26: Pillar grain schematic, SEM micrograph and corresponding load-displacement curve respectively for an oligocrystalline pillar (A,D,G) a near oligocrystalline pillar (B,E,H), and a polycrystalline pillar (C,E,I) [42]. The bulk grain size was  $\sim 1.7 \mu\text{m}$ .

The bending strain in the oligocrystalline pillar was very large, 7%, yet there was no evidence of cracking. The pillar was examined from multiple angles as shown in the micrographs in Figure 27, with no observed cracks. However, close examination of the side of the pillar showed a striped pattern which is characteristic of martensitic domains intersecting with the free surface, which is clearly seen in Figure 28a.

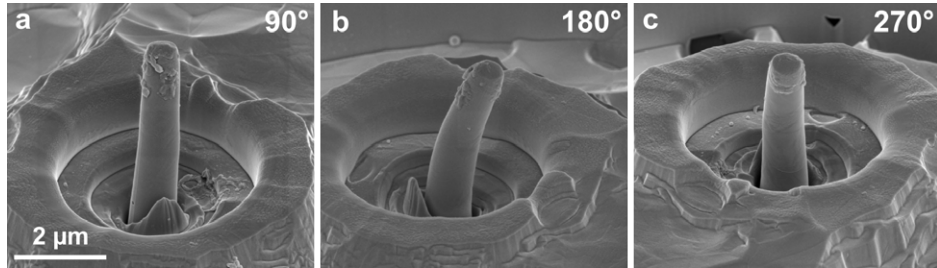


Figure 27: Close up micrographs of bent oligocrystalline pillar from different viewing angles a) 90° b) 180° c) 270°. No cracking is observed.

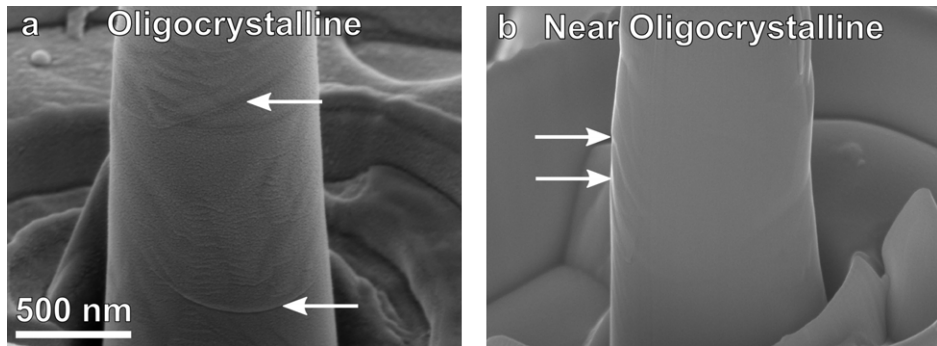


Figure 28: Observation of martensite stripe pattern on a) oligocrystalline pillar and b) near oligocrystalline pillar.

Another type of pillar was made with a diameter of 1.7 µm and height of 4.4 µm. Since the average bulk grain size was also 1.7 µm this pillar should have grains that just span the pillar diameter and will therefore likely contain 3-6 total grains. This pillar is referred to as near oligocrystalline because it will likely contain some triple junctions between grains. A schematic of the structure and an image of the pillar after compression are shown in Figure 26b and Figure 26e respectively. For compression testing, a 2 mN axial load was applied to the pillar with the load-displacement curve shown in Figure 26h. The load-displacement

### 3.3 TRANSFORMATION STRESS ACROSS THE OLIGOCRYSTALLINE TRANSITION

curve had one displacement plateau of 54 nm, indicative of a martensitic transformation. The residual displacement was measured as 58 nm which matched well with the displacement plateau. The critical stress, calculated from the critical load  $F_c$ , was found to be 0.9 GPa. Again a stripe pattern was observed on the side of the pillar, [Figure 28b](#), which likely reflects a martensite domain with a thickness of approximately 200 nm.

The last type of pillar examined was a polycrystalline pillar with grain size much smaller than the pillar diameter. An example pillar is shown in [Figure 26f](#) with diameter of 2.8  $\mu\text{m}$  and height of 5.4  $\mu\text{m}$ . A microstructure schematic of the pillar is presented in [Figure 26c](#) and it is expected to have many grains, grain boundaries, and triple junctions. The pillar was loaded axially with a force of 9 mN producing the load-displacement curve in [Figure 26i](#). A small strain plateau was observed around 8 mN but further loading resulted in fracture at 9 mN which corresponds to a stress of 1.4 GPa. We suspect that the martensitic transformation that occurred at 8 mN may have induced a crack that initiated the final fracture.

The three pillars presented in [Figure 26](#) — oligocrystalline, near oligocrystalline, and polycrystalline — are representative of all the pillars tested in this work. In total 10 pillars were fabricated, spanning the diameter range of 0.7-2.8  $\mu\text{m}$ , all with constant grain size. The most obvious trend was that as the pillar diameter increased they were more likely to fracture. This is attributed to the increased prominence of grain boundaries and triple junctions in these pillars, which are sites where stresses are concentrated due to mismatches between neighboring grains that transform at different times due to the difference in crystal orientation. However, when the pillar diameter was reduced, these mismatch stresses were eliminated and the samples could transform freely without fracture.

### 3.3 TRANSFORMATION STRESS ACROSS THE OLIGOCRYSTALLINE TRANSITION

The critical stress for transformation or the fracture stress was measured for each pillar to observe the effect size has on the stresses, with the data gathered in [Figure 29a](#). The general trend showed that as the pillar diameter decreased the stress to trigger the transformation decreased. When the pillar diameter was around 1  $\mu\text{m}$  the critical stress was  $\sim 0.6$  GPa and when the pillar diameter was

increased to 2.8  $\mu\text{m}$  the stress required rose to  $\sim 1.3$  GPa. This behavior is opposite to what is normally observed in shape memory metals, which tend to get stronger as they get smaller [11]. One explanation for this is the difference in the stiffness of ceramics versus metals; ceramics being much stiffer. That can make the stored elastic energy term more significant and this will be discussed in greater detail in Section 4.6. Pillars with diameters less than one micron (marked with a dotted oval in Figure 29a) tended to bend in response to the applied load but if the critical stress is considered as the inner-fiber uniaxial stresses then the overall trend is

Z. Du et al. / Scripta Materialia 101 (2015) 46–48

a striped pattern of  
s of approximately  
ry materials, indicat-

and height of 5.4  $\mu\text{m}$ .  
an the grain size of  
ave a polycrystalline  
boundaries, and triple  
ted schematically in  
s applied, producing  
Figure 2I. A small  
1.3 GPa), suggesting  
, but further loading  
which was verified by  
We believe that the  
induced a cracking

of many experiments  
a general trend that  
more grains are more  
ted to the increased  
ple junctions in such  
ormation mismatch  
nsform sequentially  
ue to their different  
diameter is smaller  
to sustain the trans-  
ormation mismatch is  
of grain junctions  
ss-relieving free sur-  
onstraints that lead  
smaller diameters we  
isitic transformation  
all 10 pillars tested  
s versus the effective

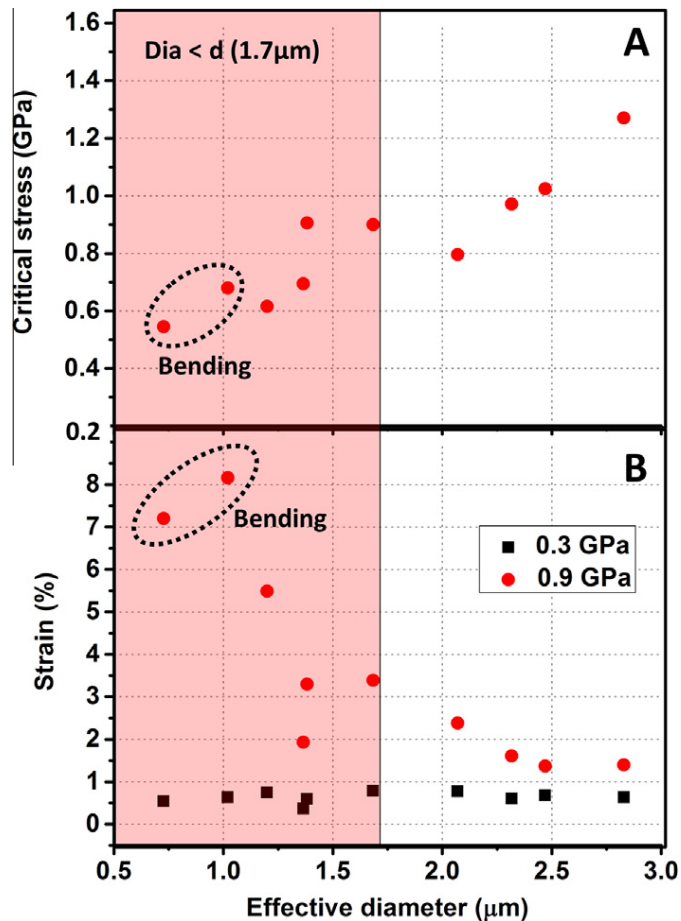


Figure 3. (A) Graph of critical stress for the (B) formation and b) achieved under a stress of 0.3 GPa (black square dots) and 0.9 GPa (red circle dots); this is a function of the effective pillar diameter ( $D_{\text{eff}}$ ). The figure indicates the grain size of the bulk ceramic from which the pillars were made. The red shaded area denotes the pillar diameters smaller than grain size. The data highlighted by the dotted ovals are from the bent pillars; the other data are for pillars loaded in compression. (For interpretation of the references to color in this figure legend, the reader is referred to the web version of this article.)

56

transformation, i.e., those with an effective diameter in the range of  $\sim 0.7$ – $1.7$   $\mu\text{m}$ . These oligocrystalline pillars

### 3.4 SIZE EFFECT ON TRANSFORMATION STRAIN

A summary of how the transformation strain varies with the pillar diameter is shown in [Figure 29b](#). Again, since the pillars with diameters less than  $\sim 1 \mu\text{m}$  were bent, their inner-fiber uniaxial strain was used to allow some degree of cross-comparability with liberal error bars applied to the strain values. Two measures of strain were taken. The first at low stress (0.3 GPa) which should lie in the elastic regime and here all the pillars exhibited similar strains of  $\sim 0.5\text{-}0.7\%$ . The second strain measurement was taken at high stress (0.9 GPa) where the martensitic transformation was triggered for most of the pillars. The smaller pillars — those with effective diameters between  $0.7\text{-}1.7 \mu\text{m}$  — were able to survive the transformation without cracking or fracture. Furthermore, significant strains were obtained for these pillars varying from 3% up to 8%. On the other hand, the larger, polycrystalline pillars with diameters greater than  $2 \mu\text{m}$  tended to crack and fracture before (or as a result of) the transformation and therefore had much smaller strains than the oligocrystalline pillars.

### 3.5 CONCLUSIONS

The results presented in this chapter provide quantitative insight into the transition from polycrystalline shape memory ceramics that have tendencies to crack to oligocrystalline shape memory ceramics that can sustain transformation without cracking. The most important structural feature is the relationship between the characteristic size, in this case the pillar diameter, and the grain size. In this work, pillars with diameters larger than  $\sim 2 \mu\text{m}$  were considered polycrystalline and tended to fracture and exhibited small strains. However, when the pillar diameter was on the order of the grain size the structure was classified as oligocrystalline and here the grains were largely unconstrained and as a result the stress needed to induce the martensitic transformation was decreased. In addition the resulting transformation strain tended to increase as the pillar diameter was decreased and reached values between 3-8%, a large value for a ceramic material. It should be noted however that as pillars become more oligocrystalline fewer total grains were present and the stress and strain values became more sensitive to the actual crystal orientation of each grain. For these types of structures a greater

spread is expected in the measured stress and strain, and this will be explored further in the next chapter.

## ORIENTATION EFFECTS

---

Up to this point the improved properties of small volume zirconia based ceramics — transformation without cracking, superelastic cycling ability, damping capacity etc. — have been demonstrated on single crystal specimens or oligocrystalline specimens. When considering these types of samples, the properties are expected to strongly depend on the specific crystal orientation that is present, more so than in polycrystalline specimens, which can be assumed to have isotropic properties due the large number of crystals present. However, the crystal orientation dependence on the shape memory properties of small-scale zirconia is still mostly unknown, and in this section the crystallographic theory will be introduced and compared with experimental data on single crystals of various orientations.

*- This work done in collaboration with:  
Xiaomei Zeng at Nanyang Technological University*

### 4.1 CRYSTAL ORIENTATION DEPENDENCE IN SHAPE MEMORY METALS

The effect of crystal orientation has been studied in some shape memory metal alloys, such as Ni-Ti [50] and Cu-Al-Ni alloys [2], and the results have shown that both the transformation stress and strain have an unmistakable dependence on the crystal orientation as illustrated by Figure 30, showing superelastic stress-strain curves for various orientations of a Cu-Al-Ni alloy [2]. The transformation stress and strain vary widely depending on the crystal orientation. The reason for the orientation dependence is related to the mechanism of the transformation which occurs by shearing of specific crystal planes and it is this relationship between the shear planes and the applied stress that gives rise to variations in properties with orientation. In other words, for a given orientation only certain crystallographic shears are possible because of their position with respect to the applied stress. The same mechanisms are expected to be present in shape memory ceramics and will be expanded upon in the following sections.

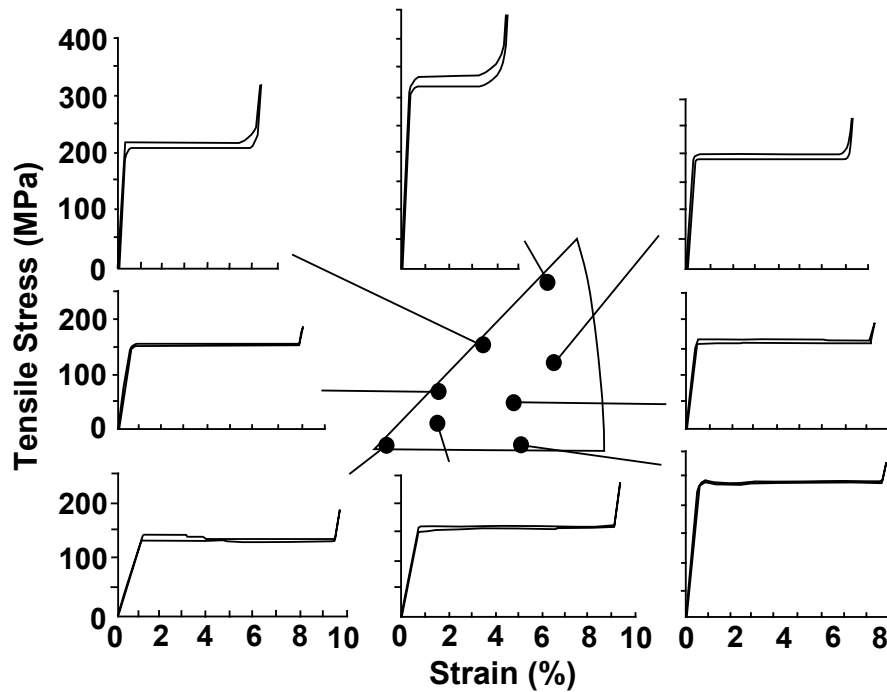


Figure 30: Orientation dependence of the transformation stresses and strains in Cu-Al-Ni alloys [2].

#### 4.2 EXPERIMENTAL DESIGN FOR ORIENTATION DEPENDENCE

To explore the effects of crystal orientation it is necessary to assemble a variety of samples with different orientations. Often this is done by producing bulk single crystals that are rotated into the desired orientation and then machined into the proper geometry. However, this is challenging for ceramics because it is difficult to make ceramic single crystals. To overcome this, a bulk polycrystalline ceramic was used as the starting material, with large grains,  $\sim 5\text{-}10\ \mu\text{m}$  as shown in [Figure 31a](#). The orientation of each grain was measured using electron backscattered diffraction (EBSD). This produced a grain orientation map, [Figure 31b](#), where each grain's orientation was uniquely identified. Once the grain orientation was known micro pillars were milled from the grain. Finally, micro-compression tests were carried out as described in [Section 2.5](#) and [Section 2.6](#).

The bulk ceramic material that was used as the source of large grains was chosen with a very specific composition that began in the austenite (tetragonal) phase,



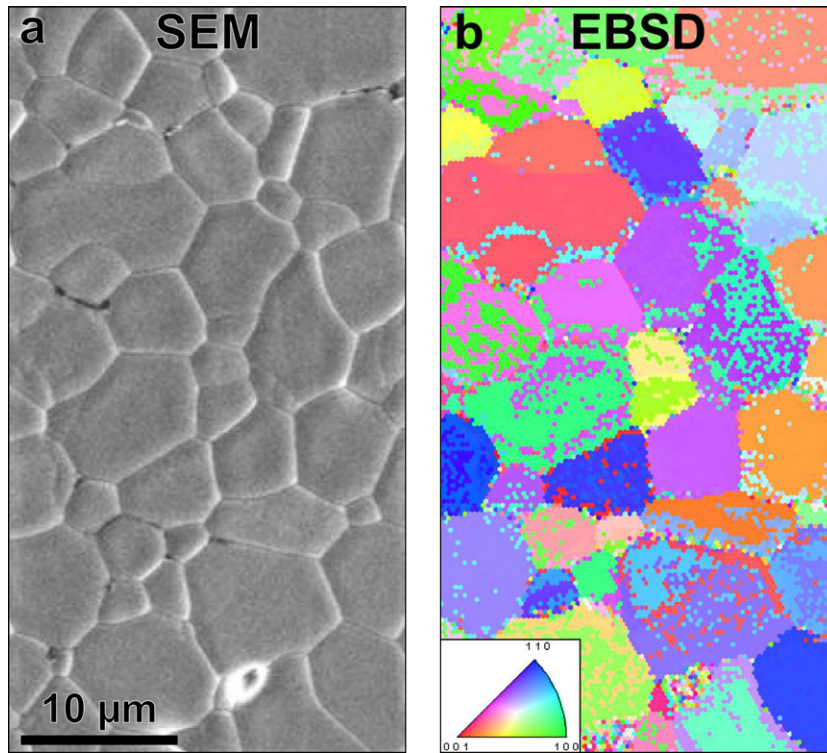


Figure 31: A polycrystalline zirconia micrograph, (a) SEM micrograph showing grain size and (b) EBSD grain orientation map [51].

but upon application of a load was expected to undergo a stress induced transformation to martensite at room temperature. Furthermore, it was expected to retain the martensite phase in an equilibrium condition after transforming because the composition was tuned so that the  $A_s$  and  $M_s$  temperatures spanned room temperature.

The transformation temperatures were measured with differential scanning calorimetry for a variety of yttria levels in 5 mol%  $\text{TiO}_2\text{—ZrO}_2$ , as shown in Figure 32, with the inset showing an example DSC curve. The trend clearly indicates that increased yttria lowers the transformation temperatures as expected from other literature [29]. Direct measurement of the room temperature phases using x-ray diffraction, Figure 33, shows that low levels of yttria doping (<2 mol%) result in the predominance of the monoclinic phase, yet higher doping (>2 mol%) mostly yields the tetragonal phase.

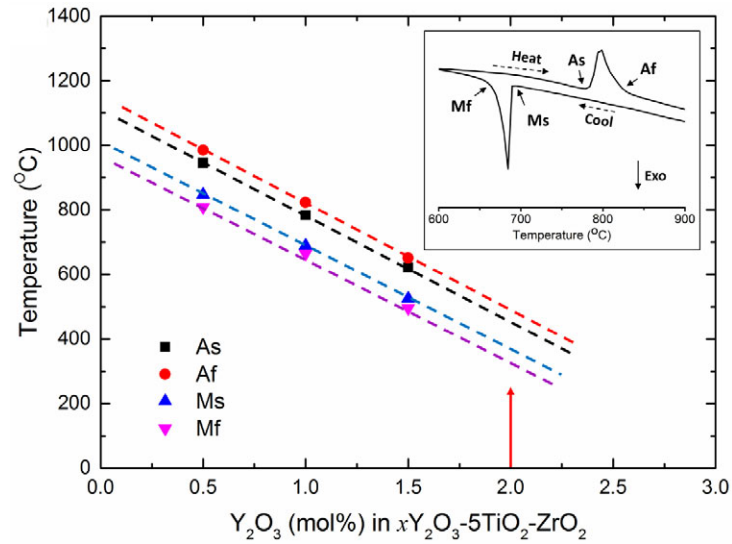


Figure 32: Transition temperatures ( $A_s$ ,  $A_f$ ,  $M_s$ ,  $M_f$ ) as a function of yttria doping in 5 mol%  $\text{TiO}_2\text{—ZrO}_2$ . Inset shows an example DSC curve for 2 mol%  $\text{Y}_2\text{O}_2\text{—5 mol% TiO}_2\text{—ZrO}_2$  [51].

In all, 43 grains were identified using EBSD, milled into pillars with a focused ion beam, and compressed using a nanoindenter to collect a complete picture of orientation space. The pillar diameters were kept close to 1.2  $\mu\text{m}$  to avoid the size effects discussed in the previous chapter. The pillar dimensions and crystal orientation data are all gathered in Table 6, Table 7, and Table 8, and their orientations are shown graphically in the standard tetragonal stereographic projection in Figure 35, which indicates which crystal plane normals are parallel with the compression axis. A wide variety of mechanical responses were observed, but the most common behavior was permanent transformation as illustrated in the before and after compression images in Figure 34a and Figure 34b. The corresponding load displacement curve is shown in Figure 34c and this was typical of all the transformed pillars and the figure also indicates the critical load to initiate the transformation, as well as the loading modulus, and transformation strain.

For all of the pillars studied here, it was clear that only a partial transformation occurred, as revealed by the surface morphology after transformation, as in Figure 34b. In this pillar and all the others studied, constraints at the top and bottom of the pillar apparently suppressed the shape change near those regions, and in some pillars there was incomplete transformation within other regions in the pil-

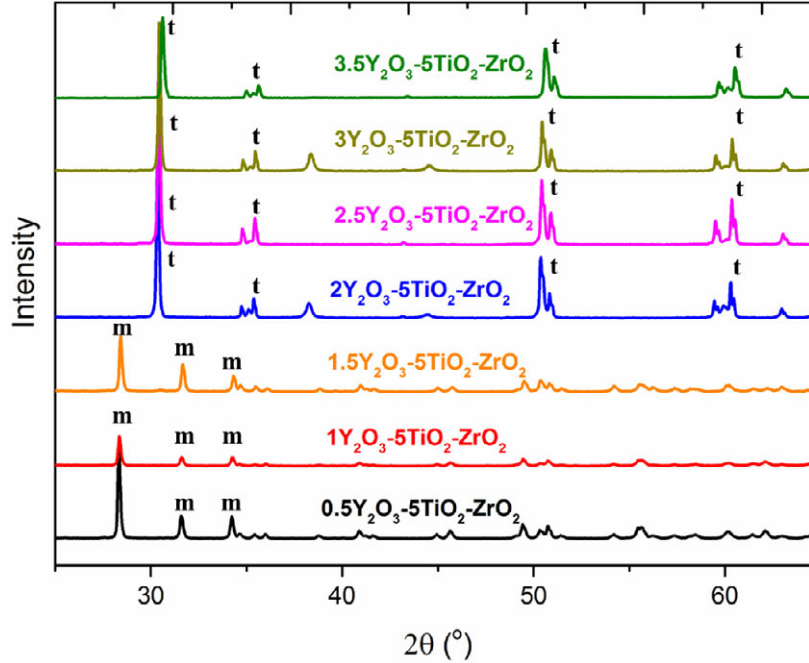


Figure 33: X-ray diffraction patterns as a function of yttria doping in 5 mol%  $\text{TiO}_2\text{—ZrO}_2$  [51].

lar midsection as well. Such partial transformation is important when carrying out strain calculations (as will be described later), and to account for this, each pillar was examined via SEM after compression to evaluate the fraction transformed ( $f_{\text{trans}}$ ) using a linear intercept method along the pillar axis as shown in Figure 34b. Some pillars had clear demarcations between the phases while others showed less distinct markings, leading to uncertainty in the determination of transformation percentage and by extension the measured strains.

In addition to transforming, some pillars fractured while other pillars showed signs of plastic slip. A summary of the different pillar behaviors, with select micrographs after compression and load-displacement curves, is presented in Figure 36. It is proposed that all of the different behaviors can be directly attributed to the variations in crystal orientation. For each pillar the following data were measured: 1) the critical stress to initiate the transformation, 2) the transformation strain, and 3) the loading elastic modulus. These data are all collected in Table 9, Table 10, and Table 11, and each property will be discussed in turn in the subsequent sections.

Table 6: Orientation and dimensions of TRANSFORMED pillars 1-24.

PILLAR	Pillar		Orientation		
	Dimensions ( $\mu\text{m}$ )		Euler Angles ( $^{\circ}$ )		
ID	EFFECTIVE DIAMETER	HEIGHT	E1	E2	E3
1	1.24	4.6	285	45	319
2	1.23	3.9	177	92	18
3	1.18	3.5	3	146	306
4	1.18	3.3	194	46	235
5	1.17	3.5	84	142	118
6	1.19	3.4	183	162	172
7	1.17	3.4	53	122	299
8	1.17	3.3	75	117	301
9	1.17	3.2	250	34	206
10	1.17	3.2	258	60	147
11	1.17	3.8	245	33	197
12	1.18	3.3	135	113	0
13	1.17	3.4	300	59	352
14	1.17	3.5	99	117	351
15	1.18	3.6	265	63	16
16	1.18	3.4	262	45	179
17	1.17	3.7	97	118	359
18	1.17	3.6	68	104	305
19	1.18	3.8	187	57	234
20	1.09	3.2	187	107	176
21	1.2	3.7	310	80	167
22	1.09	3.3	80	115	174
23	1.12	2.5	180	111	175
24	1.1	3.3	248	72	171

Table 7: Orientation and dimensions of TRANSFORMED pillars 25-31.

PILLAR	Pillar		Orientation		
	Dimensions ( $\mu\text{m}$ )		Euler Angles ( $^\circ$ )		
ID	EFFECTIVE DIAMETER	HEIGHT	E1	E2	E3
25	1.12	3.1	236	82	200
26	1.15	2.9	32	75	340
27	1.17	3.4	178	83	356
28	1.14	2.6	30	108	288
29	1.17	2.5	195	107	192
30	1.15	2.8	217	79	16
31	1.15	3.0	68	90	301

Table 8: Orientation and dimensions of FRACTURED pillars 32-40 and SLIPPED pillars 41-43.

PILLAR	Pillar		Orientation		
	Dimensions ( $\mu\text{m}$ )		Euler Angles ( $^\circ$ )		
ID	EFFECTIVE DIAMETER	HEIGHT	E1	E2	E3
32	1.2	3.7	232	15	296
33	1.16	2.7	72	101	357
34	1.19	3.6	243	72	53
35	1.17	3.6	105	98	384
36	1.14	3.6	157	9	185
37	1.12	3.5	185	17	184
38	1.19	3.7	91	104	353
39	1.17	3.3	178	88	349
40	1.14	2.4	200	90	177
41	1.11	2.5	15	85	320
42	1.15	2.5	8	94	126
43	1.08	2.3	163	88	224

Table 9: Mechanical properties of TRANSFORMED pillars 1-24.

PILLAR ID	TRANS %	Critical Stress (GPa)	Transformation Strain (%)	Loading Modulus (GPa)	
		MEASURED	MEASURED	MEAS.	THEORY
1	87	0.65	3.0	59	168
2	70	2.32	3.3	137	287
3	75	1.20	3.6	70	176
4	65	0.81	3.9	52	169
5	100	1.04	4.3	77	172
6	47	2.60	1.5	103	212
7	68	0.81	4.3	67	165
8	49	1.30	3.0	88	193
9	51	1.24	4.6	76	175
10	86	1.11	3.7	69	188
11	50	0.71	4.6	67	176
12	84	0.71	6.2	79	172
13	76	0.63	6.5	72	170
14	76	0.78	5.5	69	198
15	74	0.83	5.5	68	202
16	79	0.58	6.3	61	170
17	30	0.67	2.2	70	198
18	49	0.62	1.8	56	214
19	70	0.78	4.8	80	185
20	63	2.59	2.0	191	235
21	83	3.53	2.1	209	192
22	69	1.43	1.3	139	204
23	96	2.61	4.7	160	225
24	82	2.81	3.7	198	206

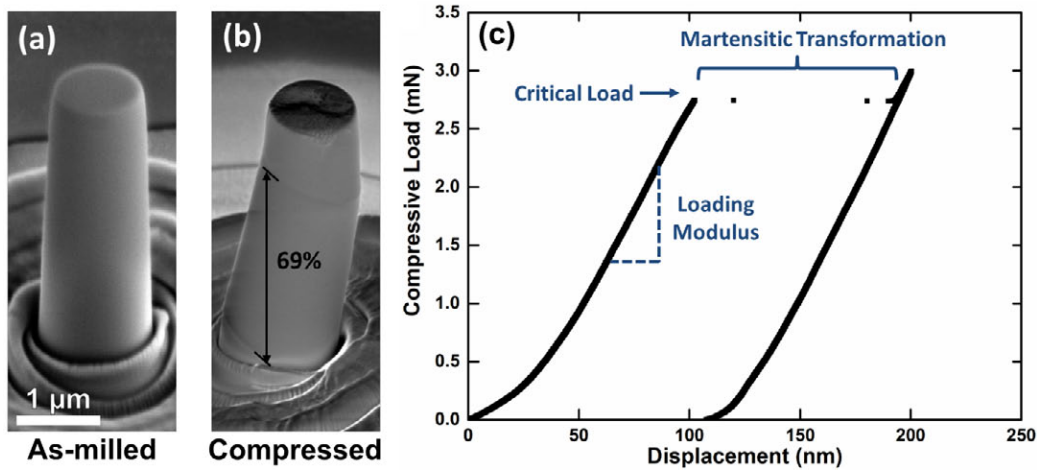


Figure 34: (a) An as-milled pillar and (b) the same pillar after compression with a clear transformed zone. The percent transformed was determined via a linear intercept method as shown. (c) A typical load-displacement curve for a transformed pillar showing a characteristic displacement plateau that is indicative of the transformation [51].

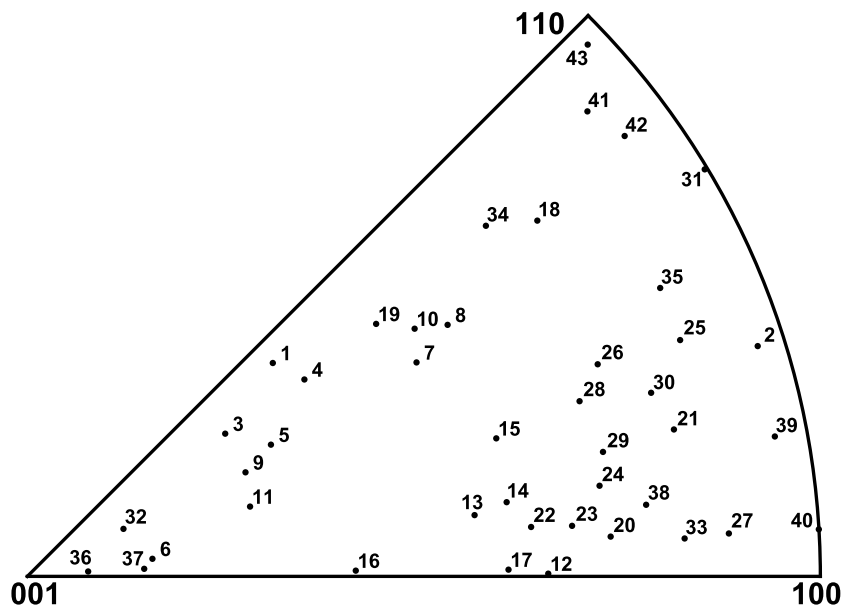


Figure 35: Tetragonal 001 inverse pole figure showing the orientations of all the pillars tested in this work.

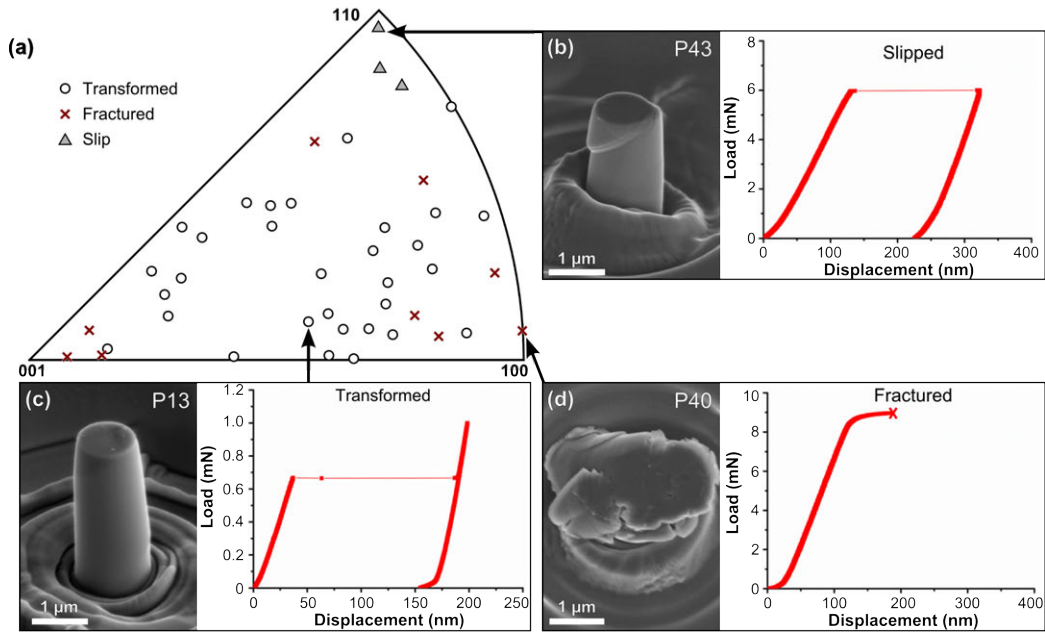


Figure 36: (a) Tetragonal inverse pole figure showing the various mechanical responses, (b) some pillars showed plastic slip, (c) most pillars transformed without cracking, (d) while some pillars fractured completely [51].

Table 10: Mechanical properties of TRANSFORMED pillars 25-31.

PILLAR ID	TRANS %	Critical Stress	Transformation	Loading	
		(GPa)	Strain (%)	Modulus (GPa)	
		MEASURED	MEASURED	MEAS.	THEORY
25	42	3.98	1.4	204	201
26	55	3.49	2.0	163	194
27	33	3.79	2.2	265	278
28	22	2.13	2.1	174	192
29	71	2.64	2.6	127	223
30	54	3.58	3.0	170	193
31	69	4.33	5.7	177	235



Table 11: Mechanical properties of FRACTURED pillars 32-40 and SLIPPED pillars 41-43.

PILLAR	TRANS	Critical Stress	Transformation	Loading	
		(GPa)	Strain (%)	Modulus (GPa)	
ID	%	MEASURED	MEASURED	MEAS.	THEORY
32	/	2.46	/	75	219
33	/	3.18	/	145	235
34	/	3.57	/	78	196
35	/	2.76	/	130	249
36	/	3.10	/	156	236
37	/	2.29	/	124	215
38	/	3.61	/	132	254
39	/	5.92	/	309	287
40	/	8.73	/	338	240
41	/	5.77	/	150	255
42	/	5.20	/	134	277
43	/	6.57	/	159	250

## 4.3 ORIENTATION EFFECT ON ELASTIC LOADING MODULUS

The anisotropy of the elastic modulus is well understood and theoretically expected values along the pillar z-axis can be calculated from the compliance tensor of tetragonal zirconia and the measured pillar orientation information. This is accomplished by rotating the standard compliance tensor into the specified lab frame, written using the full Einstein tensorial notation as [52],

$$\begin{aligned} \frac{1}{E_{33}} = s'_{33} = s'_{3333} = a_{3m}a_{3n}a_{3o}a_{3p}s_{mnop} = \\ (a_{31}^4 - a_{32}^4)s_{11} + (2a_{31}^2a_{32}^2)s_{12} + (2a_{31}^2a_{33}^2 + 2a_{32}^2a_{33}^2)s_{13} + \\ (a_{33}^4)s_{33} + (a_{32}^2a_{33}^2 + a_{31}^2a_{33}^2)s_{44} + (a_{31}^2a_{32}^2)s_{66} \end{aligned} \quad (4)$$

where the  $a_{ij}$  terms represent the components of the rotation matrix found from the EBSD orientation data in Table 6 - Table 8, and  $s_{11}$ ,  $s_{33}$ ,  $s_{44}$ ,  $s_{66}$ ,  $s_{12}$ , and  $s_{13}$  are the compliances for tetragonal zirconia taken from Kisi [53].

To measure the loading moduli of the pillars, the slope of the linear elastic section of the load-displacement curves was examined — the load-displacement data were converted to stress-strain data using the pillar effective diameter and height. The moduli data are collected in the fifth column of Table 9 - Table 11. In Figure 37, the experimentally measured moduli are plotted against the theoretical values calculated from Equation 4 and a reasonable correlation is shown, though there is better quantitative agreement at higher moduli. The experimental variation is attributed to several aspects of the micro-compression testing such as substrate and tip compliance, minor misalignments, and indentation compliance at the point of contact of the tip and pillar; these are all well known deficiencies of microcompression testing and the apparently high compliance seen here is in line with results from the field on other materials [37, 54].

Another way to view the orientation dependence of the loading modulus is by plotting the data in the standard stereographic triangle for tetragonal zirconia as shown in Figure 38. The color contour lines represent the theoretical moduli, which are highly anisotropic and range from 160 GPa near (111) to 290 GPa near (100). The measured data are superimposed over the theoretical contours and in general the experimental results follow the correct trend, with orientations near

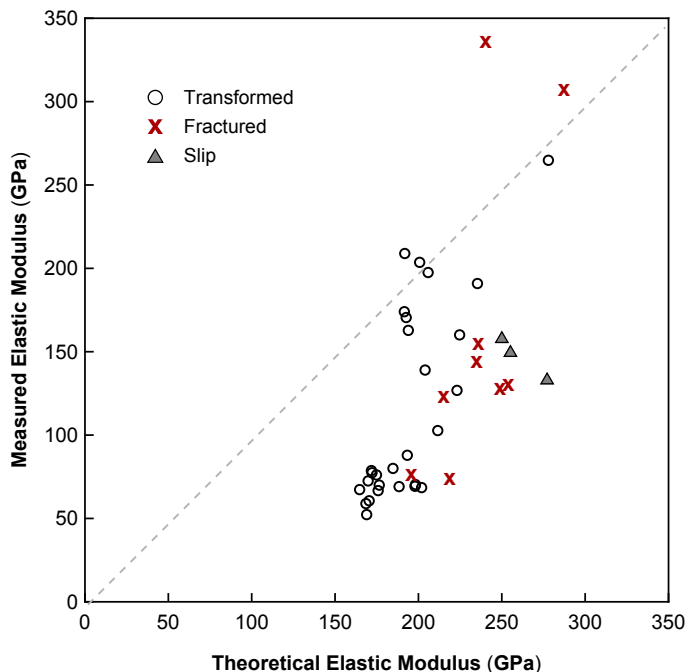


Figure 37: Comparison of theoretically expected pillar loading modulus and the measured modulus for all pillars — transformed, fractured, and slipped.

(111) having smaller moduli, typically less than 100 GPa, whereas orientations near (001) and (100) have higher moduli, mostly greater than 100 GPa.

Since the compression tests trigger a transformation from the tetragonal phase to the monoclinic phase, it should be possible to examine the unloading elastic modulus, which should correspond to the monoclinic modulus. However, most pillars did not fully transform to the monoclinic phase and a partial transformation would result in both phases being present during unloading and therefore the measured unloading modulus data would reflect the mixed properties of both phases. Due to this combined unloading behavior, the unloading modulus was not analyzed here.

#### 4.4 TRANSFORMATION CORRESPONDENCES AND THERMODYNAMICS

The transformation in zirconia is described by the lattice correspondence between the tetragonal (double) unit cell and the resulting monoclinic unit cell [20, 55], which were described previously in Figure 7. There are three possible routes

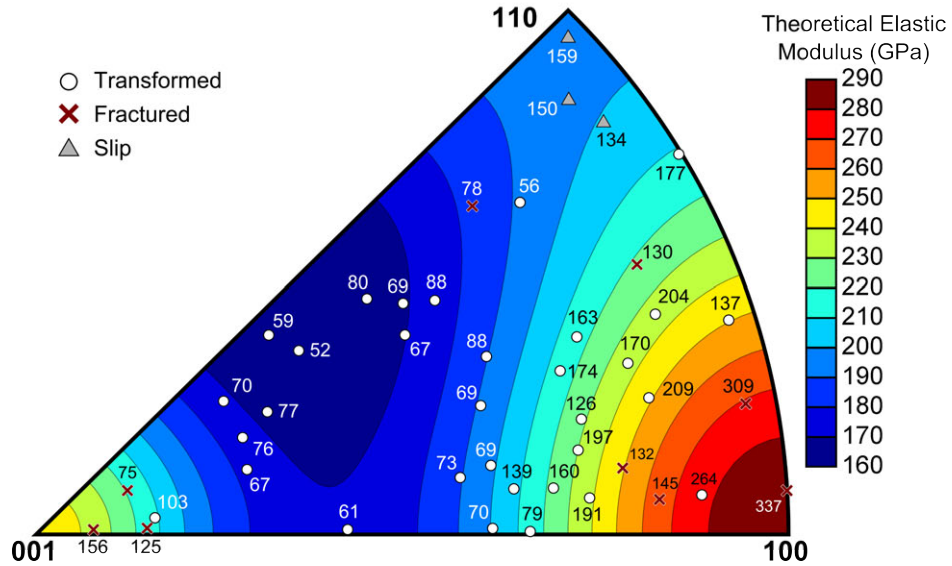


Figure 38: Standard stereographic projection comparing the theoretically expected pillar loading modulus (contour lines) and the measured modulus (data points) for all pillars — transformed, fractured, and slipped.

through which the tetragonal cell can become the monoclinic cell, and while each route produces an identical final monoclinic cell, the routes differ on whether the tetragonal  $c$  axis becomes the monoclinic  $a$ ,  $b$  or  $c$  axis [55, 56]. The three different monoclinic correspondences are shown in Figure 39. Here, the mathematical formalism from Simha [56] was used, but the correspondence notation of  $A$ ,  $B$ , and  $C$  was taken from Kriven [57]. For each correspondence there are four possible variants that can occur depending on the shear direction, which leads to 12 possible routes through which the transformation can occur. However, here we exclude any variant from correspondence  $A$  since it is not favored thermodynamically because it has larger principal distortions than correspondence  $B$ . The principal distortions are the sum of the squares of the eigenvalues of the Bain strain and this value is often taken as a measure of the strain energy [57]. Furthermore, correspondence  $A$  is not observed experimentally in literature [22], leaving only correspondence  $B$  and  $C$  to consider — and their 8 remaining possible variants. The preference among correspondence  $B$  and  $C$  will be discussed in greater detail in the following section.

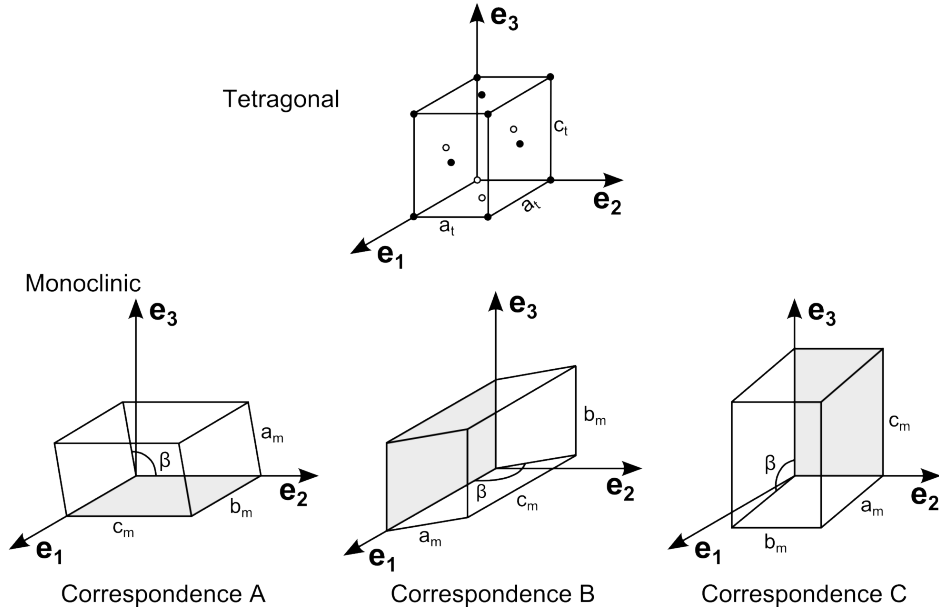


Figure 39: The tetragonal unit cell and the three different monoclinic correspondences, using A, B, and C notation from Kriven [57] with figure adapted from Simha [56]. Shaded planes are only to aid the eye.

The thermodynamics of the transformation from austenite to martensite can be examined by looking at the Gibbs free energy,  $\Delta G_{\text{Total}}$ , and can be written as [11, 58, 59],

$$\Delta G_{\text{Total}} = \Delta G_{\text{Chemical}} + \Delta G_{\text{Elastic}} + \Delta G_{\text{Friction}} - \sigma_{\text{shear}} \epsilon_{\text{shear}} \quad (5)$$

where all of the  $\Delta G$  terms on the right hand side represent various energies that must be overcome for the transformation to occur. The dominant free energy term is the chemical free energy,  $\Delta G_{\text{Chemical}}$ , which is a function of the enthalpy of transformation  $\Delta H$  and the temperature  $T$  and is expressed as [2],

$$\Delta G_{\text{Chemical}} = \frac{\Delta H \rho}{M} \left( 1 - \frac{T}{T_0} \right) \quad (6)$$

where  $\rho$  is the density,  $M$  is the molar mass, and  $T_0$  is the equilibrium transformation temperature between austenite and martensite. The elastic free energy,  $\Delta G_{\text{Elastic}}$ , represents the elastic energy that is stored in the bulk around the transformed region. In general for micro-pillars this term is very small because there is less bulk material around the transformed zone to store elastic energy and mis-

match strains are accommodated at free surfaces. The frictional term,  $\Delta G_{\text{Friction}}$ , includes any energy that is dissipated by the transformation front as it overcomes obstacles such as defects and free surfaces. Other terms can be added to the total Gibbs free energy including interfacial and surface energies, but these terms are typically negligible compared to the chemical, elastic, and frictional terms [11]. The final term in Equation 5 ( $\sigma_{\text{shear}}\epsilon_{\text{shear}}$ ) represents the energy that is supplied as external work by the applied stress and it is this term that opposes all the free energy terms. For the transformation to occur, the applied mechanical work must equal the sum of the  $\Delta G$  terms on the right hand side therefore bringing  $\Delta G_{\text{Total}}$  equal to zero. The next section will discuss the details of the mechanical work and how it relates to the measured transformation stress.

#### 4.5 ORIENTATION EFFECT ON TRANSFORMATION STRESS

The phase transformation from austenite to martensite in zirconia is shear dominated — as is the case for most shape memory materials — therefore an analysis based on shear stresses is sensible. The applied axial stress ( $\sigma_{\text{app}}$ ) can be related to the shear stress needed to drive the transformation ( $\sigma_{\text{shear}}$ ) by using the well known Schmid Factor (SF) [60],

$$\sigma_{\text{app}} = \frac{\sigma_{\text{shear}}}{\cos(\chi)\cos(\lambda)} = \frac{\sigma_{\text{shear}}}{\text{SF}} \quad (7)$$

where  $\chi$  is the angle between the shear plane normal and the compression axis and  $\lambda$  is the angle between the shear direction and the compression axis. Equation 7 predicts an inverse relationship between the Schmid factor and the measured transformation stress. The tetragonal unit cell faces are the viable shear planes, as shown in Figure 39, and their plane normals effectively have the indices matching the plane indices since the tetragonal double cell has only a slight degree of tetragonality of 1.7% ( $c/a = 1.017$ ) and the axes are therefore nearly Euclidean. Since only one variant of the 8 possible variants can occur, a variant selection process is needed to determine which of the variants is preferred. The most common selection criterion is the maximum resolved shear stress criterion [61]. This examines the transformation shear planes of each variant and finds the resolved shear stress for each, and then selects the variant with the maximum resolved shear stress acting on it. According to Equation 7, this selection criterion

will choose the variant with the most negative Schmid factor ( $SF_{max}$ ) since this variant will require the smallest applied compressive axial stress to reach the critical condition for transformation. The general idea here is that only one variant will have the largest shear stress acting upon it so it will have the largest driving force to transform. If we now combine Equation 5 - Equation 7 we can make a relationship between the applied stress and the Schmid factor as,

$$\sigma_{app} = \frac{\frac{\Delta H_p}{M} \left(1 - \frac{T}{T_0}\right) + \Delta G_{Elastic} + \Delta G_{Friction}}{SF_{max} \epsilon_{shear}} \quad (8)$$

which allows prediction of the required applied stress as a function of the thermodynamic variables and the orientation as represented by the Schmid factor.

The experimental micro-compression tests exhibited a wide range of critical stresses at which the transformation occurred, ranging from 0.58 to 8.7 GPa, suggesting that the critical stress depends strongly on the crystal orientation. This notion is well studied in shape memory metals [2, 60] but has yet to be explored in-depth in a ceramic shape memory material. In Figure 40 the orientation is shown using the standard stereographic triangle with colored contour lines representing the maximum Schmid factor, calculated from Equation 7, for a given correspondence with the experimentally determined transformation stresses overlaid on top as data points. For the purpose of discussion, the plots are duplicated to individually explore lattice correspondence B and C (Figure 40a and Figure 40b respectively) and correspondence B and C together Figure 40c.

In Figure 40 the dark blue regions represent high Schmid factor orientations, indicating that the transformation should be easiest and the applied critical transformation stresses low. Conversely, the low Schmid factor regions are designated as red, and here the shear planes are unfavorably aligned so the axial applied transformation stresses should be higher. Inspection of Figure 40a reveals that the agreement is very poor if the transformation is assumed to follow lattice correspondence B, while examination of Figure 40b shows a generally very good alignment of the measured stresses and Schmid Factor for correspondence C. To check if both correspondence B and C could be active, a combined analysis was carried out that found the maximum Schmid factor of both correspondences, which is plotted in Figure 40c. Rather than improving the agreement, it degrades the level of agreement between the experiment and the theory.

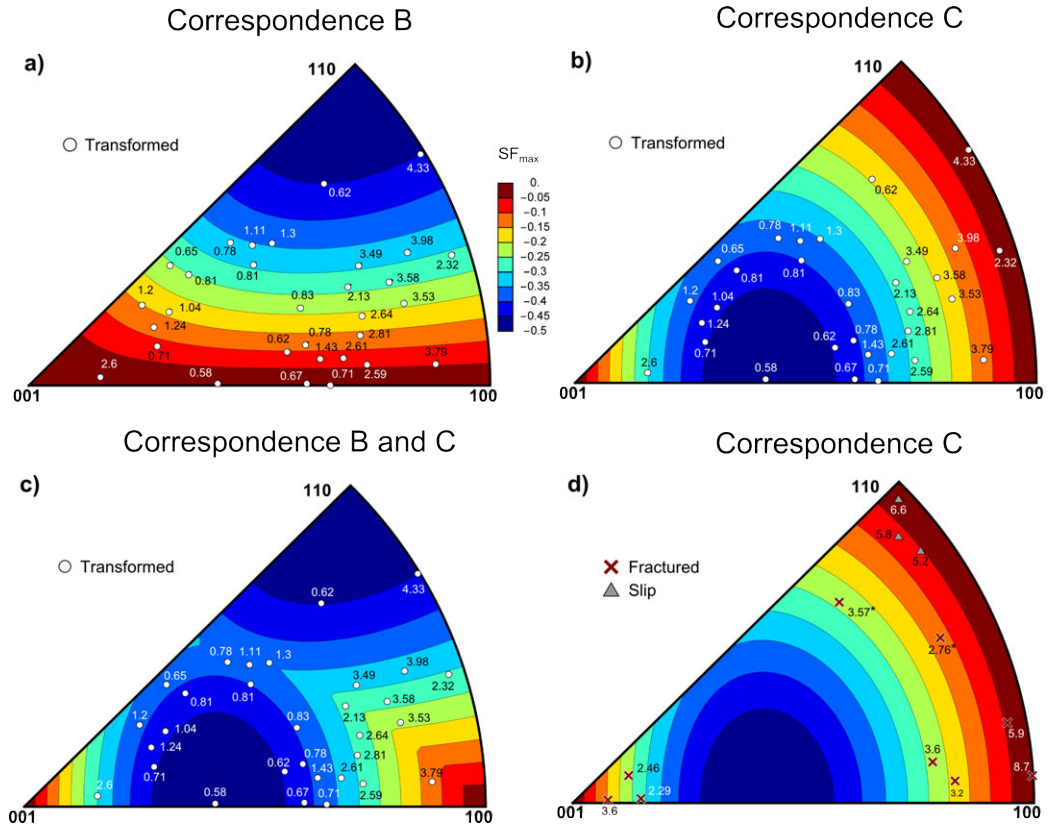


Figure 40: Standard stereographic triangle of tetragonal zirconia, with experimentally measured axial transformation stress ( $\sigma_{\Lambda pp}$  in GPa) overlaid on contours of maximum Schmid factor ( $SF_{max}$ ) based on a) correspondence B b) correspondence C and c) correspondence B and C. d) The experimentally measured critical stress for fractured and slipped pillars based on correspondence C.

Altogether, Figure 40 indicates that correspondence C alone fits the experimental data the best and this is best illustrated by plotting  $\sigma_{\Lambda pp}$  directly against  $SF_{max}$  which is shown in Figure 41. The data was fit to the equation  $\sigma_{\Lambda pp} = \alpha/SF_{max}$  using a least squares method and the resulting fit,  $\sigma_{\Lambda pp} = 0.49/SF_{max}$  matches well with the expectations from Equation 7. The 95% confidence bands shown by the gray shaded regions cover almost all the pillars that transformed, with the exception of three outliers (pillars 2, 18, and 31) which are highlighted with asterisks and are not included in the fitting; these will be discussed in more detail shortly.



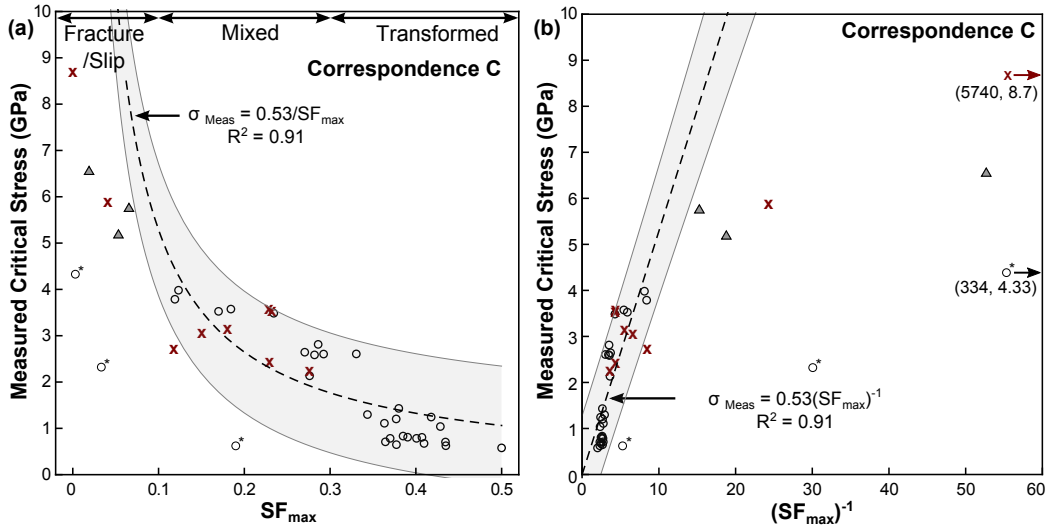


Figure 41: a) The measured critical stress versus the maximum Schmid factor for correspondence C. The fit line includes only transformed pillar data (without the three outliers), obtained by least-squares fitting of equation  $\sigma_{App} = a/SF_{max}$ , and with 95% confidence bands shown by the gray shaded region. b) Plot of critical stress versus  $SF_{max}^{-1}$  in order to produce a linear relationship.

Based on the above analysis we now take correspondence C as the only active correspondence in the present work, and can now draw more insight from Figure 40b and Figure 40d. These show the Schmid factor for correspondence C and experimental data for transformed and fractured/slipped pillars respectively. The measured transformation stresses generally decrease as the Schmid factor increases, as expected, and shown most clearly in Figure 40b where the lowest stresses lie in the dark blue regions. But for regions where the Schmid factor is very low (dark red areas) we see mostly fractured and slipped pillars, which intuitively makes sense since these pillars are expected to have very high transformation stresses, so high that other deformation mechanisms can occur first, such as cleavage or slip.

The occurrence of crystal slip in an unconfined ceramic material at room temperature may at first appear surprising, but there is precedent of such behavior in other small-scale samples like those being tested here. For example, Zou and Spolenak demonstrated plastic slip for certain orientations of micron-scale pillars made from ionic crystals (NaCl, KCl, LiF, and MgO) [62]. While Montagne et al.

showed similar results in  $\text{Al}_2\text{O}_3$  and Kiani et al. in SiC [63, 64]. In tetragonal zirconia, the expected preferred slip planes are {110} type planes when considering the tetragonal single cell BCT system, but this corresponds to {100} in the tetragonal double cell FCT system that is used for calculations in this work. This is in line with the observed crystal slip planes in cubic zirconia which are also {100} [65]. According to the Schmid factor relationship, Equation 7, a given plane will experience the greatest shear stress when it is aligned  $45^\circ$  from the applied stress direction. This condition is met for the slip planes in tetragonal zirconia (FCT) when pillars have the (110) crystal plane normal aligned with the compression axis, [001] in this case, and indeed the pillars that exhibited slip are clustered near the (110) orientation in the stereographic projection in Figure 40d.

Now taking a closer look at Figure 41a it is possible to see three distinct regions in terms of the pillar's behavior according to the Schmid factor which are labeled at the top of the figure. Beginning with the region where  $SF_{\max} > 0.3$ , here all the pillars transformed without fracture or slipping, suggesting a reliable transformation region for favorably aligned shear transformation planes lying in the blue or dark blue regions of Figure 40b. On the other hand, when  $SF_{\max} < 0.1$ , the dominant behavior was fracture or slip as seen in the red regions of Figure 40b. Interestingly, the boundary between transformation and fracture/slip in orientation space is not sharp, but rather it is quite diffuse, with pillars having intermediate values of  $SF_{\max}$  — between 0.1 and 0.3 — sometimes exhibiting clean transformations and other times fracturing, as indicated by the light blue and cyan regions of Figure 40b. Here it is suspected that the normal stresses are approaching values large enough to cause cleavage and beginning to compete with the transformation. In fact, for a few pillars the competition between transformation and cracking was very clear, as evidenced by both occurring simultaneously in the same pillar. Figure 42 shows two views of pillar 6 that has regions of transformation and a small axial crack near the top of the pillar.

The mixed region of Figure 41a contains pillars with nearly identical Schmid factors, yet some transform while others crack, therefore the type of response that is triggered in a pillar must depend upon some aspect other than the maximum Schmid factor alone. One possible explanation is small variations in factors such as pillar geometry (pillar taper, aspect ratio), mechanical loading (pillar-tip alignment), and orientation (EBSD identification). These factors might help to explain

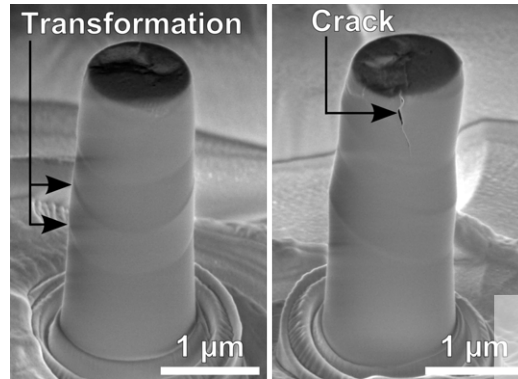


Figure 42: a) Pillar 6 with a transformation zone in pillar midsection and b) 90° rotated view of pillar 6 with axial crack indicated with the arrow [51].

the behavior of the three outlier pillars marked with asterisks in [Figure 40](#) and [Figure 41](#). Pillar 2 and pillar 31 have very low Schmid factors, 0.03 and 0.0003 respectively, so were not expected to transform when, somewhat surprisingly, they did transform. One possible explanation for this is orientation identification error; for example if the pillars contained multiple grains along their height, then it's imaginable that the indexed orientation at the top of the pillar did not coincide with the majority orientation of a grain beneath it, thereby causing a different mechanical response. Outlier pillar 18 has an intermediate Schmid factor (0.19) so it's expected to either transform or fracture, and while it does transform, it does so at a much lower stress level than predicted by [Equation 7](#). Again, pillar taper, pillar-tip misalignment, or even a surface defect that helps nucleate the transformation are possible sources of this error.

The transformation stress ( $\sigma_{A_{pp}}$ ) is plotted against  $(SF_{max})^{-1}$  in [Figure 41b](#); this has the convenience of producing a linear relationship as predicted by [Equation 8](#). The transformed pillars roughly conform to the linear relationship, with some scatter, and a regression line is fitted to the data. The very large range of the data points in this figure is due to a few pillars, which lie near the edges of the stereographic triangle, and have very low Schmid factors and therefore very large inverse values. Most of the points that lie far to the right of the trendline correspond to pillars that fractured or slipped, showing how the very high transformation stresses expected by the extrapolated trendline are never attained

when samples can access other mechanisms (fracture and slip) to accommodate the applied strain.

The slope of the fit line in [Figure 41b](#) represents the sum of all of the orientation-independent  $\Delta G$  terms from [Equation 8](#); this leaves out the elastic and frictional terms. The theoretical value of the chemical free energy was calculated using the values presented in [Table 12](#) and [Table 13](#) and the value of 0.69 GPa is surprisingly close to the measured slope of the trendline of 0.53 GPa. This agreement, while very encouraging, is subject to some caveats. First, the enthalpy of transformation used in the calculations here was measured from a bulk specimen and that would incorporate some elastic free energy, which in turn is expected to cause the bulk enthalpy to be larger than the true micro-pillar enthalpy. Second, while the assumption that the elastic energy term is close to zero for micro-pillars is properly backed by theory [[11](#)], the assumption that the frictional energy is zero is less reliable. To properly determine the frictional energy contributions, one would need to know all the defects present and their distribution as well as how the different orientations interact with the free surfaces, and both of these are challenging to ascertain. Nonetheless, we still expect the chemical energy term to be the dominant energy term, so the agreement between its values and the experimental values is considered positive.

Table 12: Materials parameters for the calculation of the theoretical transformation stress in 2 mol%  $Y_2O_3$ -5 mol%  $TiO_2$ - $ZrO_2$  (mol%).

TRANSFORMATION		MOLAR	TESTING	EQUILIBRIUM
ENTHALPY	DENSITY	MASS	TEMP.	TEMP.
$\Delta H$ (KJ/mol)	$\rho$ (g/cm <sup>3</sup> )	M (g/mol)	T (°K)	T <sub>0</sub> (°K)
2 <sup>a</sup>	6.081 <sup>b</sup>	123.1 <sup>c</sup>	298	700 <sup>d</sup>

a - Extrapolated from the area under exothermic peaks of bulk experimental DSC

b - Using measured lattice parameters: a = 5.103 Å, c = 5.184 Å [[66](#)]

c - Using a weighted average of molar mass of  $ZrO_2$ ,  $Y_2O_3$ , and  $TiO_2$

d -  $(A_s+M_s)/2$ , extrapolated from bulk experimental DSC

Another possible physical origin for the scatter, outliers, and differentiation among pillars of similar Schmid factor in [Figure 40](#) and [Figure 41](#) is the effect of other non-shear stress components on the transformation. As noted earlier, the

Table 13: Strain parameters for the calculation of the theoretical transformation stress in 2 mol% Y<sub>2</sub>O<sub>3</sub>-5 mol% TiO<sub>2</sub>-ZrO<sub>2</sub> (mol%).

CORRESPONDENCE B TRANSFORMATION SHEAR STRAIN $\epsilon_{\text{shear}}$	CORRESPONDENCE C TRANSFORMATION SHEAR STRAIN $\epsilon_{\text{shear}}$	TRANSFORMATION NORMAL STRAIN $\epsilon_{\text{normal}}$
$\pm 8.18\%$	$\pm 8.12\%$	$+0.77\%$

phase transformation in zirconia is dominated by shear but it also involves a volume change and therefore non-shear tensor terms can contribute to its activation. Each of the possible mechanical responses — transformation, cracking, and slip — are affected by these normal or hydrostatic components. To account for these effects we can adjust Equation 7 to include the normal components,

$$\sigma_{\text{app}} = \frac{\sigma_{\text{shear}}}{\cos(\chi)\cos(\lambda) + \cos(\chi)\sin(\lambda)} = \frac{\sigma_{\text{App}}}{(\text{SF} + \text{NF})} \quad (9)$$

where the  $\cos(\chi)\sin(\lambda)$  term is denoted as the normal factor (NF) and represents how the applied load is resolved normal to the shear plane. The transformation from tetragonal to monoclinic in zirconia includes a volume increase of  $\sim 4\%$  [56], so for some orientations this can work against the work done by the applied shear stress. We can account for this by combining Equation 9 and Equation 5 but this time leaving out the elastic and frictional components for simplicity,

$$\sigma_{\text{app}} = \frac{\frac{\Delta H_p}{M} \left(1 - \frac{T}{T_0}\right)}{(\text{SF} \cdot \epsilon_{\text{shear}} + \text{NF} \cdot \epsilon_{\text{normal}})_{\text{max}}} \quad (10)$$

where now instead of maximizing the Schmid factor only, we maximize the combined sum of the Schmid factor and normal factor multiplied by their respective shear and normal strains taken from the Bain strain tensor. For only some orientations will the addition of the normal factor have a pronounced affect, and in particular it affects orientations with low Schmid factors the most, thus the main effect is on fractured and slipped pillars. This is best illustrated by Figure 43 which plots the measured critical stress against the inverse of  $(\text{SF}\epsilon_{\text{shear}} + \text{NF}\epsilon_{\text{normal}})_{\text{max}}$  in a similar manner to Figure 41a. The effect of the normal factor

on transformed pillars is small, as indicated by the nearly identical fit line. However, the fractured and slipped pillars are much more affected as shown by their shifts along the x-axis noted by the gray horizontal lines. The only transformed pillars that are affected are the outlier transformed pillars which lie far to the right of the trend line. The inclusion of the normal factor appears to make the fractured, slipped, and transformed outliers even less favorable for transformation by moving them further away from the transformation stress line (dashed line).

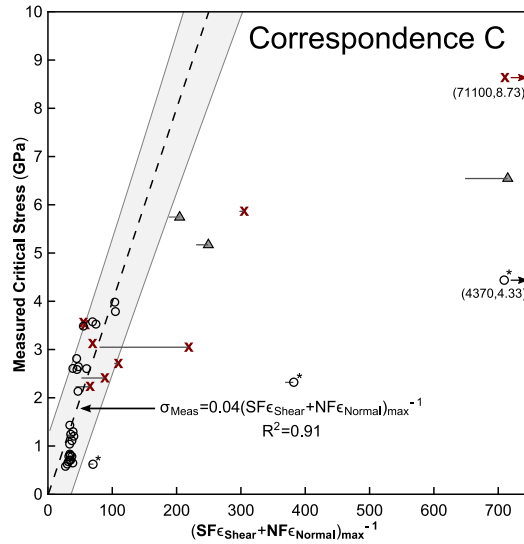


Figure 43: Plot of measured critical stress (transformation, fracture, or slip) vs. maximum  $(SF\epsilon_{Shear} + NF\epsilon_{Normal})_{Max}^{-1}$  for correspondence C. Incorporation of the normal factor component only shifts the position of fractured, slipped, and transformed outlier pillars as indicated by the horizontal gray lines.

#### 4.6 ORIENTATION DEPENDENT SIZE EFFECTS

Up to this point we have presented several possible sources of scatter in the micro-compression tests such as pillar-tip misalignment, orientation uncertainty, slight variations in pillars taper and aspect ratio, and normal stress effects. But there is one systematic physical contribution to the scatter that has yet to be explored in shape memory materials of any kind — orientation dependence of sample size effects. The influence of sample size on the critical transformation stress is already relatively well established in martensitic materials [11, 13, 49], however we are

currently unaware of any investigation into the effect, if any, that crystal orientation has on the size effects. It is plausible that some of the free energy terms in Equation 5, which are already known to be sensitive to structure and sample size, could also be sensitive to the sample orientation.

A preliminary investigation into the orientation dependence of sample size effects is shown in Figure 44. Two orientations were examined — one oriented near (101) and the other near (201) — and both show a trend of increasing critical stress as the pillar diameter increases. This is in line with the work presented earlier for shape memory ceramic micro-pillars (Section 3.3), but this is opposite of the effect typically seen in shape memory metals, which tend to get stronger as they get smaller [11, 49]. This may speak to a dominance of a different term in the energy balance of Equation 5 for ceramics than for metals. For example, one major difference between metals and ceramics is their stiffness; zirconia has a Young's modulus (~200 GPa) that is almost an order of magnitude higher than that of metals, e.g. Cu-Ni-Al shape memory alloys (~25 GPa). As a result, the elastic energy term in the Gibbs free energy equation might be much more significant for ceramics than for metals. In fact, in shape memory metals the dominant free energy term is usually assumed to be the internal friction which increases as the pillar size decreases and accounts for their size effects.

Here it is hypothesized that the stored elastic energy term dominates the other terms due to the high stiffness of zirconia. Work done by Chen and Schuh calculated that the elastic stored energy in Cu-Ni-Al shape memory alloys with Young's modulus of 26 GPa could increase the transformation by as much as 20 MPa as the pillar diameter increased towards a "bulk" response. So the higher stiffness of zirconia could have transformation stress increases in the hundreds of megapascals.

What is most interesting is that there appears to be a different size effect depending on the crystal orientation of the pillar as shown in Figure 44c. The data sets for the two pillars have different slopes which indicates some orientations could be more sensitive to size effects. Again, this could be due to orientation dependent free energy terms that are influenced by how the transforming martensite interacts with free surfaces. It is clear that more work is needed in this area, as only two orientations were examined here and with only three different pillar diameters.

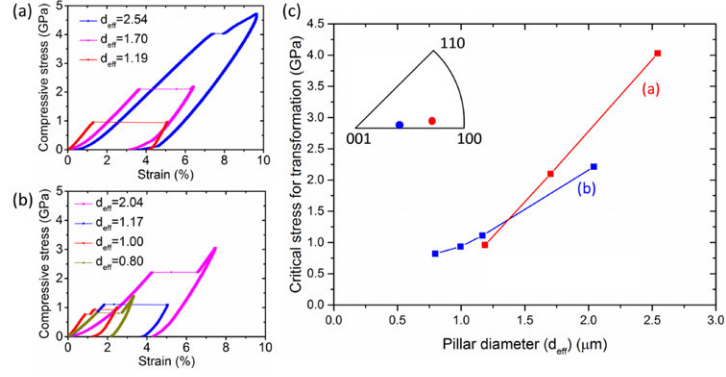


Figure 44: Stress-strain curves for different diameter pillars a) near (201) oriented, Euler angles = [258, 60, 147] and b) near (101) oriented, Euler angles = [259, 43, 290]. c) the critical transformation stress as a function of pillar diameter for pillars with different crystal orientations [51].

#### 4.7 ORIENTATION EFFECT ON TRANSFORMATION STRAIN

The final orientation dependent shape memory property that will be explored is the transformation strain. It is one of the characteristic features of shape memory materials, a large strain plateau caused by the rapid phase transformation and many such plateaus were observed in this work. To properly calculate the transformation strain it is critical to know how much each pillar transformed; as noted earlier, most pillars only demonstrated partial transformation so it is not enough to know just the starting pillar height and displacement plateau magnitude for strain calculations, we need to know how much of the pillar transformed. This was accounted for by calculating the transformation percentage ( $f_{trans}$ ) as discussed in Figure 34b. The reported axial transformation strain ( $\epsilon_{trans, meas}$ ) is then a corrected measured strain,

$$\epsilon_{trans, meas} = \frac{\Delta h_{plateau, meas}}{f_{trans} \cdot H_{pillar}} \quad (11)$$

where  $\Delta h_{plateau, meas}$  is the displacement measured in the plateau region and  $H_{pillar}$  is the initial pillar height.

The starting point for theoretical strain calculations is the transformation strain tensor, also known as the lattice deformation tensor ( $F$ ), which converts a tetragonal unit cell to a monoclinic unit cell. The values used for each correspondence are



slightly different [56], but they have similar forms, like the transformation strain tensor shown here for correspondence C,

$$\begin{bmatrix} \frac{a_m \sin(\beta)}{a_t} & 0 & 0 \\ 0 & \frac{b_m}{a_t} & 0 \\ \frac{a_m \cos(\beta)}{a_t} & 0 & \frac{c_m}{c_t} \end{bmatrix} \quad (12)$$

where  $a_t$  and  $c_t$  are the tetragonal unit cell parameters and  $a_m$ ,  $b_m$ ,  $c_m$ , and  $\beta$  are the monoclinic unit cell parameters. One further operation is required, polar decomposition to account for lattice rotations, which yields what is known as the Bain strain tensor, B, and that is what is finally used to calculate the strain. Here it is assumed that the biasing stress applied during micro-compression results in the formation of only one variant of martensite and therefore no lattice invariant shear is included in the calculation. The transformation strain for a given orientation can then be calculated for any vector as,

$$\begin{pmatrix} v'_x \\ v'_y \\ v'_z \end{pmatrix} = B \begin{pmatrix} v_x \\ v_y \\ v_z \end{pmatrix} \quad (13)$$

where B is the Bain strain tensor for a given correspondence and variant.

To calculate the expected axial strain during a pillar compression test, we begin with the [001] vector and apply the Bain strain tensor to obtain a new vector,  $v'$ . The deformation along the compression direction axis is represented by the component  $v'_z$  that lies along the compression direction, and the strain can then be found using the following equation,

$$\epsilon_z = v'_z - 1 \quad (14)$$

In order to apply this analysis to all possible crystal orientations, we must rotate the Bain strain tensor over all of orientation space using,

$$\begin{pmatrix} v'_x \\ v'_y \\ v'_z \end{pmatrix} = RBR^T \begin{pmatrix} v_x \\ v_y \\ v_z \end{pmatrix} \quad (15)$$

where R and  $R^T$  represent the rotation matrix generated from the Euler angles and its transpose, respectively. [Figure 45](#) maps the expected theoretical strains for

all pillars for correspondence C as color contour lines with the experimentally measured strains for the transformed pillars overlaid on top.

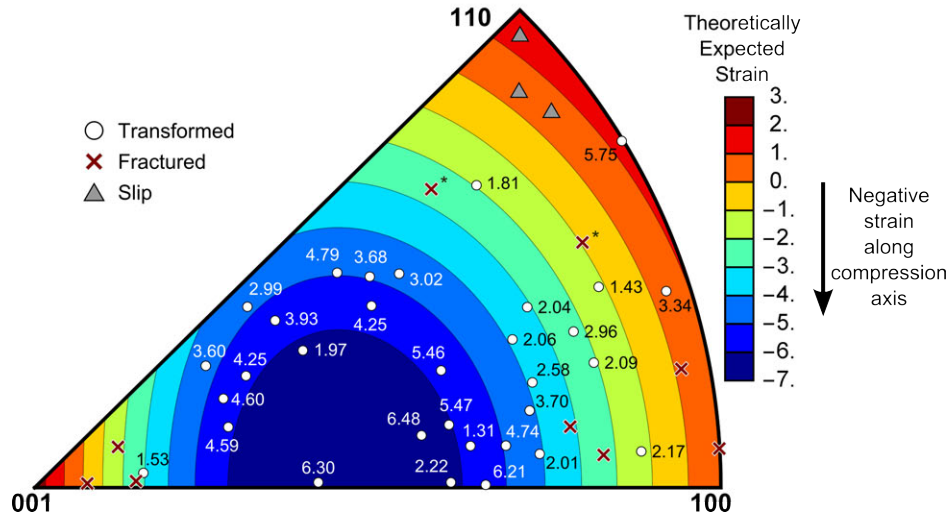


Figure 45: Standard stereographic triangle with theoretical transformation strains given as colored contour lines. The experimentally measured data is overlaid as the data points. The outlier pillars, noted by asterisks are not included in the fit.

The map in Figure 45 shows there is a large range of possible transformation strains from negative 7% (a compressive transformation strain) to positive 3% — positive indicating the transformation would actually favor tensile elongation along the compression axis. The areas with the largest expected strains are identified as lying near the [101] pole and in general the pillars that manifested the largest strains lie near this region, towards the bottom middle of the stereographic triangle in dark blue colored areas. Another especially interesting feature of Figure 45 is the regions near the [001], [100], [110] poles where positive strains are predicted from the crystallographic analysis. Since a positive strain is not compatible with the applied compressive stress, we expect that these orientations could not transform during compression. It is therefore encouraging that this is indeed what is generally observed with pillars that have positive expected strains (red and orange regions) mostly exhibiting fracture or crystal slip without transformation.

Finally, the theoretically expected strains are plotted against the measured strains in Figure 46. The outlier pillars — in terms of transformation stress — are also

highlighted with asterisks and as expected they are also outliers in terms of strain. Apart from the outliers and some experimental scatter, the agreement between theory and experiment is reasonable. The least squares fitting, (fit to  $y = ax$ ) and the 95% confidence bands shown in gray cover most of the data and encompass the expected  $\epsilon_{\text{meas}} = \epsilon_{\text{theo}}$  trend.

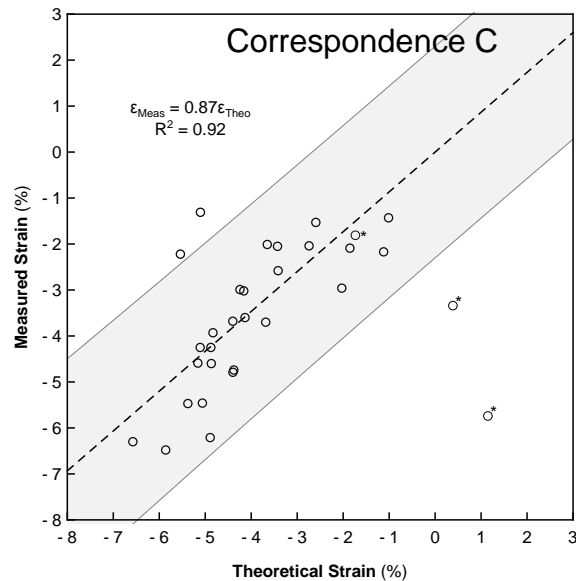


Figure 46: The experimentally measured pillar strain versus the theoretically calculated strain for correspondence C.

#### 4.8 CONCLUSIONS

This chapter explored the effect of the pillar crystal orientation on the shape memory properties such as elastic modulus, transformation stress and strain, and fracture behavior. Knowledge of the relationship between orientation and properties is crucial for small scale structures especially those with carefully engineered single crystalline or oligocrystalline structures. These mesoscale structures can not use averaged materials properties which are a suitable approximation for polycrystals. The small number of grains and grain orientations mean that a full prediction of the properties requires exact knowledge of each grain and its properties.

Here we produced orientation maps for the critical transformation stress which show that some orientations will fracture or slip instead of transformation. Orientation maps for the transformation strain were also produced and indicated that some orientations can not be transformed by compression because they have expected tensile extensions that are incompatible with a compressive loading state. It is hoped that the orientation maps produced in this chapter will be useful as design criteria when optimizing the shape memory properties in small scale zirconia.

## SCALE UP METHODS

---

So far all of the work presented has exclusively studied the properties of shape memory ceramics in the form of micro-pillars. This was mainly due to the ease of fabrication of the micro-pillars and how their dimensions and orientations could be carefully controlled, making them ideal for rigorous scientific studies. Unfortunately, micro-pillars are not well suited for most practical applications because the FIB milling technique is not scalable and the samples remain very small, less than a few cubic micrometers. In order for shape memory ceramics to arrive in real world applications they must be scaled-up into larger volumes and into more useful geometries such as free particles, wires, foams, and thin films. An excellent summary of the possible geometries, [Figure 47](#), has been shown for magnetic shape memory metals [13]. This chapter will describe the efforts made to produce macro-scale shape memory ceramics that maintain a given dimension on the micrometer scale to avoid stress concentrations that lead to fracture and each geometry — free particles, wires, foams, and thin films — will be discussed in turn.

### 5.1 PARTICLES AND POWDER

To begin, we will examine the most straightforward scale-up method, free standing particles. A free particle can essentially be viewed as a micro-pillar that was removed from its substrate; but particles have the advantage of being able to be produced in great quantities using mass production methods. Furthermore large amounts of particles can be gathered together as a collection, which will be referred to here as powders, and this is an ideal way to maintain the micron-scale size necessary for enhanced performance yet produce large scale objects.

As noted in [Section 2.4](#) and [Section A.1](#) the bulk polycrystalline zirconia was produced via a common co-precipitation method [23, 24, 31] that produced irregularly shaped particles which were mostly smaller than 2  $\mu\text{m}$ . This is shown in the

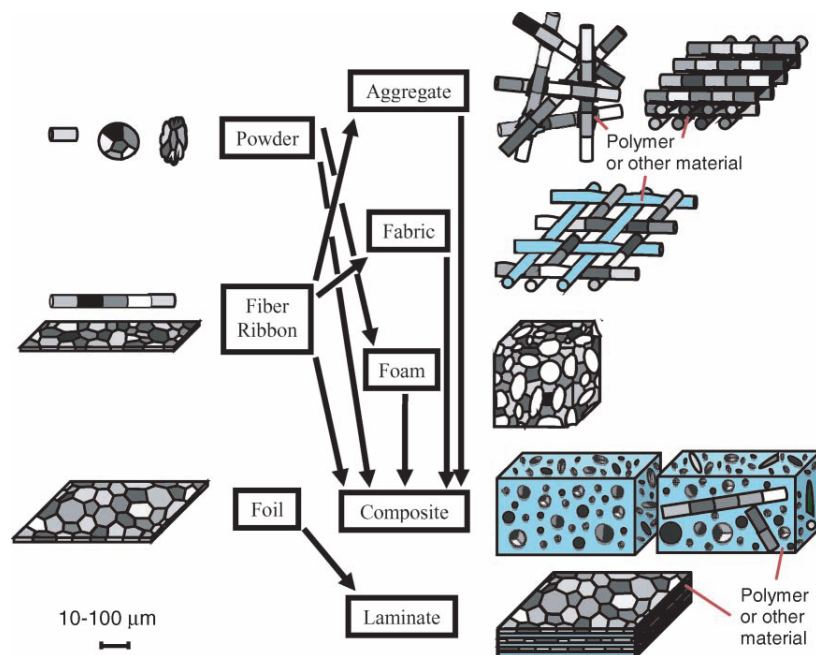


Figure 47: Examples of macroscopic oligocrystalline structures with "elements" shown on the left and "constructs" built from the elements shown on the right [13].

particle size distribution in Figure 48a which was collected with laser diffraction in ethylene glycol. Upon drying and calcination, the particles tended to agglomerate and grow to yield particles with diameters that were generally larger than  $45\ \mu\text{m}$  as shown by the particle size distribution in Figure 48a as collected by sieving. This method can easily be scaled to produce powders on the tonnage scale.

- This work done in collaboration with:

Dr. Hang Yu at MIT

Dr. Zehui Du at Nanyang Technological University

### 5.1.1 Superelastic Properties of Micron-Sized Particles

The first step to prove that powders can be useful for large scale applications is to show that individual particles do indeed demonstrate the necessary shape memory properties. The pillars tested previously demonstrated excellent shape memory properties but there is likely a lower limit to the size of a pillar or particle

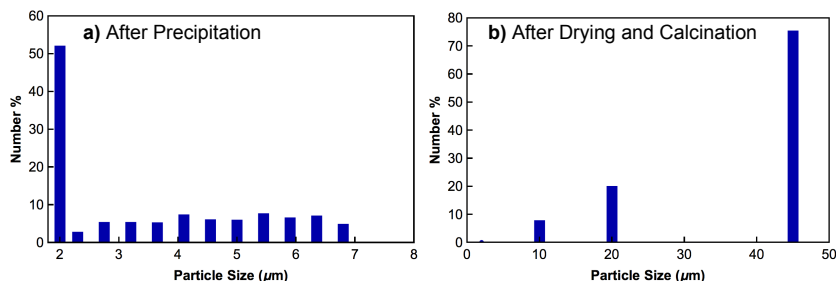


Figure 48: Particle size distributions for a) as-precipitated powders and b) dried and calcined powders.

where the phase transformation will occur since it has been shown that nanoparticles do not demonstrate the transformation [67]. Here the goal was to show that these particles will demonstrate superelasticity.

To make micron scale particles with uniform diameters, a controlled precipitation technique was used. Zirconium and cerium metal salts were mixed and slowly precipitated with an acid catalyst. This was followed by aging for up to 48 hours to slowly grow the particle size. The particles were then dried and sintered at 1400°C for 30 minutes to ensure full crystallization. The final particle composition was 16 mol% CeO<sub>2</sub> which is expected to produce superelastic properties.

To test these particles, they were distributed on top of a sapphire substrate followed by compression to measure the mechanical properties; this type of setup brought about a few experimental challenges. Previously micro-pillars were located using the imaging capabilities of a cono-spherical tip, but for loose particles this could cause translation of the particles and make alignment difficult. To overcome this an in-situ nanoindenter was used (Hysitron PI-85 PicoIndenter) that was loaded in a scanning electron microscope to simultaneously indent and obtain an image, allowing precise alignment.

The results of the in-situ indentation are shown in Figure 49. The first cycle, Figure 49a, is a typical superelastic cycle with loading and unloading displacement plateaus. There was some residual displacement measured which is likely due to indentation effects between the tip and the particle or the particle and the substrate. Subsequent cycles, such as the fourth cycle shown in Figure 49b, have smaller amounts of residual displacement. Further cycling showed the character of the load-displacement curve changes slightly, with the 148<sup>th</sup> cycle shown in Figure 49c, but the residual strain completely disappears while still maintain-

ing the energy dissipation ability as indicated by the non-zero area within the curve. The particle was cycled a total of 502 times with the final load displacement curve shown in Figure 49d still showing excellent superelasticity. The particle was imaged before and after 502 compression cycles, Figure 49e and Figure 49f respectively, and while it has changed shape somewhat, there are no visible cracks or fractures — a very positive result for so many cycles. These results are very promising because they show that micron sized particles can indeed transform without cracking.

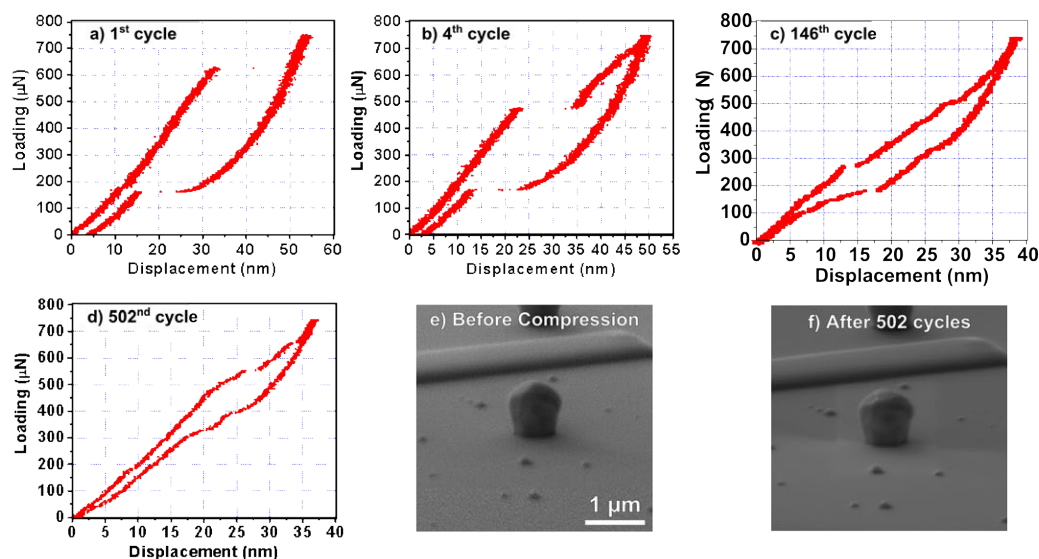


Figure 49: Superelastic load-displacement curves for a single particle on a sapphire substrate a) 1<sup>st</sup> cycle, a) 4<sup>th</sup> cycle, a) 146<sup>th</sup> cycle, and a) 502<sup>nd</sup> cycle. e) The particle before compression testing and f) after the 502<sup>nd</sup> cycle [Data and figure courtesy of Zehui Du, unpublished data, 2016].

### 5.1.2 Shape Memory Ceramic Powders

Individual particles can be assembled together in large quantities to produce a macro-sized object by simply encapsulating the particles in a casing. Each particle may be in close contact with neighboring particles but they will not be intimately connected and therefore should be able to transform freely without major constraints from other particles. An encapsulated powder assembly is expected to



demonstrate both the shape memory effect and superelasticity with the improved properties that accompany small-scale structures.

To probe the properties of powder assemblies, a set of experiments were carried out that compressed powders in a mechanical die; the goal here was to prove that a collection of particles could indeed transform when loaded together. A schematic of the testing apparatus is shown in Figure 50 where an amount of powder was loaded into a high strength steel die that encapsulated the powder in disk form that could be loaded using a standard compression tester (Instron 5900R-4505).

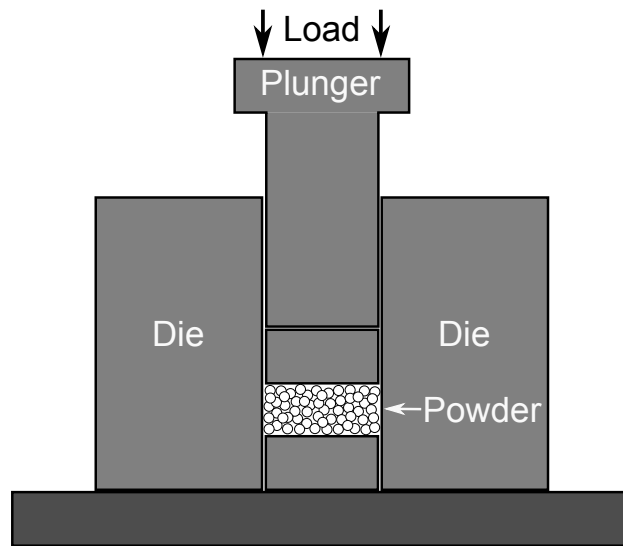


Figure 50: Die and powder experimental setup for quasi-static testing of powder compacts.

For each test 0.1 g of powder was loaded into a die with a 6 mm inner diameter, then compressed in displacement control mode. After compression the disks were approximately 0.8 -1.0 mm thick. Many cycles were repeated to ensure that the processes were repeatable and properly reflected the material properties of the powder and not simply a compaction and rearrangement of the particles. To investigate the full spectrum of shape memory properties, powders were made with three different compositions via co-precipitation of CeO<sub>2</sub>-doped zirconia.

### 5.1.2.1 Shape Memory Powder – Irreversible Twinning of Martensite

To observe shape memory properties in particles, a batch of powder was fabricated with 10 mol% ceria resulting in a powder that were nearly 100% martensite (monoclinic). The stress-temperature diagram in Figure 51a shows that if stress is applied at room temperature (as indicated by the vertical arrow in the figure) this composition is not expected to cross the martensite-austenite phase boundary. However, certain martensite variants can be aligned in the direction of the applied stress, in other words certain textures can be developed which is exactly what is seen in the x-ray diffraction data.

The loose powders were analyzed with x-ray diffraction prior to compression, Figure 51b, and monoclinic peaks were observed at  $28.1^\circ$  and  $31.4^\circ$  which correspond to the  $\bar{1}11$  and  $111$  planes respectively. After compression, another XRD pattern was collected from the pressed disk, Figure 51c, which still shows peaks at  $28.1^\circ$  and  $31.4^\circ$  but their relative intensities have changed; now the  $111$  peak is larger whereas prior to compression the  $\bar{1}11$  peak was dominant. This signifies a change in the texture due to the applied stress converting some martensite variants into different martensite variants that are preferred for the given stress state.

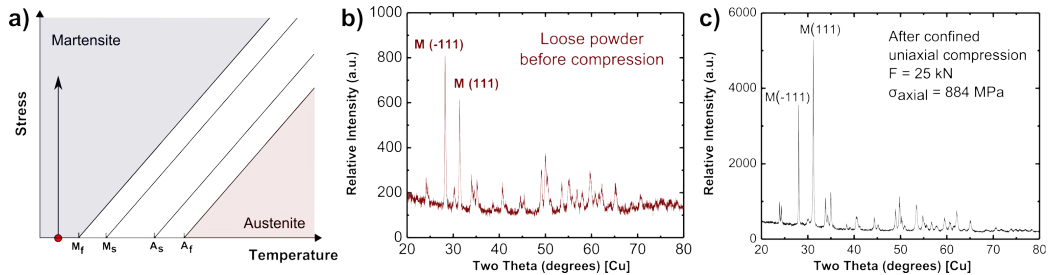


Figure 51: a) Stress-temperature diagram of shape memory powders (10 mol%  $\text{CeO}_2$ ) (b) XRD pattern of loose powders before compression with majority  $\bar{1}11$  peaks and (c) XRD pattern of compacted powders after compression with majority  $111$  peaks indicating a different texture [data courtesy of Dr. Hang Yu].

### 5.1.2.2 Superelastic Powder – Reversible Austenite-to-Martensite Transformation

Shifting the composition by doping with more ceria, up to 13.2 mol%  $\text{CeO}_2$ , results in a change of the room temperature phase from martensite to austenite and

therefore changes the expected mechanical behavior to superelasticity instead of shape memory as seen in the previous section. Figure 52a illustrates the expected response, an applied stress will cross the austenite to martensite phase boundary and initiate the phase transformation. However, removing the stress will retrace the same path and cross the phase boundary again thereby returning the material to its original austenite state.

The XRD patterns of the loose powders before compression are shown in Figure 52b and majority peak is at  $30^\circ$  which corresponds to austenite (tetragonal zirconia). The XRD pattern after compression is still dominated by the austenite peak but small peaks are seen at  $28.1^\circ$  and  $31.4^\circ$  that correspond to martensite.

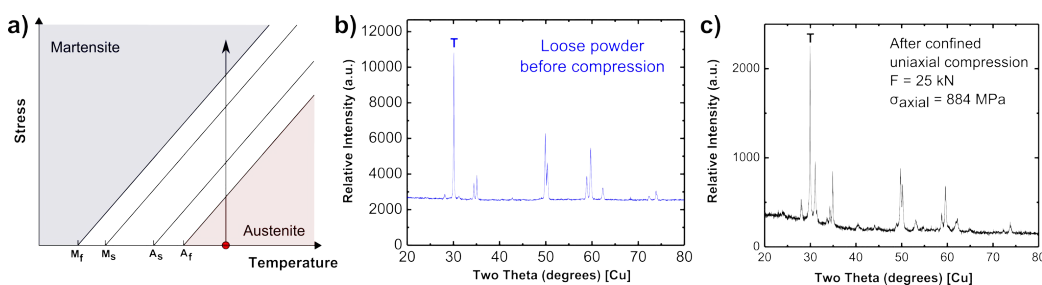


Figure 52: a) Stress-temperature diagram of superelastic powders (13.2 mol%  $\text{CeO}_2$ ) (b) XRD patterns of loose powders before compression with majority tetragonal phase and (c) compacted powders after compression with mostly tetragonal but some monoclinic peaks present [data courtesy of Dr. Hang Yu].

It is expected that most of the material transformed from austenite to martensite on loading and then reverted back to austenite on unloading, but it is possible that a small portion remained as martensite after unloading. Here we hypothesize three possible explanations for the retained martensite:

- *Variation in Crystal Orientation* — It was shown in Chapter 4 that the crystal orientation has a strong effect on the stress required to initiate the transformation. Since a large collection of particles will express every possible crystal orientation then all of the different mechanical responses are possible. So some particles could transform in both directions (a full superelastic cycle) but some could have an irreversible response such as slip.
- *Variation in Particle Size* — The particle size in shape memory materials can have an enormous effect in the mechanical response. If the particle size is

small enough it can completely hinder the transformation. The particle size can also alter the observed transformation temperatures, so some particles may not actually lie in the position indicated in the stress-temperature diagram shown in [Figure 52a](#) which would change their behavior drastically.

- *Variation in Stress State* — Finally, each particle will lie in its own unique environment, with different neighboring particles and different amounts of contact with those neighbors. Also each particle will have a slightly different geometry. All of this means each particle will experience distinctive stresses, some higher than others, and some more uniform than others. As a result some particles could go through some kind of irreversible transformation to martensite.

#### 5.1.2.3 *Intermediate Powder – Irreversible Austenite-to-Martensite Transformation*

The final composition that was examined contained 12 mol% CeO<sub>2</sub> and its A<sub>s</sub> and M<sub>s</sub> are expected to straddle room temperature as shown in the stress-temperature diagram in [Figure 53a](#). The starting phase was measured via XRD as almost completely austenite, so loading is expected to cross the austenite to martensite phase boundary resulting in a transformation to martensite. But what is especially interesting about this composition is that subsequent unloading will not cross the martensite to austenite boundary and therefore the final phase will be martensite. This was confirmed with the XRD patterns, in [Figure 53b](#), that showed the starting loose powders were austenite but after compression, in [Figure 53c](#), the XRD patterns had definitive martensite peaks implying an irreversible transformation. Some austenite did remain after compression and that can be explained by the same reasons presented in the previous section — variations in orientation, stress, and particle size.

#### 5.1.3 *Concluding Thoughts on Particles and Powders*

All of the results presented here about shape memory powder assemblies conclusively demonstrate that a collection of particles can demonstrate shape memory properties. This, in combination with the results that show individual particles can obtain hundreds of superelastic cycles without cracking or fracture, suggests

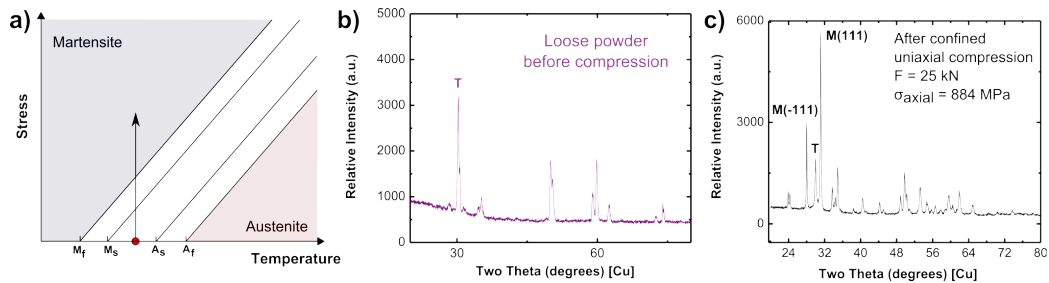


Figure 53: a) Stress-temperature diagram of intermediate powders (12 mol% CeO<sub>2</sub>) (b) XRD pattern of loose powders before compression with majority tetragonal phase and (c) XRD pattern of compacted powders after compression with mostly monoclinic phase indicating a successful stress-induced transformation [data courtesy of Dr. Hang Yu].

that the powder-route has great potential for real applications specifically those where energy dissipation is desired.

## 5.2 OLIGOCRYSTALLINE WIRES

Another oligocrystalline form is a bamboo structured wire or fiber where the grain size is controlled so that each grain spans the entire wire diameter as shown in the schematic in [Figure 54a](#). In an ideal bamboo structure, each grain is in contact with a free surface, and while there are grain boundaries, there are no triple junctions; thus creating a structure that should reduce mismatch stresses between neighboring grains which can cause fracture. This concept has been illustrated for shape memory metals [11, 16, 68, 69, 70] where oligocrystalline melt-spun wires were produced with large diameter-spanning grains. An example of an actual wire is seen in [Figure 54b](#).

*- This work done in collaboration with:  
Dr. Zehui Du, Xiaomei Zeng, and Pengcheng Ye  
at Nanyang Technological University*

The advantage of these oligocrystalline wires is that they show properties similar to single crystals (ability to cycle through the transformation many times without fracture) but without the difficulties associated with creating single crystals. This concept of oligocrystalline shape memory metals was discussed in [Sec-](#)

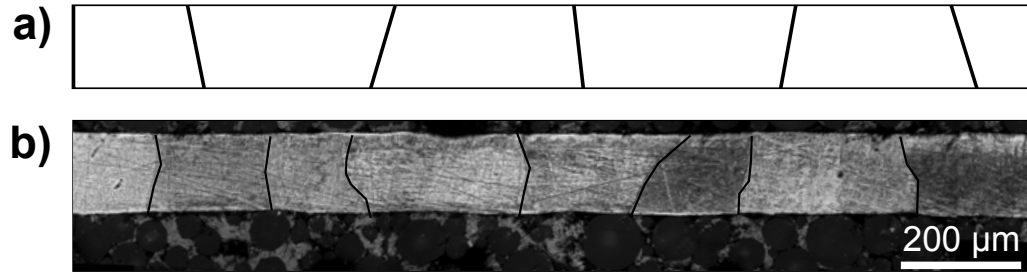


Figure 54: a) Schematic of a bamboo structured wire with grains that span the diameter and (b) actual copper based SMA oligocrystalline wire. [courtesy of Nihan Tuncer]

tion 3.1 and is most clearly shown in the stress-strain diagrams in Figure 5 which shows oligocrystalline wires undergoing repeated superelastic cycles.

However, oligocrystalline wires have yet to be demonstrated in ceramic shape memory materials, mainly due to difficulties in processing because of their high melting temperatures that can be in excess of 2700°C. This is in contrast to metals, which have lower melting temperatures and therefore can be melt spun into ribbons or drawn into wires using the Taylor drawing technique, where molten metal is drawn within a softened glass [71]. This is not a feasible method for ceramics since there is no glass or other material that can be used as the soft drawing casing.

Another melt based method is inviscid melt spinning which has been used to create alumina wires with diameters of hundreds of microns [72]. Molten ceramic is extruded through an orifice using gas pressure, and the strand exits into a reactive atmosphere that forms a thin stabilizing layer that prevents Rayleigh instabilities and breakup [73, 74]. Nevertheless, inviscid melt spinning still requires melting the ceramic making it challenging; an ideal method would not require molten ceramic. In the next section we will examine low temperature processing of ceramic wires via electrospinning.

### 5.2.1 *Electrospinning of Shape Memory Ceramic Wires*

For this work electrospinning was chosen as the method to produce ceramic wires because it does not require melting and can produce wires with diameters in the

range of nanometers to micrometers. The process applies a voltage to a stream of liquid, typically a polymer liquid, causing the liquid to become charged; at some point the repulsive forces from the electric charging will overcome the surface tensions of the liquid and the liquid will form into a long thin stream [75]. As the stream continues in space it will become thinner and also dry into a thin fiber or wire which can be collected. To make a ceramic wire, ceramic precursors can be added to the liquid and will be incorporated into the final wire. More information about the electrospinning process can be found in the literature [76, 77, 78].

To prepare the polymer solution in this work yttrium nitrate in 38.3 wt% 2-methoxyethanol, herein referred to as MOE, was mixed with titanium isopropoxide. This mixture was then added dropwise to zirconium butoxide (80 wt% in butanol). Finally, polyvinylpyrrolidone (PVP, MW = 1300k) was added and stirred for 24 hours. The solution was passed through a 0.22  $\mu\text{m}$  filter and degassed under vacuum for 10 minutes. The final solution chosen for the work was 6 mol% Y and 4.9 wt% PVP. This was fed into the syringe and discharged at a constant flow rate into a spinneret needle where the final jet was formed with the application of a high voltage. The critical process variables factor that determine the final wire diameter and morphology are the polymer solution flow rate and the applied voltage.

Examples of as-deposited electrospun wires are shown in [Figure 56](#) and individually they appear to be straight and have uniform diameter, although there is some wire to wire diameter variation. The wire diameter here is in the range of hundreds of nanometers and the as-deposited wires do not show any discernible microstructure. However, heat treatment is expected to grow the grains and a series of anneals from 1100-1500°C were carried out to investigate this. [Figure 57a](#) presents a micrograph of a wire annealed at 1100°C for 2 hours and its grain morphology is clearly visible with a mean grain size of approximately 100 nm. Further annealing to 1300°C for 2 hours results in additional grain growth up to 250-300 nm, [Figure 57b](#). A maximum grain size of ~750 nm was achieved after an annealing at 1500°C for 30 minutes. This created the near oligocrystalline wire shown in [Figure 57c](#) where the grains almost span the entire grain diameter and it is likely very few triple junctions existed within the wire interior.

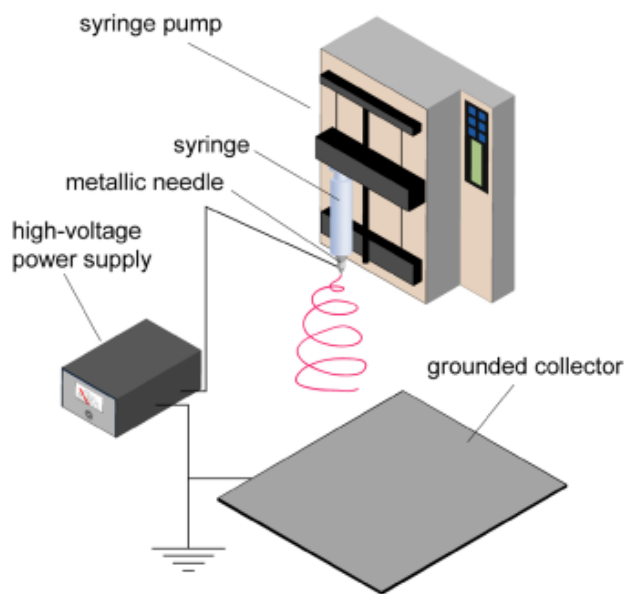


Figure 55: Schematic of a typical electrospinning setup with high voltage supply, syringe, and grounded collector plate. In this work a roller collector was used [78].

These near oligocrystalline wires would be ideal for micro-tension testing to examine their mechanical properties. Unfortunately, as of this writing the mechanical testing is still in the early stages and the results have yet to be compiled.

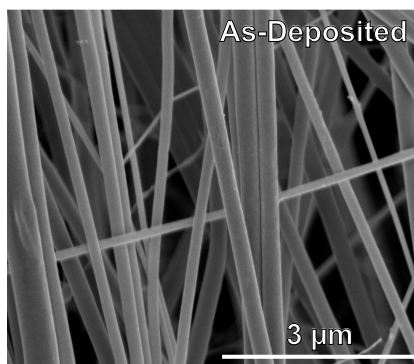


Figure 56: As-deposited electrospun ceramic wires.



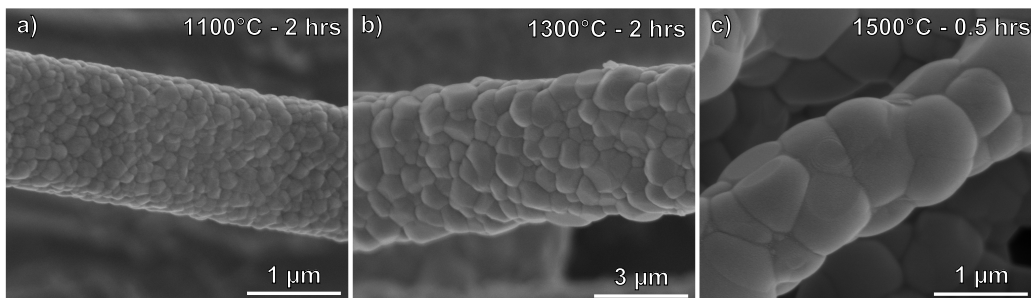


Figure 57: Annealing the ceramic wires increases the grain size. Here the wires were annealed at a) 1100°C for 2 hours, a) 1300°C for 2 hours and, a) 1500°C for 0.5 hours. Higher annealing temperatures lead to larger grain sizes.

### 5.2.2 Concluding Thoughts on Oligocrystalline Wires

Electrospinning was used to produce micro-sized fibers of CeO<sub>2</sub> doped zirconia with compositions expected to demonstrate shape memory properties. The important processing parameters were investigated such as the polymer-ceramic solution flow rate and the applied voltage. The as-produced wires were polycrystalline with small nanometer-scale grains, but annealing treatments up to 1500°C demonstrated that near oligocrystalline wires could be produced. Mechanical characterization of the wires still needs to be carried out. One of the most exciting aspects of wire structures is the possibility of withstanding tensile loads, something that is un-common for ceramics.

## 5.3 FOAMS

Foams, also known as cellular solids, are macro scale structures that are comprised of struts of solid material surrounded by air filled voids or pores. They have a variety of attractive properties such as low relative densities, high thermal insulation, and large compressive strains [79]. In terms of small volume shape memory materials, foams are attractive by virtue of the free surfaces created between the struts and the voids which can alleviate transformation mismatch stresses. In turn, this allows for the formation of oligocrystalline structures if the grain size is similar to the strut diameter thus imparting the enhanced shape memory properties.

Many different materials can be made into foams using many different processing methods. For example, polymeric foams can be made via gas foaming, phase separation, precipitation, and templating [80]. While metallic foams can be made by casting, direct gas injection, solid-gas eutectic solidification, spray foaming, and powder metallurgical methods [81, 82, 83]. Additionally, foams can be made with ceramics and in this section we will discuss several ceramic foam fabrication methods; ultimately a freeze-casting method was chosen to make shape memory ceramic foams with oligocrystalline structures. The last part of this section will examine the shape memory properties of the resulting foams.

- *This work done in collaboration with:  
Xueying Zhao at MIT*

### 5.3.1 *Fabrication of Ceramic Foams*

Many processing methods are available for the production of ceramic foams and many are similar to the methods used to make polymer and metallic foam. They are often classified by differentiating some part of the production process such as, direct vs. indirect foaming, templated vs. non-templated, or low vs. high temperature. But in order to achieve improved shape memory properties we mostly care about the differences in the final foam structure, so here the production methods will be classified by the final form of the foam produced, either random or ordered structures.

- *Randomly Structured Foam Production Methods* — These production methods typically rely on a random distribution of pores that are either directly added to a slurry or are formed by burning out a polymer phase during sintering. Direct foaming of a ceramic-polymer slurry followed by polymerization was used to make alumina foams [84]. Gel-casting [85] and sol-gel oil-emulsion methods [86] have been used to create the foam structure upon sintering. High temperature superplastic deformation can also make ceramic foams with a random distribution of pores [87].
- *Ordered Foam Production Methods* — The most common way to make highly ordered foams is by applying a ceramic slurry to a pre-existing foam tem-

plate. This has been done to make alumina foams from a polyurethane template [88] and silicon carbide foams from wood templates [89, 90]. A lithography based method was used to make a highly uniform polymer scaffold that was then coated with alumina using atomic layer deposition [91]. For all of these methods, if the template has a regular structure then the resulting foam will mimic the starting structure, however one caveat is that the struts tend to be hollow since the ceramic material is coated around the template.

For this work we wanted to choose a ceramic processing method that allowed precise control of the foam structure to ensure an oligocrystalline product but would produce solid non-hollow struts. None of the methods presented above can achieve both of these goals so a different method, freeze casting, was chosen that can produce ordered foams with solid struts.

### 5.3.2 *Freeze Casting*

The freeze casting procedure is illustrated in the pressure-temperature phase diagram of water in [Figure 58](#). It begins at (i) with ceramic particles dispersed in a liquid suspension; the liquid is typically aqueous but can be other liquids. The slurry is then directionally frozen (i  $\rightarrow$  ii) in a controlled manner which, if done correctly, can impart a well defined microstructure to the frozen liquid. During freezing the solidification front of the liquid pushes out ceramic particles and they form a cellular network around the frozen liquid. The cooling step is the most crucial for determining the final foam structure, and varying the cooling rate will produce different microstructures such as columnar or dendritic ice grains [92]. When fully solidified the frozen liquid can be removed via sublimation (ii  $\rightarrow$  iii) by maintaining low temperatures and reducing the pressure. This will produce a porous green ceramic body (ii) and often times a binder is added to the starting slurry to ensure sufficient green strength. The final step is high temperature sintering (iii  $\rightarrow$  iv) to fuse the ceramic particles together and increase the total strength and produce the final foam (iv).

Freeze casting has been applied to make from ceramics such as alumina [93], pure zirconia [94], and yttria stabilized zirconia [95] but none of these investigations used a material with shape memory properties. Here we made zirconia

foams via freeze casting and varied the composition with ceria doping to control the shape memory properties.

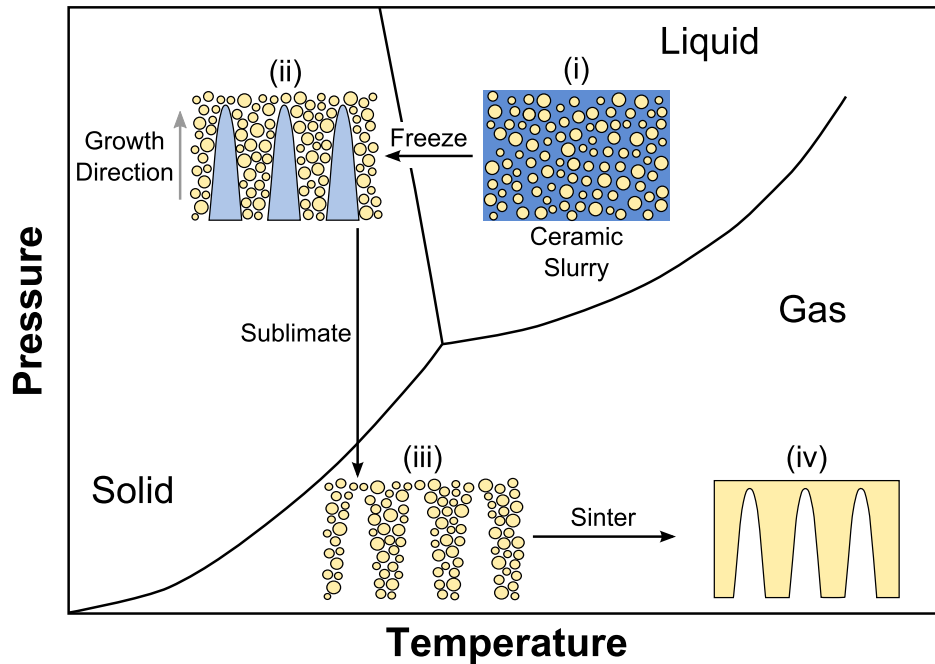


Figure 58: Pressure-temperature phase diagram of water showing the processing route to freeze cast a ceramic foam, adapted from [92].

### 5.3.3 Experimental Setup

To obtain precise control of the solidification rates of the ceramic slurry a custom freeze casting apparatus was built for this work as shown in Figure 59. To provide the cooling, a Peltier (thermoelectric) cooler was employed which produces a cold and hot surface when connected to a DC current. To maintain the cold surface temperature, heat must be removed from the hot side which was accomplished by running water cooled lines. The cooler was connected to an external power supply generally setup in voltage control, although current control is a possible option. The foam making process began by putting the ceramic slurry into a cylindrical teflon mold that was secured to the cold side of the cooler. Heat was removed from the bottom by the Peltier cooler and the solidification rate can be adjusted by varying the input power. Once the slurry was completely frozen

the sublimation step could be started by lowering the pressure above the frozen slurry; to achieve this low pressure the whole setup was housed inside a vacuum chamber. Low pressure was obtained by drawing a vacuum on the whole system. After sublimation was complete, the green body was removed from the mold and sintered.

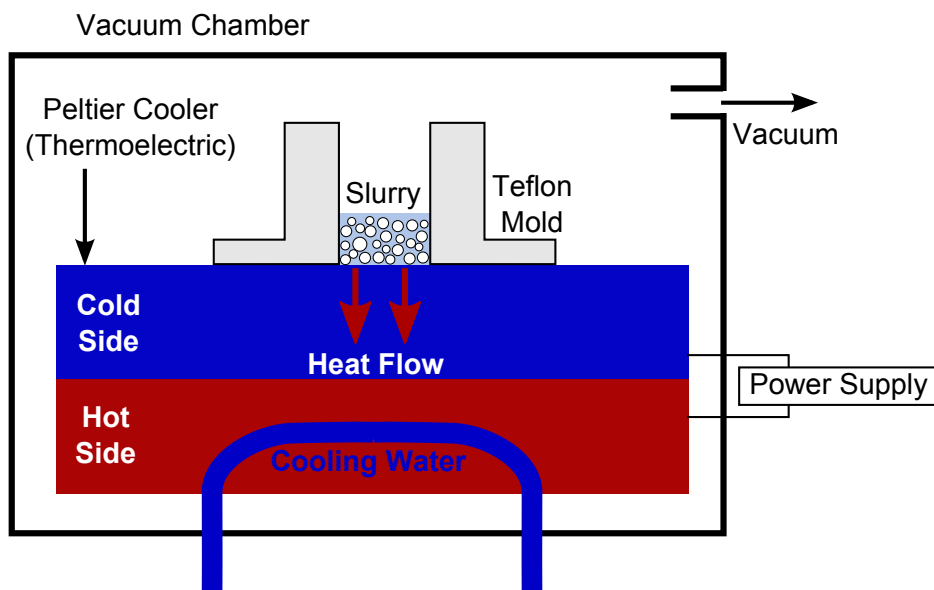


Figure 59: The experimental freeze caster used in this work. The thermoelectric cooler provides controlled cooling rates and the vacuum chamber provides the low pressure necessary for sublimation.

#### 5.3.4 Freeze Cast Zirconia Structures

The freeze casting process produced porous cellular structures like those shown [Figure 60](#). The starting slurry was composed of 14.4 mol% CeO<sub>2</sub>-ZrO<sub>2</sub> commercial nano powders and 2 wt% polyvinyl alcohol mixed with water to achieve a solids loading of 15 vol%. The Peltier cooler cold plate was kept at ~-11.5°C during freezing.

Large open pores can be seen in black in [Figure 60a](#) with the pores having diameters of approximately 10-15 μm. The size of the pores is likely due to the freezing process but a portion can be attributed to shrinkage during sintering. The

strut structure can be seen in the micrograph in [Figure 60b](#) and many of the struts have oligocrystalline structures with grains spanning the whole strut thickness. The sintered grain size was  $\sim 5 \mu\text{m}$  which was consistent with the grain size of bulk ceramics with the same sintering schedule of  $1500^\circ\text{C}$  for 10 hours.

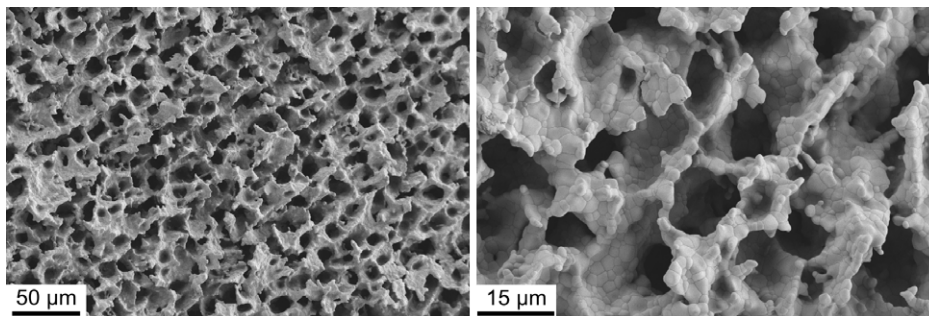


Figure 60: Shape memory ceramic foam produced by freeze casting with a) low magnification image of macro-pore structure showing uniform distribution of  $\sim 10 \mu\text{m}$  pores and b) high magnification image showing near oligocrystalline structure in foam struts, with  $\sim 5 \mu\text{m}$  grains.

### 5.3.5 Thermal Properties of Shape Memory Ceramic Foams

The first shape memory properties measured for the freeze cast foams were the transformation temperatures, determined with differential scanning calorimetry. [Figure 61](#) shows DSC scans for foams made with two different levels of  $\text{CeO}_2$  doping, 5 mol% and 11.7 mol%. In general doping will lower the transformation temperatures and as expected the lower doped sample, 5 mol%  $\text{CeO}_2$ , has higher transformation temperatures, around  $850^\circ\text{C}$  for the martensite to austenite transformation and around  $650^\circ\text{C}$  for the austenite to martensite transformation. The 11 mol%  $\text{CeO}_2$  sample transformed to austenite around  $300^\circ\text{C}$  and transformed back to martensite near  $75^\circ\text{C}$ .

The transformations viewed in the DSC curves were repeatable and this is illustrated in [Figure 61b](#) where the heating-cooling cycle was repeated three times. The curves show a nearly identical overlap indicating the transformations occurred repeatably at the same temperatures.

It is our belief that this is the first time that any type of shape memory transformation has been shown in a ceramic foam. These thermally induced transfor-

mations are very promising indicators for the ability to mechanically induce the transformation which is perhaps more important for practical applications and will be investigated in future work.

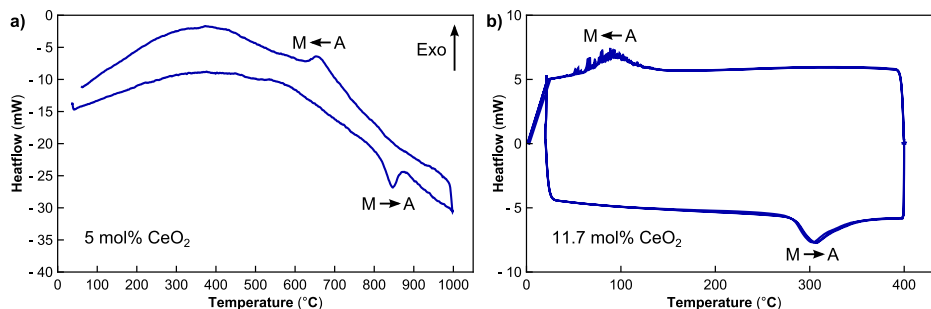


Figure 61: Differential scanning calorimetry curves of freeze-cast shape memory ceramic foams for a) 5 mol %  $\text{CeO}_2\text{-ZrO}_2$  and b) 11.7 mol %  $\text{CeO}_2\text{-ZrO}_2$ .

### 5.3.6 Concluding Thoughts on Foams

In this section we have demonstrated the ability to produce highly ordered zirconia foams produced by freeze casting. The foams were made using a custom built freeze caster equipped with a Peltier cooler to provide a cold surface for directional cooling, and a teflon mold to hold the ceramic slurry, with both of these components housed within a vacuum chamber to allow for reduced pressure sublimation. The critical processing parameters for freeze casting were the solids loading and the freezing rate which was controlled by the power supplied to the Peltier cooler.

The shape memory behavior of the foams was tailored by doping with  $\text{CeO}_2$  with greater amounts of doping lowering the transformation temperatures as measured with differential scanning calorimetry. The DSC results of the foams show clear transformation peaks over a range of temperatures depending on the foam composition. We believe that this is the first time any shape memory properties have been shown in a shape memory ceramic foam. While these results are promising, much more work needs to be done to optimize the foam structure and characterize the foam properties.

## 5.4 THIN FILMS

The final scale-up architecture that will be discussed is a thin film structure. The critical dimension here is the film thickness, which is typically in the nanometer to micrometer range and provides access to free surface to allow for unconstrained transformation. The lateral dimensions can be more or less unrestricted in their extent and a schematic of a simple film and substrate is shown in Figure 62. Most thin films are made with some type of deposition process that progressively builds up the material using a "bottom-up" approach on top of a substrate. Thin films are common in the semiconductor industry and in microelectromechanical systems (MEMS) and therefore there is a broad knowledge base about their processing and properties [96, 97].

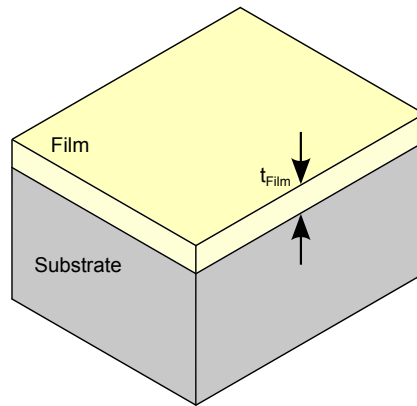


Figure 62: Schematic of a thin film highlighting the film thickness which is the critical dimension.

There have been many investigations into metallic shape memory thin films since they are ideally suited for integration with MEMS systems to provide mechanical motion. Most of the work has focused on Ni-Ti thin films, and it has been shown that the thin films can have the full range of shape memory properties [98, 99, 100, 101]. This indicates that thin films made from shape memory ceramics should also be possible.

In fact, zirconia thin films have also been researched extensively mainly for their potential as a solid electrolytes for fuel cells [102, 103, 104] and for their dielectric properties for use as insulating layers in transistors [105, 106, 107]. The prevailing fabrication method is sputter deposition — a physical vapor deposi-



tion method — using either direct current (DC) or radio frequency alternating current (RF) techniques depending on the target material. For DC sputtering, the targets must be electrically conducting and therefore are typically made of high purity metals. In order for the deposited film to be in the oxidized form a reactive gas must be added, which is typically oxygen [108]. Metallic targets can also be used with RF sputtering [109], although the real advantage of RF sputtering is for oxide targets which require the alternating current to eliminate charging on the non-conductive targets which this can be done with [110] or without [111] reactive oxygen added.

#### 5.4.1 *Production of Zirconia Thin Films*

Here two sputtering methods were used to create thin films of zirconia; both were RF based but the first method used oxide targets and the second used metallic targets. Both were placed in a AJA International sputterer which had an RF frequency of 13.5 MHz and a target to substrate distance of approximately 4 inches.

- *Oxide Targets* — The oxide targets were custom made by mixing zirconium oxide ( $ZrO_2$ ) and cerium oxide ( $CeO_2$ ) powders and mixing thoroughly with polyvinyl alcohol binder (45 g of powders and 5 mL of 4 wt% PVA solution). The mixed powders were pressed into a 3 inch diameter die with 45,000 pounds of force to make a green disk which was sintered at 1500°C for 10 hours. The sintered disk was then cut using a water jet abrasive cutter to a final diameter of 2 inches, which is the required size for the sputtering tool available, and the thickness was  $\sim 1/4$ ". The targets were secured to a copper backing plate using thermally conductive carbon epoxy to ensure proper cooling.

As composition of the final films is critical for determining the transformation temperatures — and therefore the mechanical properties — it is necessary to have careful control of the composition. This was done by altering the ratio of the oxides in the targets during fabrication. This means that each target was customized for a single composition of  $CeO_2$ - $ZrO_2$ .

Argon and oxygen gas were used for the oxide sputtering to ensure the final films were fully oxidized. The total chamber pressure was 3 mT and the

argon to oxygen ratio was 11:1. The target power was varied between 60 W and 200 W with careful attention paid to use slow ramp up and ramp down rates to avoid large thermal gradients that can cause cracking of the targets. Deposition rates were measured using a quartz crystal microbalance and the effect of target power on the deposition rate is shown in Figure 63 for several targets with varying levels of CeO<sub>2</sub>. Higher target power increases the deposition rate for each composition as expected but there is no obvious trend with regards to the target composition.

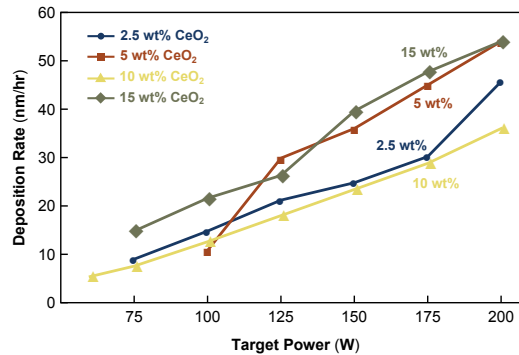


Figure 63: RF sputter deposition rates for zirconium oxide targets with various amounts of CeO<sub>2</sub> doping.

- Metallic Targets* — The metallic targets were zirconium (99.92%) and cerium (99.9%) purchased from AJA international and both were 2" diameter and 1/4" thick. The metallic targets required more oxygen to ensure full oxidation so the argon to oxygen ratio was increased to 10:2 but the total chamber pressure was kept at 3 mT. The deposition rates for each target varied greatly, with cerium sputtering considerably faster, and the effect of target power for both targets is shown in Figure 64a and Figure 64b. There are a few methods to control the final ratio of each oxide in the deposited film but by far the most straightforward and the one used in this work was to vary the power on each target individually; the results of this will be discussed in the next section.
- Substrates* — Nearly any substrate can be used for depositing thin films as long as it can withstand the low pressures found in the vacuum chamber. Typically extremely flat substrates are used because of the small film thick-

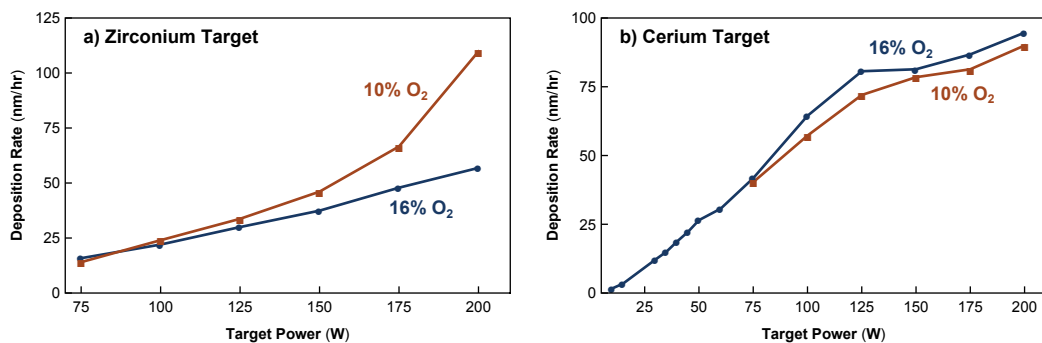


Figure 64: RF sputter deposition rates for a) zirconium and b) cerium targets for different target powers. Two argon to oxygen ratios are shown, 16% O<sub>2</sub> corresponds to an Ar:O<sub>2</sub> flowrate of 10:2 and 10% O<sub>2</sub> is Ar:O<sub>2</sub> of 10.8:1.2.

nesses and a rough surface would not yield a continuous film. In this work a few substrates were used including silicon wafers, metallized silicon wafers, and indium tin oxide transparent substrates. All were thoroughly cleaned before deposition by using a sequence of ultrasonic bath treatments in acetone then isopropyl alcohol with a final rinse in isopropyl and finally drying with nitrogen.

#### 5.4.2 Characterization of Zirconia Thin Films

After deposition the films were first examined using a scanning electron microscope. A film deposited directly onto silicon was cleaved and is shown in [Figure 65a](#) to be ~100 nm thick with good thickness uniformity. A top-down examination of the film, [Figure 65b](#), revealed that the grain size was approximately 25 nm while a cross-section analysis, [Figure 65c](#), showed that most of the grains were columnar and spanned the entire thickness of the film.

In order to determine the phases present in the films, grazing incident x-ray diffraction (GIXD) was performed [112]. GIXD was necessary due to the small volume of material within the film and the technique uses a small constant incident angle, commonly known as  $\omega$ , to increase the amount of irradiated material; for this work  $\omega$  was typically 1° or 2°.

The phases present were either tetragonal or monoclinic and increased doping with ceria leads to greater stabilization of the tetragonal phase. For films made

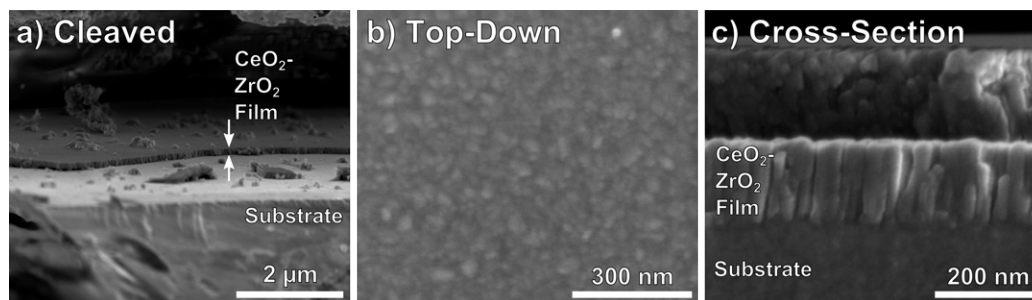


Figure 65: a) View of cleaved film on substrate b) top-down view of a film showing  $\sim 25$  nm grain size and c) cross-section view of film with  $\sim 25$  nm columnar grains.

from oxide targets, [Figure 66](#) shows the GIXD patterns for various  $\text{CeO}_2$  doping levels and films were produced that spanned the range from fully monoclinic at low doping levels to fully tetragonal at high doping levels. This knowledge will allow for the full spectrum of shape memory properties to be manifested such as the shape memory effect and superelasticity.

For the films made from metallic targets, control of the composition and therefore the phase distribution, is achieved by varying the relative deposition rate of each target. [Figure 67](#) shows the effect of varying the power applied to the cerium target while maintaining the zirconium target at a constant power of 200W. As the cerium power is lowered, less ceria is incorporated into the film and as a result the amount of monoclinic phase in the film increases.

Once the relationship between the sputtering process parameters and the final film phase distribution was determined, the next step was to measure the transformation in the thin films. One method to measure the transformation temperatures is [DSC](#), as was done previously for bulk samples, powders, and foams. However, the transformation is difficult to measure in DSC because the film contains such a small amount of material, and the heat flow signals produced by the transformation are likely below the instrument resolution.

The only other method to measure the transformation is to directly measure the phases using XRD, but in order to view the transformation the temperature must be changed during the measurements. In this work GIXD measurements were setup inside of a furnace to measure the transformation in-situ. A typical test collected a 2-theta scan over 40 minutes then the temperature was increased and another scan was collected. [Figure 68](#) shows an example of the in-situ GIXD

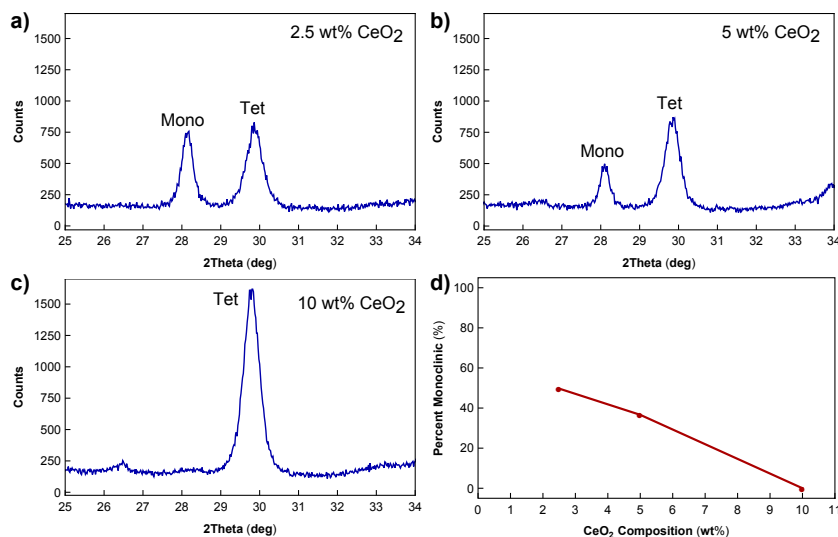


Figure 66: GIXD patterns for films produced from oxide targets with a) 2.5 wt% CeO<sub>2</sub>, b) 5 wt% CeO<sub>2</sub> and, c) 10 wt% CeO<sub>2</sub>. All films were deposited at 500°C at 150W target power for 5 hours. d) The percentage of monoclinic phase vs. composition determined by comparing the relative peak heights.

for a thin film produced with metallic targets. The zirconium target power was 200 W, the cerium target power was 5W, the chamber pressure was 3 mT, the argon to oxygen ratio was 10:2, and the deposition was carried out without any substrate heating. The first scan in [Figure 68](#) was done at 25°C and is shown on the bottom left. The peaks seen at 28.1° and 31.4° are from monoclinic phase indicating that the as-deposited film was 100% monoclinic phase. As the heating progressed there was very little change up to 300°C. At 450°C a new peak was observed at 30.4° and this peak is associated with the tetragonal phase, but monoclinic peaks were also present. This suggests that some of the monoclinic phase transformed into the tetragonal phase and both phases were present in the film. The sample was cooled back down to room temperature and the tetragonal and monoclinic peaks persisted. This indicates that a portion of monoclinic phase transformed to the tetragonal phase but did so irreversibly. Normally it would be expected that the transformation would revert upon cooling but that was not the case here. Stress could be an explanation for the irreversible transformation. It is possible that the as-deposited film had a residual stress that was likely compressive.

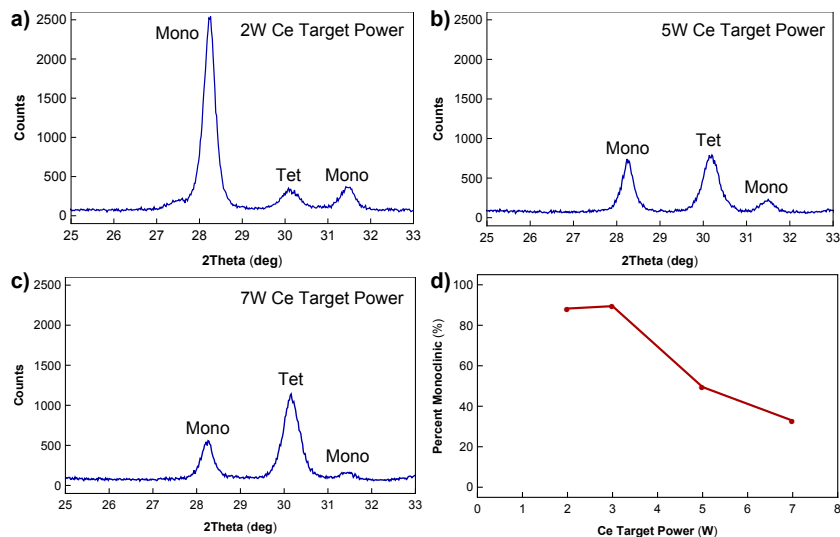


Figure 67: GIXD patterns for films produced from metallic targets with constant Zr power of 200W and a) 2W Ce power, b) 5W Ce power and, c) 7W Ce power. All films were deposited at 500°C 3 hours. d) The percentage of monoclinic phase vs. Ce target power determined by comparing the relative peak heights.

sive. Heating the sample may have alleviated that stress and allowed some of the monoclinic phase to transform to the austenite irreversibly.

Other in-situ GIXD tests were carried out to investigate other ratios of the monoclinic and tetragonal phases in order to look for a reversible transformation, however none were observed. The most likely explanation for this is the small grain size observed in the thin films of ~25 nm. When the grains are this small, it is possible that the transformation is hindered. Small grains are known to retard the transformation by altering the transformation temperatures.

#### 5.4.3 Concluding Thoughts on Thin Films

Thin films can be oligocrystalline structures if they have grains that are columnar and span the entire film thickness. In this form they are expected to have the ability to transform without cracking. The appeal of thin films is their ease of integration with MEMS and shape memory ceramics have the potential to provide mechanical motion in these systems. This work demonstrated that thin films of zirconia can be made via RF magnetron sputtering and that the phases can be con-

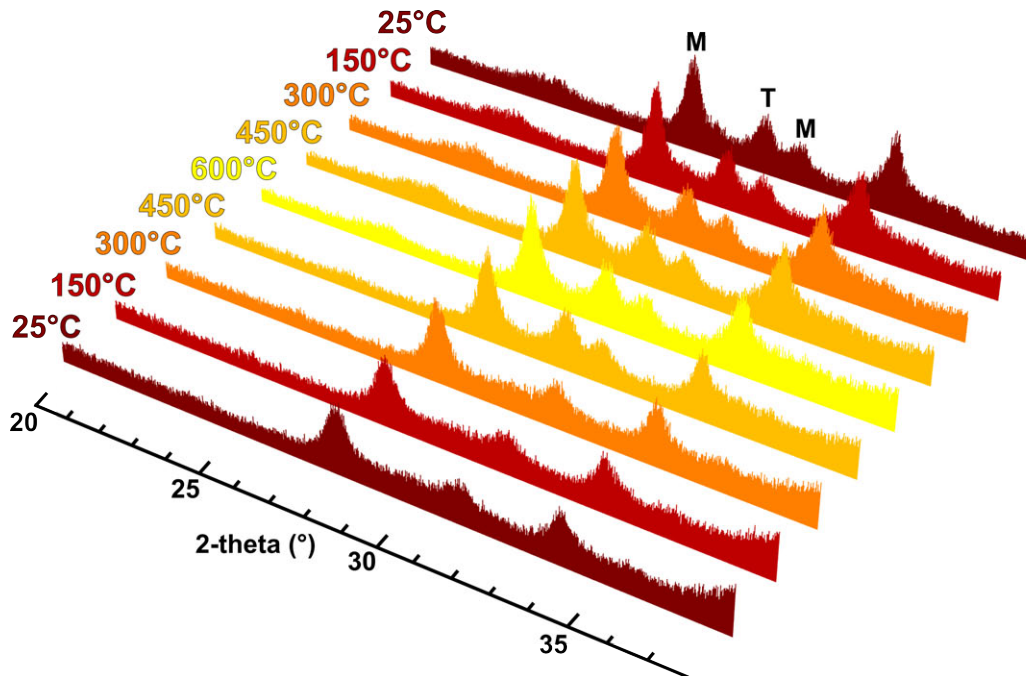


Figure 68: GIXD patterns for thin films measured in a furnace at different temperatures. A peak from the tetragonal phase ( $30.4^\circ$ ) appears at  $450^\circ\text{C}$  but persists upon cooling to room temperature indicating an irreversible transformation.

trolled by doping with ceria. Films were made from mixed oxide targets and from metallic targets with oxygen added to the chamber to ensure complete oxidation.

The films were typically on the order of 100 nm thick with grain size of  $\sim 25$  nm. To investigate their transformation behavior the films were heated in a furnace and the phases were measured simultaneously with GIXD. An irreversible transformation from the monoclinic phase to the tetragonal phase was observed and was attributed to stress-relief in the film. No reversible transformations were observed and this was ascribed to the small grain size of the film. Reversible transformation should be possible and more work needs to be done to adjust the grain size and residual stress in the films.

## 5.5 CONCLUSIONS

This chapter presented the many possible methods to scale-up the promising results that were found with micro-pillars in the previous chapters. Each of the

methods can maintain at least one dimension on the micrometer scale to ensure the improved cycling ability, elevated energy dissipation, and transformation without cracking; be it particle diameter, fiber diameter, foam strut diameter, or thin film thickness. Each has its own set of applications and industries where they can be applied: powders in energy dissipation, fibers for smart fabrics, foams for light-weighting and energy dissipation, and thin films for MEMS and microelectronics, but they are likely not to be limited to any of these and probably will expand to other applications. While each of the structures has known processing routes, work remains to be done to optimize production and link the structure and property relationships for the best shape memory properties.



## CONCLUSIONS AND FUTURE WORK DIRECTIONS

---

Shape memory materials are a class of materials that possess a solid-state martensitic phase transformation which, by definition, results in a shape change. It is this shape change — and the associated energy required to drive the shape change — that make them interesting for engineering applications such as actuation and energy dissipation. However, this shape change can be problematic if it can't be accommodated by the material; this situation typically occurs if the material is brittle. The expansion or contraction of a single grain within the material creates mismatch stresses between neighboring grains, and for brittle materials this frequently leads to fracture along the grain boundaries.

Some ceramics with martensitic phase transformations have been investigated for their shape memory properties, notably zirconia, but the brittle nature of ceramics resulted in severe limitations in the number of transformation cycles that could be achieved in bulk polycrystalline forms, generally permitting less than five cycles. This cycling limitation has greatly restricted the practical applicability of shape memory ceramics. To overcome this, we have applied microstructure engineering techniques to reduce or eliminate grain boundaries and allow free transformation without stress concentrations and the associated fracture. Here we summarize the main conclusions drawn from this work.

### SMALL VOLUME SHAPE MEMORY CERAMICS

The first proof of concept work involved fabricating zirconia single crystalline micro-pillars from a larger bulk polycrystalline specimen. The pillars were compression tested with a semi-blunt nanoindenter tip to examine their shape memory properties. The transformation temperatures were controlled by doping with either ceria or titanium.

Superelasticity was investigated in micron-sized pillars with 15.9 mol% CeO<sub>2</sub> doping in [Section 2.7](#). The pillars were able to sustain 50 reversible superelastic cycles without fracture and many more cycles are expected to be possible. The superelastic behavior showed characteristic displacement plateaus

indicative of a phase transformation, and during each cycle energy was dissipated as seen by the hysteresis in the stress-strain curves.

The shape memory effect was demonstrated in micro-pillars doped with 8 mol% CeO<sub>2</sub> and 0.5 mol% Y<sub>2</sub>O<sub>3</sub> in [Section 2.9](#). The pillars achieved ~7% bending strain and did not show any signs of cracking or fracture. The deformation was recoverable when the pillars were heated to 500°C, completing the shape memory effect cycle. Direct evidence of the phase transformation was obtained by identifying the phases present with electron diffraction on both a bent pillar and a pillar after heating. Nearly all of the shape change was recovered after heating.

The transformation stress and strain observed in the micro-pillars — up to 2.5 GPa and 7% respectively — makes small scale shape memory ceramics attractive for actuator applications. The combination of stress and strain is the energy density, and the micro-pillars tested here have some of the highest energy density of all actuator systems, see [Figure 24](#). Another attractive property of shape memory ceramics is their ability to withstand high temperatures, and they are expected to demonstrate shape memory properties up to ~1100°C which is much higher than most shape memory metals which max out around 500°C, see [Figure 25](#).

*Future Work* — Micro-pillar compression is ideally suited for exploring the underlying physical mechanisms of martensitic transformations. Other shape memory ceramic systems besides zirconia, such as those listed in [Table 2](#), could be explored to extend the concepts discovered here. Since the transformations in other systems are somewhat different, studies could reveal other interesting phenomena in micro-scale shape memory ceramics.

#### OLIGOCRYSTALLINE TO POLYCRYSTALLINE TRANSITION

The work done on single crystal pillars was extended to oligocrystalline pillars — those which contain only a few grains. Pillars with different diameters were made from a bulk specimen with constant grain size to explore the transition from nearly single crystalline to oligocrystalline all the way to polycrystalline. The larger diameter pillars had a greater propensity for cracking as they were more polycrystalline, see [Figure 26](#). This result was expected and served as a useful confirmation of the general idea that more

grain boundaries lead to greater internal grain boundary stresses. The magnitude of the transformation stresses also increased with pillar diameter and this was believed to be due to greater stored elastic energy within larger pillars which acts against the transformation.

*Future Work* — Oligocrystalline structures do not have inherent size scales, but rather are based on the relationship between their grain size and the overall specimen size. So in theory, oligocrystalline structures can be fashioned to any desired size but as of yet there is no guarantee that they will maintain the favorable properties demonstrated here. There is a chance that at some size scale, other sub-grain transformation zones could form that would behave similar to grain boundaries and could lead to internal stresses. Therefore, an interesting extension of this work on the oligocrystalline to polycrystalline transition would be to investigate larger oligocrystalline structures. For example, if a bulk polycrystalline sample was prepared with a larger grain size, then larger oligocrystals could be made. These could be used to determine the maximum specimen size that would exhibit the improved transformation cycling properties that have been demonstrated here.

#### CRYSTAL ORIENTATION DEPENDENCE

When dealing with single crystals and oligocrystals, very few crystal grains are present and as a result the crystal anisotropy becomes a much greater factor in determining the overall properties. So to properly design these structures, one must know their properties as a function of crystal orientation. In [Chapter 4](#), single crystal micro-pillars — 43 in total — with fixed geometry were fabricated with different crystal orientations spanning most of orientation space to determine the orientation dependencies.

The properties investigated included the transformation stress, transformation strain, fracture behavior, and the elastic modulus. The transformation was found to occur along only one transformation correspondence between the tetragonal phase to the monoclinic phase, specifically correspondence C, which had the highest correlation between the measured stress and the Schmid factor as shown in [Figure 40](#). The Schmid factor was also highly predictive of the fracture response with three behavior zones emerging from the analysis. When the Schmid factor was greater than 0.3, all the pillars

transformed, but when the Schmid factor was less than 0.1 the pillars fractured or showed signs of crystal slip. A mixed zone was found where either transformation or fracture was observed to occur, for pillars with intermediate Schmid factors between 0.1 and 0.3, indicating competing mechanisms of transformation and fracture.

The crystallographic theory of the transformation was used to calculate the expected transformation strain and elastic modulus and the results showed decent correlation with the measured values, see [Figure 46](#) and [Figure 37](#) respectively.

The orientation property maps produced here should be useful for future design and optimization of shape memory zirconia. The maps will be especially critical for design of single crystalline and oligocrystalline structures.

*Future Work* — The experimental framework developed here for probing orientation space should be useful for mapping other orientation dependent properties. Specifically, the energy absorbing properties of small-scale zirconia would be interesting for further work. As the sample size decreases, free surfaces become more prominent and this can increase the energy required to move the transformation front therefore increasing the energy dissipation potential of these materials.

#### ORIENTATION DEPENDENT SIZE EFFECTS

One unexpected outcome of this research was the discovery of a potential combined orientation and size effect. Two sets of pillars were made with different diameters but two different crystal orientations. [Figure 44](#) shows that the dependence of the transformation stress on pillar diameter is different for each orientation. This could provide yet another control knob for optimizing the properties of these small scale zirconia.

*Future Work* — The orientation dependent size effect shown here was based on data from only three or four pillars for each orientation. To truly confirm the effect is indeed real, more pillars should be fabricated to ensure statistical significance. Additionally, other crystal orientations should be inspected to analyze and compare their size effects.

#### POWDER SCALE UP

Individual micron-sized particles of zirconia were compression tested to

show that they could undergo the transformation and it was shown they were able to withstand at least 500 superelastic cycles as seen in [Figure 49](#). This demonstration meant that large collections of particles could be assembled together as a means of producing a macro scale object, an encapsulated powder. Zirconia powders were compression tested to demonstrate the capability of both de-twinning martensite and stress inducing the transformation in [Section 5.1.2](#). These promising results are the first steps towards making an encapsulated powder that could find applications in energy dissipation.

*Future Work* — Now that it was shown that it's possible to drive the transformation in shape memory zirconia powders, more work is needed on determining the properties of these powders. This includes quantifying the energy absorption, transformation stresses, and cycling lifetimes. More work is also needed on finding the ideal encapsulation materials and processing.

#### WIRE SCALE UP

Electrospinning was used to make micron-scale shape memory zirconia wires in [Section 5.2](#). The process parameters of the electrospinning process were examined to make uniform wires. Annealing treatments were performed to increase the grain size which resulted in wires with near oligocrystalline structures.

*Future Work* — Annealing treatments at higher temperatures should be done to improve the oligocrystalline structure. The mechanical properties of the wires need to be explored to show they can go through the transformation many times. The most exciting prospect of the wire structures is that they are amenable to tension testing. Along with the energy absorption mechanism of the phase transformation, this could produce a ceramic material that is strong in tension, something that has many interesting applications. Furthermore, wires can be made into sheets and fabric as another scale up architecture.

## FOAM SCALE UP

A freeze casting process was employed to make ceramic foams with semi-uniform oligocrystalline structures in [Section 5.3.1](#). The foams offer another pathway to scale up that maintains the oligocrystalline structure in the struts of the foam — where few grains are found — and the transformation can proceed without constraint due to the porosity. Preliminary shape memory behavior was shown by measuring the transformation temperatures via differential scanning calorimetry.

*Future Work* — To improve upon the structure of the foam, more tests need to be done to optimize the freeze-casting process parameters such as the cooling rate and the solids loading ratio of the ceramic slurry. This can be done in conjunction with compression testing of the foams to determine the range of their mechanical properties. Other work could include characterizing the heat transfer properties, since foams are often used for their impressive thermal insulation properties.

## THIN FILM SCALE UP

The final scale up method that was investigated was thin films in [Section 5.4](#). These were made via sputter deposition using either oxide and metallic targets. Uniform films were produced with thicknesses on the order of 100 nm. Characterization revealed that the films had columnar grains with diameters of about 25 nm that spanned the full thickness of the film resulting in an oligocrystalline structure. Further characterization mapped the relationship between sputtering parameters and the phases present, which is necessary information for utilizing the shape memory properties. In-situ GIXD measurements were done to observe the transformation, however only an irreversible transformation was seen upon heating, which was likely due to stress relief in the film.

*Future Work* — Thin films of shape memory zirconia are attractive because they should be able to be integrated in micro-electro-mechanical devices with the actuation properties of shape memory zirconia being the most interesting. This will require further work on determining the conditions necessary to drive the transformation via heating or other means.

The overall theme of this thesis is that microstructure engineering techniques can be applied to eliminate the brittle intergranular fracture commonly seen in ceramic shape memory materials. The resulting oligocrystalline structures all maintain one dimension that is physically unconstrained by having access to a free surface. The work began with micro-pillars to prove the concepts and was extended to macro-scale structures such as powders, wires, foams, and thin films. All of the work showed that robust, repeatable shape memory behavior is possible in ceramics when the microstructure is properly controlled. This opens the door to accessing the attractive characteristics of ceramics such as their high strength and refractory properties for their future development in technical applications.





# A

## APPENDIX A

---

### A.1 CERAMIC POWDER PROCESSING

- Mix metals salts ( $\text{ZrOCl}_2 \cdot 8\text{H}_2\text{O}$  and  $\text{Ce}(\text{NO}_3)_3 \cdot 6\text{H}_2\text{O}$ ) in desired ratio into 200 mL of deionized water. The total mass of both salts should be approximately 10 g.
- Mix salts on a stir plate with magnetic stirrer for 10 minutes.
- Prepare 500 mL of 25 vol% ammonium hydroxide solution. 125 mL of  $\text{NH}_4\text{OH}$  in 375 mL of deionized water.
- After salt solution is finished mixing, transfer salt solution into a buret and place 25 vol% ammonium hydroxide solution below the buret on a stir plate. Vigorously stir the ammonium hydroxide solution.
- Slowly drip the salt solution into the ammonium hydroxide solution as it is being stirred.
- After all the salt solution has passed through the buret continue stirring the solution for 10 minutes.
- Centrifuge the precipitated powder solution to separate the solids and liquids, decant off the liquid.
- After decanting add more deionized water to rinse, repeat centrifuging and decanting 3 times.
- Repeat rinsing, centrifuging, and decanting with ethanol to remove water, rinse 3 times.
- After last ethanol rinse, place the powder and liquid in glass beaker and dry at 60-70°C.

- Once powder is dry, grind with mortar and pestle to break up agglomerates that form during drying.
- Calcine powder at 350°C for 2 hours with a ramp rate of 8°C/min.

## A.2 FOCUSED ION BEAM MILLING OF MICRO-PILLARS

The general procedure for top-down milling of micro-pillars beings by milling the trench around the pillar with a high ion current. This is followed by successive milling with lower currents as the final pillar dimensions are approached to reduce ion beam damage and ion implantation. In order to ensure that only a single grain was milled an additional grain marking step was also carried out where a thin annulus was milled around the edges of grain; the marking annulus was used as a centering point for the following steps. All ion milling steps were done with an annular milling geometry and the depth setting set to silicon. Note that these are just rough guidelines and producing well shaped pillars may require slight adjustments to this procedure, especially in the final steps. This work used an FEI Helios Nanolab 600 Dual Beam system with an ion accelerating voltage of 30 kV.

Table 14: FIB milling procedure to fabricate micro-pillars.

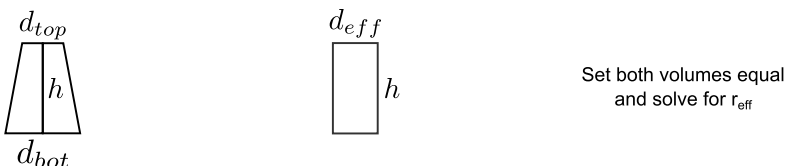
STEP	$d_{\text{outer}}$ ( $\mu\text{m}$ )	$d_{\text{inner}}$ ( $\mu\text{m}$ )	FIB CURRENT	DEPTH SETTING ( $\mu\text{m}$ )	TIME (MIN)
Marking	6	5	93 pA	0.1	1:01
Trench	40	20	6.5 nA	0.5 (2x)	8:03
Trench	22	8	2.8 nA	0.5 (2x)	6:38
Pillar	9	3	0.46 pA	0.5 (2x)	7:45
Pillar	3	1.5	0.93 pA	0.3 (2x)	2:50
Pillar	2	1.2	0.93 pA	0.1	0:36

A.3 NANOINDENTATION MICRO-COMPRESSION

The micro-compression tests in this work were carried out using a Hysitron nanomechanical test platform equipped with a 20  $\mu\text{m}$  diameter conospherical diamond tip. A conospherical tip was used in place of a flat punch because it still allowed scanning probe microscopy to "image" the sample surface. This was important for located and centering the tip above the pillar and also useful for determining if a pillar was broken. The large diameter of the tip minimized indentation of the top of the pillar as can be seen in the geometry of the pillar and tip in [Figure 16](#).

Compression was carried out using open-loop control because the phase transformation occurs too quickly for the feedback in load or displacement control. Loading rates varied, but were typically between 50-300  $\mu\text{N/s}$ . Since the load necessary to initiate the transformation was often unknown, the peak loads were slowly increased until a transformation plateau was observed.

One undesirable side effect of top down FIB milling is the resulting pillar taper. This causes the top and bottom diameter of the pillar to differ and this becomes important when converting from loads to stresses. To account for this we employed an "effective diameter" that incorporates the pillar taper. [Figure 69](#) shows the concept used for the effective diameter calculations which equates the volume of the tapered pillar to the volume of an ideal non-tapered pillar with an unknown diameter to be solved for. This method is used because it will lead to the same calculated energy dissipated when using the area within the load-displacement curve divided by the actual pillar volume and when using the area within the stress-strain curve.



$$V = \frac{\pi h}{3} [r_{top}^2 + r_{top}r_{bot} + r_{bot}^2] \quad V = \pi r_{eff}^2 h \quad d_{eff} = \sqrt{\frac{1}{3} [d_{top}^2 + d_{top}d_{bot} + d_{bot}^2]}$$

Figure 69: Calculation of the pillar effective diameter which is used to account for pillar taper.

## A.4 SUPERELASTIC MICRO-COMPRESSION STRESS-STRAIN CURVES

In [Section 2.7](#) the superelastic properties of one pillar were presented (Pillar A). Six more pillars were fabricated and superelastic micro-compression tests were carried out to varying numbers of cycles. [Table 15](#) gives the geometric properties of the pillars as well as the number of superelastic cycles achieved and the average loss factor (see [Equation 2](#)) of all the superelastic cycles. None of these pillars showed any signs of cracking after superelastic cycling. A selection of stress-strain curves are shown in [Figure 70](#) - [Figure 76](#).

Table 15: Pillar data for superelastic curves collected in this work.  $\eta$  is the loss factor.

PILLAR ID	mol% CeO <sub>2</sub>	d <sub>top</sub> (μm)	d <sub>bot</sub> (μm)	HEIGHT (μm)	d <sub>eff</sub> (μm)	TAPER ANGLE	NO. OF CYCLES	$\eta$
A	16	1.0	1.4	3.2	1.2	3.3	27	0.14
B	16	1.5	2.1	4.4	1.8	3.8	5	0.15
C	16	1.0	1.4	3.7	1.2	2.9	7	0.14
D	16	1.1	1.6	4.1	1.4	3.1	13	0.14
E	16	1.3	1.7	3.9	1.5	3.1	9	0.12
F	16	1.5	2.0	4.3	1.7	3.4	13	0.14
G	17	0.9	1.4	4.4	1.1	3.5	53	0.08

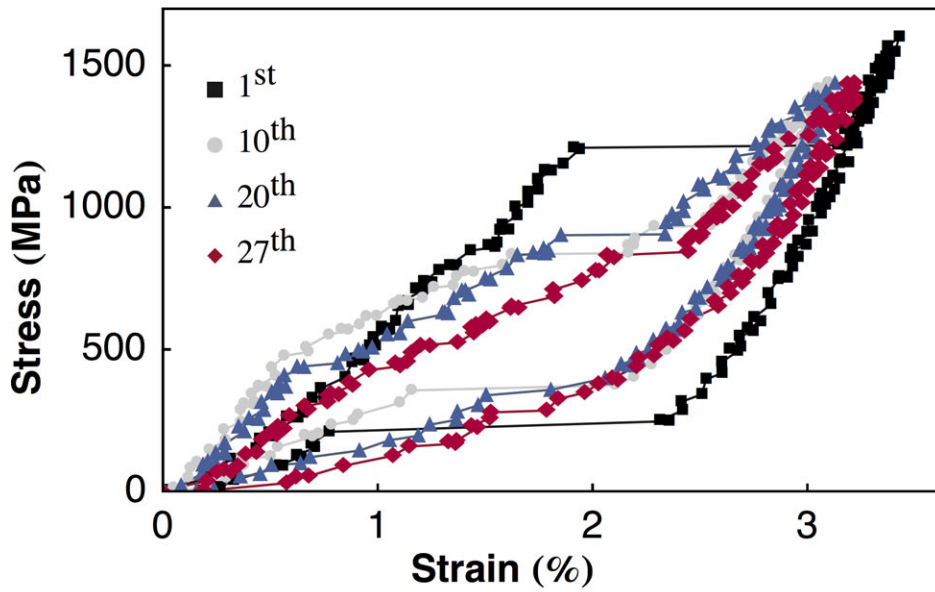


Figure 70: Superelastic stress-strain curves for pillar A, cycled 27 times, with  $d_{\text{eff}} = 1.2 \mu\text{m}$ .

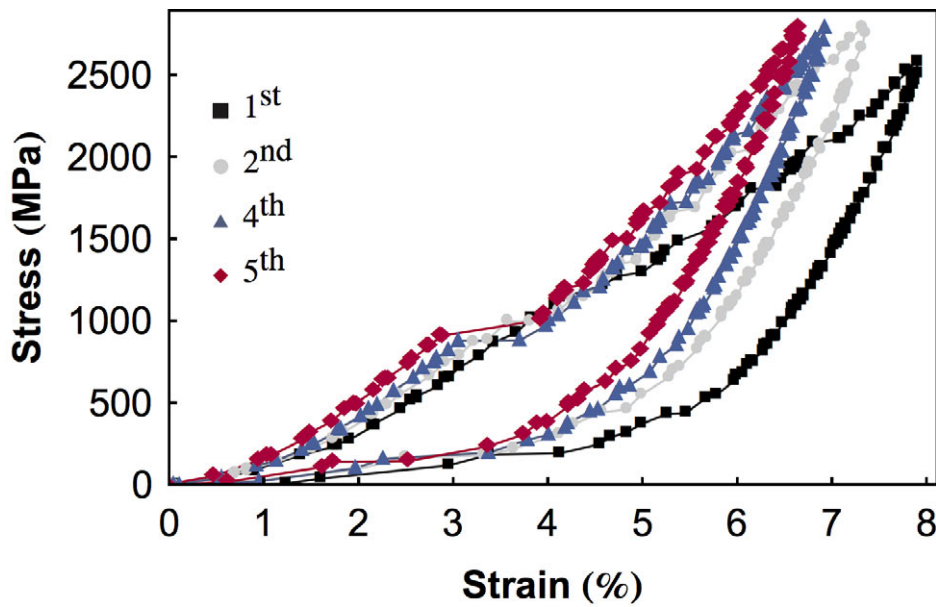


Figure 71: Superelastic stress-strain curves for pillar B, cycled five times, with  $d_{\text{eff}} = 1.8 \mu\text{m}$ .

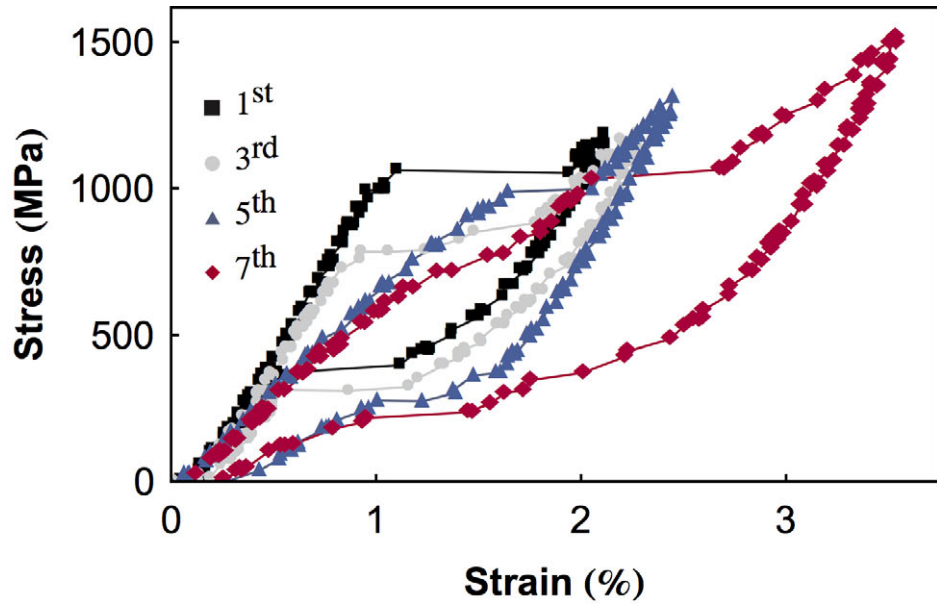


Figure 72: Superelastic stress-strain curves for pillar C, cycled seven times, with  $d_{\text{eff}} = 1.2 \mu\text{m}$ .

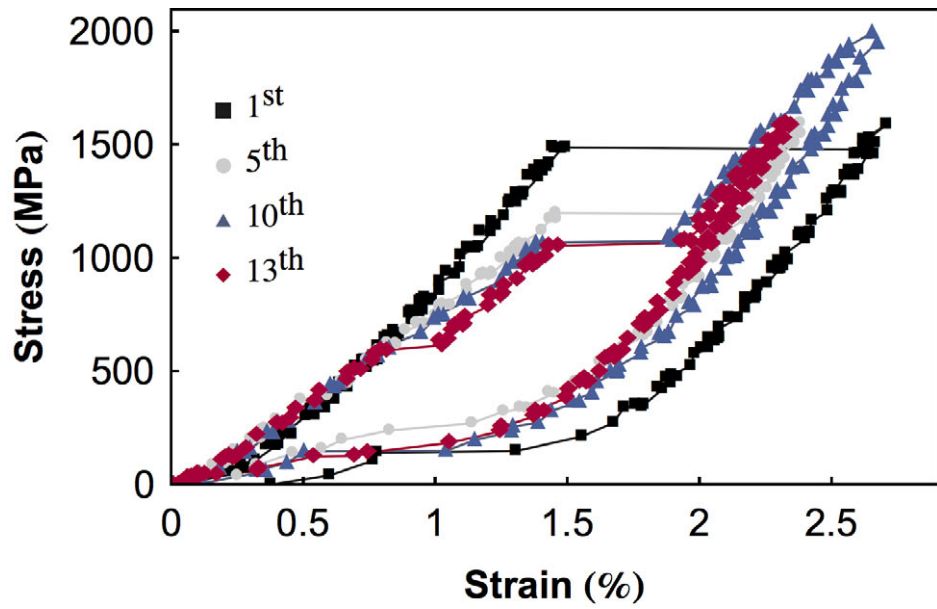


Figure 73: Superelastic stress-strain curves for pillar D, cycled 13 times, with  $d_{\text{eff}} = 1.4 \mu\text{m}$ .

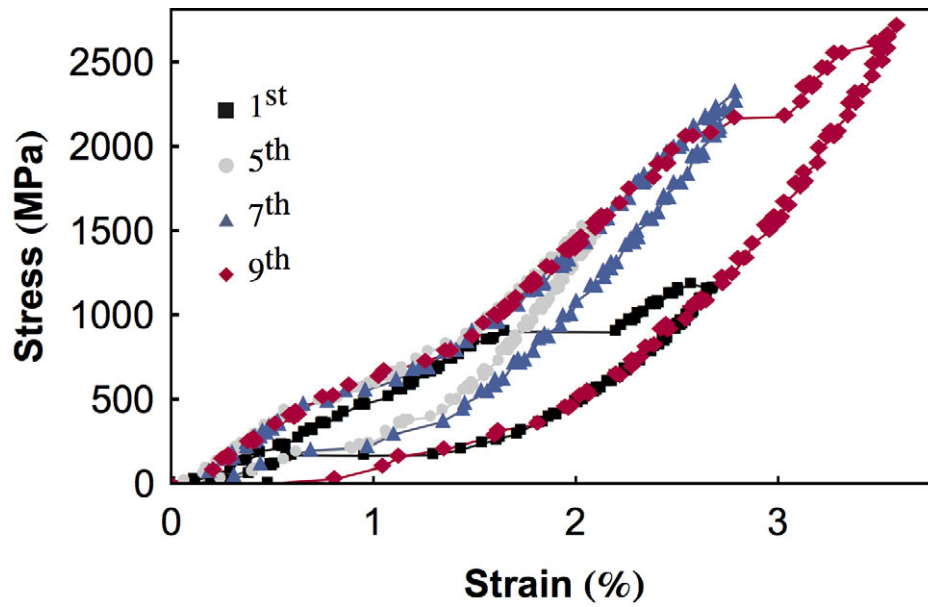


Figure 74: Superelastic stress-strain curves for pillar E, cycled nine times, with  $d_{\text{eff}} = 1.5 \mu\text{m}$ .

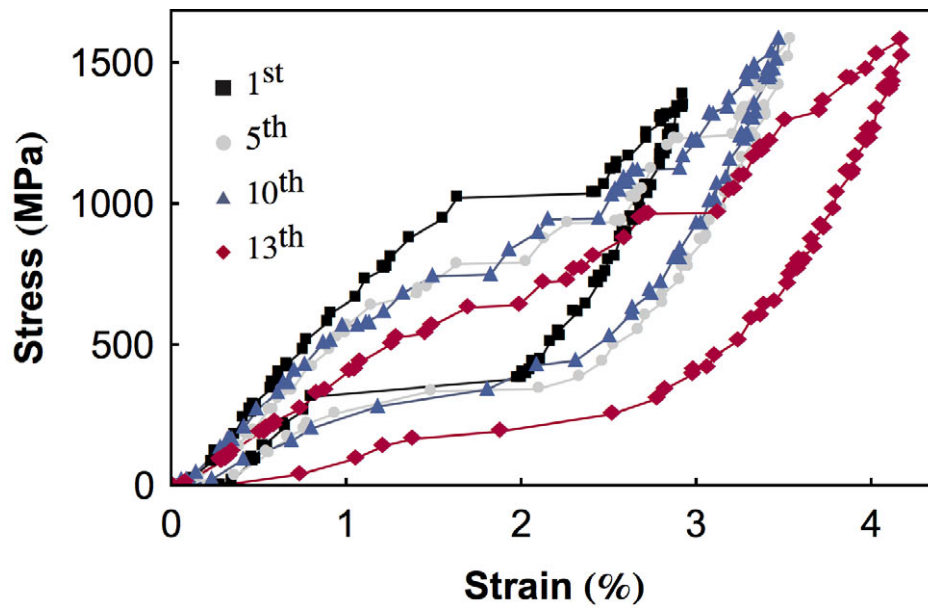


Figure 75: Superelastic stress-strain curves for pillar F, cycled 13 times, with  $d_{\text{eff}} = 1.7 \mu\text{m}$ .

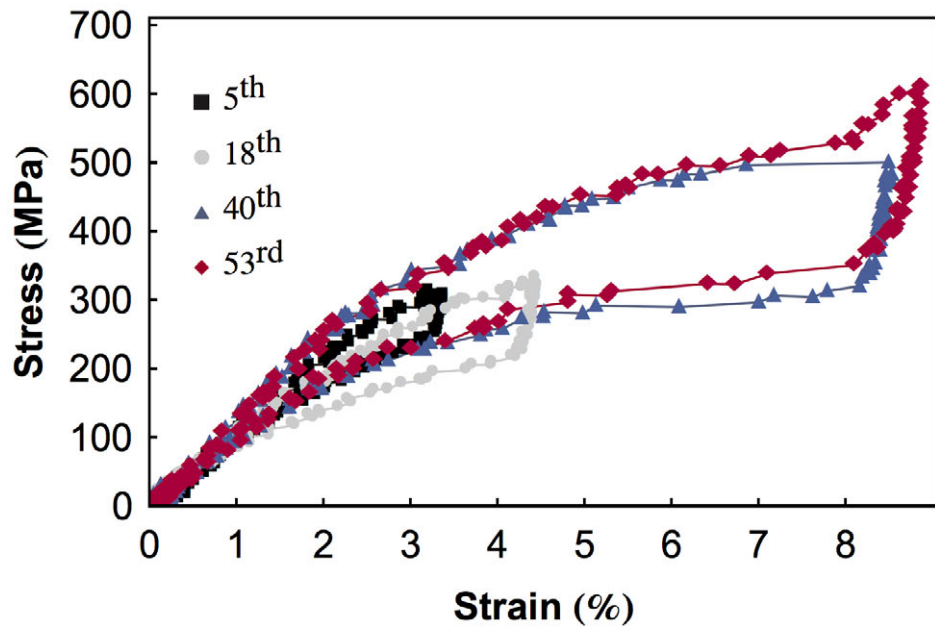


Figure 76: Superelastic stress-strain curves for pillar G, cycled 53 times, with  $d_{\text{eff}} = 1.1 \mu\text{m}$ .



## BIBLIOGRAPHY

---

- [1] K. Otsuka and C. Wayman. *Shape Memory Materials*. Cambridge University Press, 1998.
- [2] H. Horikawa, S. Ichinose, K. Morii, S. Miyazaki, and K. Otsuka. Orientation Dependence of B-B' Stress-Induced Martensitic Transformation in a Cu-Al-Ni Alloy. *Metallurgical Transactions*, 19(April):915–923, 1988.
- [3] P. Wollants, M. Bonte, and J. Roos. A Thermodynamic Analysis of the Stress Induced Martensitic Transformation in a Single Crystal. *Zeitschrift für Metallkunde*, 70:113–117, 1979.
- [4] L. Chang and T. Read. Plastic Deformation and Diffusionless Phase Changes in Metals - The Gold-Cadmium Beta Phase. *Journal of Metals*, 189:47–52, 1951.
- [5] A. Olander. The crystal structure of AuCd. *Zeitschrift für Kristallographie*, 83(1/2):145–148, 1932. ISSN 0044-2968.
- [6] C. Benedicks. On the Elasticity of Solid Solutions, in Particular Those of AuCd. *Arkiv för Matematik, Astronomi och Fysik*, 27A(18):1–11, 1940.
- [7] W. Buehler, J. Gilfrich, and R. Wiley. Effect of Low Temperature Phase Changes on the Mechanical Properties of Alloys near Composition TiNi. *Journal of Applied Physics*, 34(5):1391–1573, 1963.
- [8] T. Tadaki, K. Otsuka, and K. Shimizu. Shape memory alloys. *Annual Review of Materials Science*, 18:25–45, dec 1998.
- [9] K. Otsuka and K. Shimizu. Pseudoelasticity and shape memory effects in alloys. *International Materials Reviews*, 31(1):93–114, 1986. ISSN 09506608.
- [10] B. Fatiha, E. Feninat, G. Laroche, M. Fiset, and D. Mantovani. Shape Memory Materials for Biomedical Applications. *Advanced Engineering Materials*, (3):91–104, 2002.
- [11] Y. Chen and C. A. Schuh. Size effects in shape memory alloy microwires. *Acta Materialia*, 59(2):537–553, jan 2011. ISSN 13596454.
- [12] P. E. Reyes-Morel, J.-S. Cherng, and I. W. Chen. Transformation Plasticity of CeO<sub>2</sub>-Stabilized Tetragonal Zirconia Polycrystals: II, Pseudoelasticity and Shape Memory Effect. *Journal of the American Ceramic Society*, 71(8):648–657, aug 1988. ISSN 0002-7820.
- [13] D. C. Dunand and P. Müllner. Size effects on magnetic actuation in Ni-Mn-Ga shape-memory alloys. *Advanced Materials*, 23(2):216–232, 2011. ISSN 09359648.
- [14] H. Das and F. Spit. The measurement of the diffusion of phosphorus in oligo-crystalline silicon with <sup>32</sup>P as radiotracer. A comparison of solid and liquid scintillation counting. *Journal of Radioanalytical and Nuclear Chemistry*, 117:171–182, 1987.
- [15] Z. Zhao, M. Ramesh, D. Raabe, A. M. Cuitino, and R. Radovitzky. Investigation of three-dimensional aspects of grain-scale plastic surface deformation of an aluminum oligocrystal. *International Journal of Plasticity*, 24(12):2278–2297, 2008. ISSN 07496419.
- [16] S. M. Ueland, Y. Chen, and C. A. Schuh. Oligocrystalline Shape Memory Alloys. *Advanced Functional Materials*, 22(10):2094–2099, may 2012. ISSN 1616301X.

## BIBLIOGRAPHY

- [17] J. San Juan, M. L. Nó, and C. A. Schuh. Superelasticity and Shape Memory in Micro- and Nanometer-scale Pillars. *Advanced Materials*, 20(2):272–278, jan 2008. ISSN 09359648.
- [18] D. W. Norwich and A. Fasching. A Study of the Effect of Diameter on the Fatigue Properties of NiTi Wire. In *International Conference on Shape Memory and Superelastic Technologies*, pages 558–562, Stresa, Italy, 2008.
- [19] S. Kirby and L. Stern. Experimental dynamic metamorphism of mineral single crystals. *Journal of Structural Geology*, 15(9-10):1223–1240, sep 1993. ISSN 01918141.
- [20] R. Hannink, P. Kelly, and B. Muddle. Transformation Toughening in Zirconia-Containing Ceramics. *Journal of the American Ceramic Society*, 83(3):461–487, 2000. ISSN 1551-2916.
- [21] D. Green, R. Hannink, and M. Swain. *Transformation Toughening of Ceramics*. CRC Press, Boca Raton, 1989.
- [22] J. Chevalier, L. Gremillard, A. V. Virkar, and D. R. Clarke. The tetragonal-monoclinic transformation in zirconia: Lessons learned and future trends. *Journal of the American Ceramic Society*, 92(26208):1901–1920, 2009. ISSN 00027820.
- [23] J.-G. Duh, H.-T. Dai, and W.-Y. Hsu. Synthesis and sintering behaviour in CeO<sub>2</sub>-ZrO<sub>2</sub> ceramics. *Journal of Materials Science*, 23(8):2786–2791, aug 1988. ISSN 0022-2461.
- [24] E. N. S. Muccillo. Synthesis and characterization of submicron zirconia -12 mol% ceria ceramics. *Ceramics International*, 25(4):345–351, may 1999. ISSN 02728842.
- [25] M. Yashima, T. Hirose, S. Katano, Y. Suzuki, M. Kakihana, and M. Yoshimura. Structural changes of ZrO<sub>2</sub>-CeO<sub>2</sub> solid solutions around the monoclinic-tetragonal phase boundary. *Physical Review B*, 51(13):8018, 1995.
- [26] P. Aldebert and J. Traverse. Structure and ionic mobility of zirconia at high temperature. *Journal of the American Ceramic Society*, 68(1):34–40, 2006. ISSN 1551-2916.
- [27] R. Garvie, R. Hannink, and R. Pascoe. Ceramic Steel? *Nature*, 258:703–704, 1975.
- [28] R. Garvie and P. Nicholson. Structure and Thermomechanical Properties of Partially Stabilized Zirconia in the CaO-ZrO<sub>2</sub> System. *Journal of the American Ceramic Society*, 55(3):152–157, 1972.
- [29] M. Yashima, T. Mitsuhashi, H. Takashina, M. Kakihana, T. Ikegami, and M. Yoshimura. Tetragonal-Monoclinic Phase Transition Enthalpy and Temperature of ZrO<sub>2</sub>-CeO<sub>2</sub> Solid Solutions. *Journal of the American Ceramic Society*, 78(8):2225–2228, 1995.
- [30] G. Hugo, B. Muddle, and R. Hannink. Crystallography of the Tetragonal to Monoclinic Transformation in Ceria-Zirconia. In *Materials Science Forum*, volume 34, pages 165–169. Trans Tech Publ, 1991.
- [31] T. S. Sheu, T. Y. Tien, and I. W. Chen. Cubic-to-Tetragonal ( $t'$ ) Transformation in Zirconia-Containing Systems. *Journal of the American Ceramic Society*, 75(5):1108–1116, may 1992. ISSN 0002-7820.
- [32] S. Muqtader and B. Rao. Structural changes and mechanical properties of CeO<sub>2</sub>-doped tetragonal zirconia polycrystals. *Journal of Materials Science Letters*, 9:1075–1076, 1990.
- [33] A. Lai, Z. Du, C. L. Gan, and C. A. Schuh. Shape Memory and Superelastic Ceramics at Small Scales. *Science*, 341(6153):1505–1508, sep 2013. ISSN 0036-8075.
- [34] M. Uchic, D. Dimiduk, J. Florando, and W. D. Nix. Sample Dimensions Influence Strength and Crystal Plasticity. *Science*, 305:986–989, jul 2004.

- [35] M. D. Uchic and D. M. Dimiduk. A methodology to investigate size scale effects in crystalline plasticity using uniaxial compression testing. *Materials Science and Engineering: A*, 400-401: 268–278, jul 2005. ISSN 09215093.
- [36] D. Dimiduk, M. Uchic, and T. Parthasarathy. Size-affected single-slip behavior of pure nickel microcrystals. *Acta Materialia*, 53(15):4065–4077, sep 2005. ISSN 13596454.
- [37] H. Zhang, B. B. Schuster, Q. Wei, and K. K. Ramesh. The design of accurate micro-compression experiments. *Scripta Materialia*, 54(January):181–186, jan 2006. ISSN 13596462.
- [38] C. J. Lee, J. C. Huang, and T. G. Nieh. Sample size effect and microcompression of Mg65Cu25Gd10 metallic glass. *Applied Physics Letters*, 91(16):161913, 2007. ISSN 00036951.
- [39] L. Han, L. Wang, J. Song, M. C. Boyce, and C. Ortiz. Direct quantification of the mechanical anisotropy and fracture of an individual exoskeleton layer via uniaxial compression of micropillars. *Nano Letters*, 11(9):3868–74, sep 2011. ISSN 1530-6992.
- [40] J. San Juan, M. L. N6, and C. A. Schuh. Nanoscale shape-memory alloys for ultrahigh mechanical damping. *Nature Nanotechnology*, 4(7):415–419, 2009.
- [41] J. San Juan, M. L. N6, and C. A. Schuh. Superelastic cycling of Cu-Al-Ni shape memory alloy micropillars. *Acta Materialia*, 60(10):4093–4106, jun 2012. ISSN 13596454.
- [42] Z. Du, X. M. Zeng, Q. Liu, A. Lai, S. Amini, A. Miserez, C. A. Schuh, and C. L. Gan. Size effects and shape memory properties in ZrO2 ceramic micro- and nano-pillars. *Scripta Materialia*, 101:40–43, 2015. ISSN 13596462.
- [43] A. Runciman, D. Xu, A. R. Pelton, and R. O. Ritchie. An equivalent strain/Coffin-Manson approach to multiaxial fatigue and life prediction in superelastic Nitinol medical devices. *Biomaterials*, 32(22):4987–93, aug 2011. ISSN 1878-5905.
- [44] J. Huber and N. Fleck. The selection of mechanical actuators based on performance indices. *Proc. R. Soc. Lond. A*, 453:2185–2205, 1997.
- [45] Y. Ma, C. Jiang, Y. Li, H. Xu, C. Wang, and X. Liu. Study of Ni50+xMn25Ga25-x ( $x = 2-11$ ) as high-temperature shape-memory alloys. *Acta Materialia*, 55(5):1533–1541, 2007. ISSN 13596454.
- [46] D. Lagoudas. *Shape Memory Alloys Modeling and Engineering Applications*. Springer, New York, 2008.
- [47] M. D. Uchic, P. A. Shade, and D. M. Dimiduk. Plasticity of Micrometer-Scale Single Crystals in Compression. *Annual Review of Materials Research*, 39(1):361–386, 2009. ISSN 1531-7331.
- [48] J. San Juan and M. N6. Superelasticity and shape memory at nano-scale: Size effects on the martensitic transformation. *Journal of Alloys and Compounds*, 577:S25–S29, nov 2013. ISSN 09258388.
- [49] N. Ozdemir, I. Karaman, and N. Mara. Size effects in the superelastic response of Ni54Fe19Ga27 shape memory alloy pillars with a two stage martensitic transformation. *Acta Materialia*, 60:5670–5685, 2012.
- [50] S. Miyazaki, S. Kimura, and K. Otsuka. Shape-memory effect and pseudoelasticity associated with the R-phase transition in Ti-50.5 at.% Ni single crystals. *Philosophical Magazine A*, 57(3): 467–478, 1988. ISSN 0141-8610.
- [51] X. Zeng, A. Lai, C. L. Gan, and C. A. Schuh. Crystal Orientation Dependence of Stress-Induced Martensitic Transformation in Shape Memory Zirconia. *Manuscript submitted for*

- publication, 2016.
- [52] J. F. Nye. *Physical Properties of Crystals, Their Representation by Tensors and Matrices*. Clarendon Press, Oxford, 1957.
- [53] E. H. Kisi and C. J. Howard. Elastic Constants of Tetragonal Zirconia Measured by a New Powder Diffractino Technique. *Journal of the American Ceramic Society*, 81(6):1401–1403, 1998.
- [54] H. Fei, A. Abraham, N. Chawla, and H. Jiang. Evaluation of Micro-Pillar Compression Tests for Accurate Determination of Elastic-Plastic Constitutive Relations. *Journal of Applied Mechanics*, 79(6):061011, 2012. ISSN 00218936.
- [55] P. Kelly and L. Rose. The martensitic transformation in ceramics - its role in transformation toughening. *Progress in Materials Science*, 47(5):463–557, 2002. ISSN 00796425.
- [56] N. Simha. Twin and habit plane microstructures due to the tetragonal to monoclinic transformation of zirconia. *Journal of the Mechanics and Physics of Solids*, 45(2):261–263, feb 1997. ISSN 00225096.
- [57] A. H. Heuer and L. W. Hobbs. *Science and Technology of Zirconia*. The American Ceramic Society, Columbus, Ohio, 1981.
- [58] F. Lange. Transformation toughening Part 1 Size effects associated with the thermodynamics of constrained transformations. *Journal of Materials Science*, 17:225–234, 1982.
- [59] P. F. Becher and M. Swain. Grain Size Dependent Transformation Behavior in Polycrystalline Tetragonal Zirconia. *Journal of the American Ceramic Society*, 502(1992):493–502, 1992. ISSN 00027820.
- [60] J. Patel and M. Cohen. Criterion for the action of applied stress in the martensitic transformation. *Acta Metallurgica*, 1(5):531–538, sep 1953. ISSN 00016160.
- [61] X. Y. Zhang, L. Brinson, and Q. P. Sun. The variant selection criteria in single-crystal CuAlNi shape memory alloys. *Smart Materials and Structures*, 9(5):571–581, 2000. ISSN 0964-1726.
- [62] Y. Zou and R. Spolenak. Size-dependent plasticity in micron- and submicron-sized ionic crystals. *Philosophical Magazine Letters*, 93(7):431–438, 2013. ISSN 0950-0839.
- [63] A. Montagne, S. Pathak, X. Maeder, and J. Michler. Plasticity and fracture of sapphire at room temperature: Load-controlled microcompression of four different orientations. *Ceramics International*, 40(1 PART B):2083–2090, 2014. ISSN 02728842.
- [64] S. Kiani, K. W. K. Leung, V. Radmilovic, A. M. Minor, J. M. Yang, D. H. Warner, and S. Kodambaka. Dislocation glide-controlled room-temperature plasticity in 6H-SiC single crystals. *Acta Materialia*, 80:400–406, 2014. ISSN 13596454.
- [65] U. Messerschmidt, D. Baither, B. Baufeld, and M. Bartsch. Plastic deformation of zirconia single crystals: a review. *Materials Science and Engineering: A*, 233(1-2):61–74, 1997. ISSN 09215093.
- [66] X. M. Zeng, Z. Du, C. A. Schuh, N. Tamura, and C. L. Gan. Microstructure, crystallization and shape memory behavior of titania and yttria co-doped zirconia. *Journal of the European Ceramic Society*, 36(5):1277–1283, 2016. ISSN 09552219.
- [67] A. Suresh, M. Mayo, and W. Porter. Thermodynamics of the tetragonal-to-monoclinic phase transformation in fine and nanocrystalline yttria-stabilized zirconia powders. *Journal of Materials Research*, 18(12):2912–2921, dec 2003. ISSN 0884-2914.

- [68] S. M. Ueland and C. A. Schuh. Superelasticity and fatigue in oligocrystalline shape memory alloy microwires. *Acta Materialia*, 60:282–292, 2012.
- [69] S. M. Ueland and C. A. Schuh. Grain boundary and triple junction constraints during martensitic transformation in shape memory alloys. *Journal of Applied Physics*, 114(5):053503, 2013. ISSN 00218979.
- [70] N. Tuncer, L. Qiao, R. Radovitzky, and C. A. Schuh. Thermally induced martensitic transformations in Cu-based shape memory alloy microwires. *Journal of Materials Science*, 50(22):7473–7487, 2015. ISSN 0022-2461.
- [71] I. Donald. Review Production, properties and applications of microwire and related products. *Journal of Materials Science*, 22:2661–2679, 1987.
- [72] K. Y. Yon, B. S. Mitchell, and S. A. Dunn. Introduction of new reinforcement for cementitious materials—Calcium/alumina (CA) fibers formed by the inviscid melt-spinning (IMS) process. *Cement and Concrete*, 15(3):165–172, jan 1993. ISSN 09589465.
- [73] Z. Xiao and B. Mitchell. The production of mullite fibers via inviscid melt-spinning (IMS). *Materials Letters*, 37(6):359–365, 1998.
- [74] R. Cunningham, L. Rakestraw, and S. Dunn. Inviscid Spinning of Filaments via Chemical Jet Stabilization. *Spinning Wire From Molten Metal*, 74(180):20–31, 1978.
- [75] J. Doshi and D. Reneker. Electrospinning process and applications of electrospun fibers. *Conference Record of the 1993 IEEE Industry Applications Conference Twenty-Eighth IAS Annual Meeting*, 35:151–160, 1993. ISSN 03043886.
- [76] D. Li and Y. Xia. Electrospinning of nanofibers: Reinventing the wheel? *Advanced Materials*, 16(14):1151–1170, 2004. ISSN 09359648.
- [77] D. Li, Y. Wang, and Y. Xia. Electrospinning of polymeric and ceramic nanofibers as uniaxially aligned arrays. *Nano Letters*, 3(8):1167–1171, 2003. ISSN 15306984.
- [78] D. Li, J. T. McCann, Y. Xia, and M. Marquez. Electrospinning: A simple and versatile technique for producing ceramic nanofibers and nanotubes. *Journal of the American Ceramic Society*, 89(6):1861–1869, 2006. ISSN 00027820.
- [79] L. Gibson and M. F. Ashby. *Cellular Solids*. Cambridge University Press, Cambridge, UK, 2nd edition, 1997.
- [80] S. Berro, R. El Ahdab, H. Hajj Hassan, H. M. Khachfe, and M. Hajj-Hassan. From plastic to silicone: the novelties in porous polymer fabrications. *Journal of Nanomaterials*, 2015:1–21, 2015.
- [81] G. Davies and S. Zhen. Review Metallic foams: their production, properties and applications. *Journal of Materials Science*, 18:1899–1911, 1983. ISSN 0022-2461.
- [82] J. Banhart. Metal foams: Production and stability. *Advanced Engineering Materials*, 8(9):781–794, 2006. ISSN 14381656.
- [83] J. Banhart. Manufacture, characterisation and application of cellular metals and metal foams. *Progress in Materials Science*, 46(6):559–632, 2001. ISSN 00796425.
- [84] P. Sepulveda and J. Binner. Processing of cellular ceramics by foaming and in situ polymerisation of organic monomers. *Journal of the European Ceramic Society*, 19(12):2059–2066, 1999. ISSN 09552219.

## BIBLIOGRAPHY

- [85] Y. Gu, X. Liu, G. Meng, and D. Peng. Porous YSZ ceramics by water-based gelcasting. *Ceramics International*, 25(8):705–709, 1999. ISSN 02728842.
- [86] M. A. Alves-rosa, L. Martins, S. H. Pulcinelli, and C. V. Santilli. Design of microstructure of zirconia foams from the emulsion template properties. *Soft Matter*, 9:550–558, 2013.
- [87] A. Kishimoto, T. Higashiwada, H. Asaoka, and H. Hayashi. The exploitation of superplasticity in the successful foaming of ceramics after sintering. *Advanced Engineering Materials*, 8(8):708–711, 2006. ISSN 14381656.
- [88] X. Miao. Modification of Porous Alumina Ceramics with Bioinert and Bioactive Glass Coatings. *Advanced Materials Research*, 32:211–214, 2008.
- [89] H. Sieber, C. Hoffmann, a. Kaindl, and P. Greil. Biomorphic cellular ceramics. *Advanced Engineering Materials*, 2(3):105–109, 2000. ISSN 14381656.
- [90] A. Herzog, R. Klingner, U. Vogt, and T. Graule. Wood-Derived Porous SiC Ceramics by Sol Infiltration and Carbothermal Reduction. *Journal of the American Ceramic Society*, 87(5):784–793, 2004. ISSN 00027820.
- [91] L. R. Meza, S. Das, and J. R. Greer. Strong, lightweight, and recoverable three-dimensional ceramic nanolattices. *Science*, 345(6202):1322–1326, sep 2014. ISSN 0036-8075.
- [92] S. Deville. Freeze-Casting of Porous Ceramics: A Review of Current Achievements and Issues. *Advanced Engineering Materials*, 10(3):155–169, mar 2008. ISSN 14381656.
- [93] T. Fukasawa, M. Ando, T. Ohji, and S. Kanzaki. Synthesis of Porous Ceramics with Complex Pore Structure by Freeze-Dry Processing. *Journal of the American Ceramic Society*, 84(1):230–232, 2001. ISSN 00027820.
- [94] C. Hong, X. Zhang, J. Han, J. Du, and W. Han. Ultra-high-porosity zirconia ceramics fabricated by novel room-temperature freeze-casting. *Scripta Materialia*, 60(7):563–566, 2009. ISSN 13596462.
- [95] S. W. Sofie. Fabrication of functionally graded and aligned porosity in thin ceramic substrates with the novel freeze-tape-casting process. *Journal of the American Ceramic Society*, 90(7):2024–2031, 2007. ISSN 00027820.
- [96] E. Alfonso, J. Olaya, and G. Cubillos. Thin film growth through sputtering technique and its applications. *Crystallization - Science and Technology*, pages 397–432, 2012.
- [97] M. Ohring. *Materials Science of Thin Films*. Academic Press, 2nd edition, 2002.
- [98] A. Ishida, A. Takei, and S. Miyazaki. Shape memory thin film of TiNi formed by sputtering. *Thin Solid Films*, 228(1-2):210–214, 1993. ISSN 00406090.
- [99] S. Miyazaki and A. Ishida. Martensitic transformation and shape memory behavior in sputter-deposited TiNi-base thin films. *Materials Science and Engineering A-Structural Materials Properties Microstructure and Processing*, 273:106–133, 1999. ISSN 09215093.
- [100] W. L. Benard, H. Kahn, A. H. Heuer, and M. A. Huff. Thin-film shape-memory alloy actuated micropumps. *Journal of Microelectromechanical Systems*, 7(2):245–251, 1998. ISSN 10577157.
- [101] Y. Fu, W. Huang, H. Du, X. Huang, J. Tan, and X. Gao. Characterization of TiNi shape-memory alloy thin films for MEMS applications. *Surface and Coatings Technology*, 145(1-3):107–112, aug 2001. ISSN 02578972.
- [102] H. Huang, M. Nakamura, P. Su, R. Fasching, Y. Saito, and F. B. Prinz. High-Performance Ultrathin Solid Oxide Fuel Cells for Low-Temperature Operation. *Journal of The Electrochemical*

- Society*, 154(1):B20, 2007. ISSN 00134651.
- [103] F. Smeacetto, M. Salvo, L. C. Ajitdoss, S. Perero, T. Moskalewicz, S. Boldrini, L. Doubova, and M. Ferraris. Yttria-stabilized zirconia thin film electrolyte produced by RF sputtering for solid oxide fuel cell applications. *Materials Letters*, 64(22):2450–2453, 2010. ISSN 0167577X.
- [104] S. de Souza. Thin-film solid oxide fuel cell with high performance at low-temperature. *Solid State Ionics*, 98(1-2):57–61, 1997. ISSN 01672738.
- [105] Y. Ma, Y. Ono, L. Stecker, D. R. Evans, and S. T. Hsu. Zirconium Oxide Based Gate Dielectrics with Equivalent Oxide Thickness of Less Than 1.0 nm and Performance of Submicron MOS-FET using a Nitride Gate Replacement Process. In *Electronic Devices Meeting*, pages 149–152, 1999. ISBN 0780354109.
- [106] Y. Miyahara. Characterization of sputtered yttria stabilized zirconia thin film and its application to a metal insulator semiconductor structure. *Journal of Applied Physics*, (May 2013), 1992.
- [107] A. Javey, H. Kim, M. Brink, Q. Wang, A. Ural, J. Guo, P. McIntyre, P. McEuen, M. Lundstrom, and H. Dai. High-kappa dielectrics for advanced carbon-nanotube transistors and logic gates. *Nature materials*, 1(4):241–246, 2002. ISSN 14761122.
- [108] M. Boulouz, A. Boulouz, A. Giani, and A. Boyer. Influence of substrate temperature and target composition on the properties of yttria-stabilized zirconia thin films grown by r.f. reactive magnetron sputtering. *Thin Solid Films*, 323(1-2):85–92, jun 1998. ISSN 00406090.
- [109] F. Konushi, T. Doi, H. Matsunaga, Y. Kakihara, M. Koba, K. Awane, and I. Nakamura. Epitaxial growth of zirconia and yttria stabilized zirconia films on sapphire substrates by reactive sputtering. *Mat. Res. Soc. Symp. Proc.*, 56:259, 1986.
- [110] S. Ben Amor, B. Rogier, G. Baud, M. Jacquet, and M. Nardin. Characterization of zirconia films deposited by r.f. magnetron sputtering. *Materials Science and Engineering: B*, 57(1):28–39, dec 1998. ISSN 09215107.
- [111] B. Liaw. Thin-film yttria-stabilized tetragonal zirconia. *Solid State Ionics*, 92(1-2):85–89, 1996. ISSN 01672738.
- [112] P. Dutta. Grazing incidence X-ray diffraction. *Current Science*, 78(12):1478–1483, 2000. ISSN 15206106.

